2014

Strain decomposition for the soft elastomeric capacitors (SECs) network and investigation of sensor placement's effect on estimating accuracy

Chunhui Song
Iowa State University

Strain decomposition for the soft elastomeric capacitors (SECs) network and investigation of sensor placement's effect on estimating accuracy

by

Chunhui Song

A thesis submitted to the graduate faculty

in partial fulfillment of the requirements for the degree of

MASTER OF SCIENCE

Major: Civil Engineering (Structural Engineering)

Program of Study Committee:
Simon Laflamme, Major Professor
Jiehua J. Shen
Halil Ceylan

Iowa State University

Ames, Iowa

2014

TABLE OF CONTENTS

LIST OF FIGURES

LIST OF TABLES

ACKNOWLEDGEMENTS

I would like to express my great appreciation to Dr Simon Laflamme. You have been a tremendous mentor, adviser and lighthouse for my academic life. I would like to thank you for providing this research opportunity and allowing me to grow as a research assistant. Your valuable and constructive suggestions and assistance helped me go through the difficulties during the research. My grateful thanks are also extended to Dr Fouad S. Fanous, for his assistance with ANSYS computer software in solving finite element analysis for our experimental specimen model. I also appreciate the willingness of Dr Jiehua J. Shen and Dr Halil Ceylan to be my committee members. I wish to acknowledge the help provided by Douglas Wood and Owen Steffens. Thanks for permission to use the laboratory utilities and facilities and for assistance for experimental equipment installation and computer software guidance.

I wish to give my special thanks to my family member Huiping Dong, Weiming Song and Lin Gao for their financial support, encouragement, patience and motivation. My completion of this research work could not be accomplished without the support of my colleagues Hussam Saleem, Jinzhe Wu, Zhengyu Liu and Daniel Safier. Thanks to Hussam Saleem for sensor fabrication and guidance with experiments and problems troubleshooting experimental equipment. Thanks to Jinzhe Wu for the hard work on the same project, the help provided to each other and encouragement. I really appreciate the technical help from Zhengyu Liu. Thank Daniel Safier for his advice and the creative method he proposed. Also, I would like to thank all my friends and classmates; I could not finish my study without your support and companionship.

At last, I would like to thank Iowa State University with this great academic experience in my life.

ABSTRACT

An innovative sensor network consists of soft elastomeric capacitors (SECs) has been proposed for large scale civil infrastructures such as wind turbines. Each SEC unit is able to convert a change in local strain into a change in capacitance due to geometric deformation of the patch. Since each SEC unit measures unidirectional strain under the covered surface, a method is needed to be developed in order to decompose strain into principle components.

To perform the strain decomposition task, a strain surface fitting algorithm using polynomial interpolation functions has been developed. Firstly, the proposed algorithm was validated on both symmetrical and nonsymmetrical plates under various loading conditions. The strain polynomial functions used for plates were assumed based on the classic plate theory. By minimizing the errors between real and estimated strain values, a coefficient matrix was estimated and used to estimate bi-dimensional strains. The results of predicted strains showed good agreement with real strain data extracted from the finite element models. Once the algorithm was validated, multiple ways of sensor arrangements were performed in order to investigate the effects of sensor placement on estimating accuracy. It is found that the estimating accuracy can be improved if either the inner sensors were staggered or the amount of boundary sensors was reduced.

CHAPTER 1 INTRODUCTION

1.1 Motivation

Wind energy has become a big investment not only in the United States but all around the world. As one of the fastest growing renewable energy sources, the worldwide wind capacity reached 254,000 MW by the end of June 2012, out of which 16,546 MW were added in the first six months of 2012. According to World Wind Energy Association [1], the overall growth rate of wind energy in 2011 reached 20.3%. With wind being a strong resource of energy, it needs to be as efficient and reliable as possible, especially with the increase in use. Chia Chen et al. (2008) talked about many hardships to take into account when operating turbines efficiently and effectively including: the difficulty of inspections and maintenance, the susceptibility to accidents with maintenance workers and/or the public, the location of turbines in remote areas with limited access for repair, the large size of structures, the out-of-service time, and the frequency of unexpected failure [2]. A vital area of concern is regular maintenance and repair, especially of the turbine blades. Electrical components tend to have the highest failure rates. Drivetrains and blades, however, tend to create the longest out-of-service time and cost the most to repair. Turbine blades generally account for 15-20% of the total cost of the turbine and are a key component to the generation of energy [2]. Today the size of wind turbine blade is increasing in order to achieve a better energy harvesting effectiveness. At the same time, it dramatically increases the difficulties of routine maintenances that are required periodically. The failure of blades can also lead to

secondary failures of other components as well as potentially leading to failure of the whole tower.

In order to make turbines safer and more efficient, they must be monitored on a regular basis to track the operational and structural health at any given time. Considered from both safe and economical aspects, a monitoring technique needs to be employed to minimize downtime as well as to decrease unexpected breakdowns. Structural health monitoring (SHM) is a technique that implements damage detection and condition assessment for engineering structures. The SHM process consists of the observation of a structure over time by periodically recorded measurements, the extraction of damage related features from the measurements, and the determination of current conditions of the structures using statistical analysis of extracted features [3]. For most of existing SHM solutions, the most fundamental challenge is that damage is usually a local phenomenon and might have minor effects on lower-frequency global response of structures, which is measured by the entire system. The majority of the current literature over last 30 years, however, have focused more on identifying damage on global basis [3]. In the meantime, the features selection and damage data collection for complicated structures are difficult due to unknown behaviors and a limited number of sensor locations. In fact, it is hard to employ a technique like fiber-optic over a large scale structure due to economic issues. Thus, there is a demand to develop a sensing solution designed especially for large scale civil infrastructures. It should be cost-effective and should have capabilities to extract damage features on a local basis. At this point, a sensing network comprising soft elastomeric capacities (SECs) has been introduced.

1.2 Problem Statement

Because current application of sensing solutions to large scale structural health monitoring are limited by economic and/or technical challenges, a group of bio-inspired sensing skin has been developed for a cost-effective sensor network specifically designed for strain sensing wind turbine blades. The network consists of soft elastomeric capacitors (SECs) deployed in array form. Each SEC is fabricated from a nanocomposite mix of SEBs, which is used to fabricate dielectric and electrodes. The sensing principle is that when the monitored surface deforms, each SEC unit is able to catch the change in capacitance by the change in geometry. Capacitance signals then can be transformed into strain signals. Capacitance data will be collected using an off-the-shelf data acquisition system (ACAM PCap01). Transformation from capacitances to strain data is performed using MATLAB. The capacitance C of a SEC is written as [4]:

$$C = e_r e_0 \frac{A}{h} \qquad (Eq. 1)$$

Where, C, is the nominal capacitance of an SEC, e_0 = 8.854 pF/m is the vacuum permittivity, e_r is the dimensionless polymer relative permittivity, and $A = wl$ is the area of an SEC with width w and length l. Since SEC is attached to monitoring surface using epoxy, we could assume that only length and thickness are changed with no change in width. In addition, it is assumable that elastomer is incompressible so that the volume of SEC remains the same after geometry deforms. Through these relations, capacitance signals are transformed to strain signals, and unidirectional strain is able to be obtained. Since it is very common that biaxial stress states happen in structural components, normal stresses and

strains are necessarily obtained in order to perform stress analysis that is a primary of comparison with criterion of failure. Therefore, a method that can decompose the unidirectional strain needs to be developed and evaluated. Also, the influence of sensor arrangement for estimating accuracy is to be investigated.

1.3 Research Objectives and Scopes

The objectives of this research are to develop a technique that is able to decompose the strain signals measured by SEC networks and to investigate the effect of the sensor placement on estimating accuracy. A strain fitting algorithm was proposed and adopted to perform the task. Classical thin plate theory has been applied to assume polynomial functions for strain. The effectiveness of the proposed algorithm was evaluated on a geometrically skewed plate that was designed based on a CX-100 wind turbine blade. The influences of material properties, arbitrary loading, and geometry variation were discussed in terms of estimating accuracy as well. Another purpose of the study is to investigate the effects of sensor placement for estimating accuracy of the proposed algorithm.

1.4 Thesis Organization

The thesis is organized as follows: CHAPTER 2 provides background information on various topics including: SHM applications for wind turbine blades, existing sensor types, and backgrounds of SECs networks. CHAPTER 3 introduces the principles of the proposed algorithm as well as the application of the algorithm on a FEA based rectangular plate. The

decomposing accuracy of the algorithm was evaluated and discussed for the different loading cases. CHAPTER 4 illustrates the effect of different sensor placements on estimating accuracy. The results were compared with uniform sensor arrangement and two sensor arrangements have shown positive effects on estimating accuracy. CHAPTER 5 presents the application of the algorithm on a blade-shaped plate as well as the verification of improvement by applying the two positive sensor arrangement. CHAPTER 6 concludes the study and provides several recommendations regarding the applications. Finally, future research work is suggested.

CHAPTER 2 BACKGROUND INFORMATION

2.1 SHM Application for Wind Turbine Blades

Structural health monitoring (SHM) is a reliable technique that implements damage detection and condition assessment especially for engineering structures. According to Charkes R. et al. (2007), the SHM process consists of the observation of a structure over time by periodically recorded measurements, the extraction of damage related features from the measurements, and the determination of current conditions of the structures using statistical analysis of extracted features. One of the most popular application fields of SHM is for wind turbine systems because wind energy is becoming more and more important among other renewable energies because of its mature technology, good infrastructures, and cost-competitiveness. As wind turbines increase in blade size, which lead to more effective wind energy harvesting, and the cost of initial investment for wind turbine system correspondingly increases. This increase results in more demand for monitoring the operational condition of the wind turbine blades. In this section, monitoring methods using different types of sensors are reviewed.

2.1.1 Optical fiber sensors

The optical fiber can be made of either plastic or glass and is widely used for fiber-optic communication that allows signals transmit over much longer distance but with much less loss than other types of wired or wireless communication. Optical fiber sensors are fiber-based

techniques for sensing typically mechanical strain, load or temperature. It can be attached to the surface of structural components like wind turbine blades to measure strain and load. According to [5], the general principle of these types of sensors is that they use light instead of electricity from a laser or other sources to transfer information through an optical fiber. The signal will experience tiny change to its parameters either from its fiber or several fiber Bragg gratings, and the changes are transferred and captured by a detector arrangement. The light source will lose optical power when it is traveling through a plastic optical fiber. The level of reduction depends on the surface strain of the optical fiber. By utilizing this feature, a type of strain sensor can be developed. For example, if a piece of optical fiber is attached on the surface of a structure and is receiving a light source generated by an emitting diode, the light is focused through lens and incident to a photo detector and the power of the light is measured by an optical power meter; one can capture the change of power due to the optical fiber's change in strain, which can be used to detect damage in a structure [6]. Figure 1 illustrates the propagation process of rays in a deformed optical fiber, and the reduction of power is due to leaked rays. Figure 2 illustrates the relationship between optical power and strain. Normalized optical power decreases linearly against strain up to 10000 με and then starts to drop faster nonlinearly.

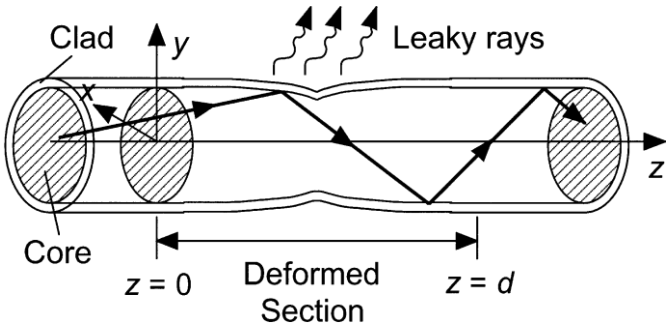

Figure 1: Propagation of rays in deformed optical fiber [6].

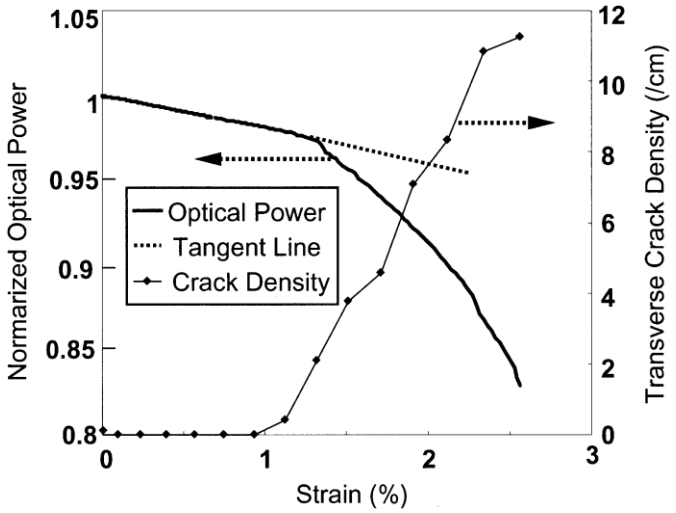

Figure 2: Optical power and strain relation [6].

In particular, one of the most common optical fiber types is optical fiber Bragg grating sensor (FBG). FBGs are small optical fiber pieces (10mm in length) that are spatially arranged with various refractive index in the core (Figure 3). It works like a light reflector, and the reflection ratio can be maximized at a specific wavelength. The shift of peak then can be related to applied external load, induced strain or varied temperature [5]. Usually, at a wavelength of 1550nm, FBG sensors have a temperature sensitivity around 10pm/ ℃ and strain sensitivity around 1.2pm/$\mu\varepsilon$ [5]. For pure strain sensing, the accuracy is sufficient in that its resolution can be the range of a few $\mu\varepsilon$.

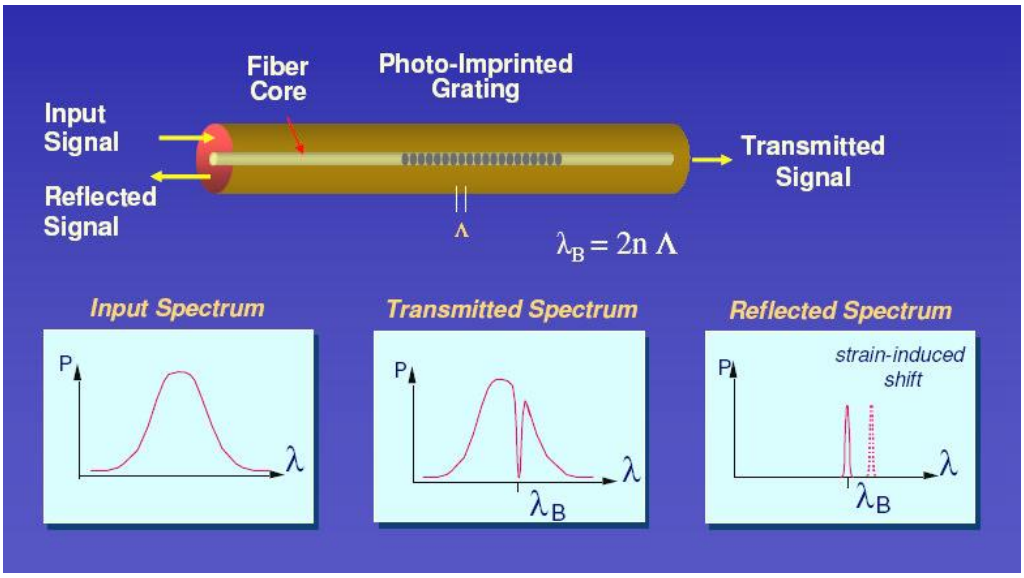

Figure 3: Transmission and reflection spectra of a FBG [5].

For application of turbine blades, FBGs offer several advantages over the conventional sensors: (1) FBGs have immunity to electromagnetic and lightning interferences [5]; (2) FBGs are resistant to corrosion and integration into composite material of the blades with minimal degradation to the host materials [5]; (3) because measured information is encoded in the wavelength of reflected light, FBGs are immune to drifts and no down-lead sensitivity is included [7]; and (4) a combination of several gratings into a single fiber is possible so that FBG systems have the capacities of outputting a large amount of sensors simultaneously through few fibers, which reduces the requirements of cables and initial installations [7]. The cost for a group of this type of sensors, however, is still too expensive for SHM application on a large scale wind turbine blades. In addition, FBGs are sensitive to temperature changes, which may have negative influence on sensing accuracy [8].

2.1.2 Acoustic emission monitoring

According to Wikipedia [9], acoustic emission (AE) is a phenomenon in which transient elastic waves are generated by materials when energy in a material or on its surface is released suddenly. This process could be a result of external forces, deformation, cracking, debonding, delamination or others that occur to materials. AE is widely used for study in inspection, system feedback, and process monitoring. For SHM on turbine blades, piezoelectric sensors are commonly applied to detect stress waves within a structure. According to the research of P.A. Joosse et al. (2002), certification tests on small wind turbine blades were conducted using AE monitoring technique. The sensing system was identified as a considerable method towards understanding the damage mechanisms of the blades because of its sensitivity and ability to detect much weaker signals than those normally audible to test engineers [10]. The practical benefits of AE monitoring by piezoelectric sensors were concluded in a research project by Erik R. et al. (2004). According to these researchers, the benefits of piezoelectric sensors include their capability to detect the high frequency component of stress released waves produced by materials undergoing energy loss. Also, clustered AE events, which were emitted at a low load level, were recognized around certain points coinciding with eventual failure locations, which was shown useful for predicting the potential failure points of a structure [11]. It was also observed that multiple piezoceramic sensors are able to connected together to each other in a array pattern, and thus the amount of data acquisition channels can be reduced, and cost-effectiveness is improved [12]. In reference [13], the application of an acoustic emission test on a stationary in-service turbine blade is presented. The real-time monitoring of the blade is proved to be feasible using a radio telemetry system to transfer AE signals from operating blades to the ground without loss in resolution. The results showed that AE signals captured from the rotating

blade have an acceptable level of noise under low or moderate wind speed. Problems related to temporary loss of signals and sensor attachments, however, still need to be resolved. Also, in order to evaluate the effectiveness of such a system for application on large scale structures, an economic solution needs to be carried out.

2.1.3 Electrical resistance-based damage detection

Electrical resistance-based damage detection is a method capable of detecting local damage on a structure. In reference [14], the authors utilized high electric conductivity characteristic of carbon fiber reinforced polymer (CFRP), and they developed an electrical impedance change method for identifying a delamination location and size of beam-type specimens. As illustrated in figure 4, several electrodes were attached by copper foil on the surface of the specimens in order to detect the change of electric resistance. It is noticeable that all the electrodes were mounted on one side of the specimen, which could be a representation of modeling sensors placement on a turbine blade. The change in electric resistance between each electrode under different delamination cases was measured, and then it was used to analyze relations between electric resistance change and delamination events. It was the prediction of delamination location and size that comprises one of the inverse problems where response surface methodology is applied. A set of tests were conducted, and the results show that electrical impedance change method was able to detect delamination in composites. Moreover, a certain amount of electrodes was required to obtain an acceptable performance.

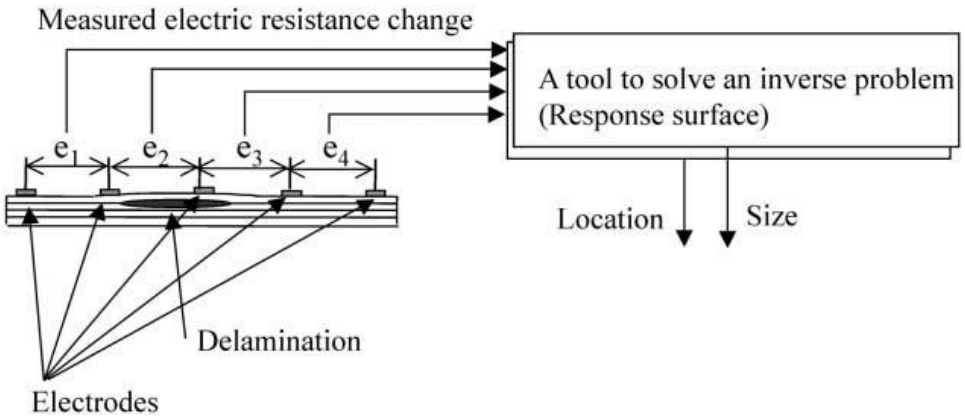

Figure 4: Schematic representation of electrical impedance change method for identification of delamination [14].

Ryosuke M et al. [15] proposed a wireless system consists of CFRP composite laminates and a ceramic oscillating circuit for in-service wind turbine blades monitoring. The basic sensing principle is that a delamination crack of composite induces change in electric resistance and oscillating frequency of the circuit so that signal receiver can capture the variation. Theoretically, the electric resistance along fiber orientation is negligible, and as in transverse orientation, it is infinite if carbon fiber alignments are perfectly straight. In practice, electrical resistance in transverse direction is still much larger than one in the fiber orientation, even though carbon fibers are not perfectly oriented. The fiber-contact-network between plies could be hindered if delamination crack occurs, as illustrated in Figure 5. This occurrence results in increased electrical resistance in the carbon laminated composites as measured by oscillating circuits. The ceramic oscillator is the key role in transmitting signals of electrical resistance change into a change of oscillating frequency to the receiver. The entire process is illustrated in Figure 6 as follows.

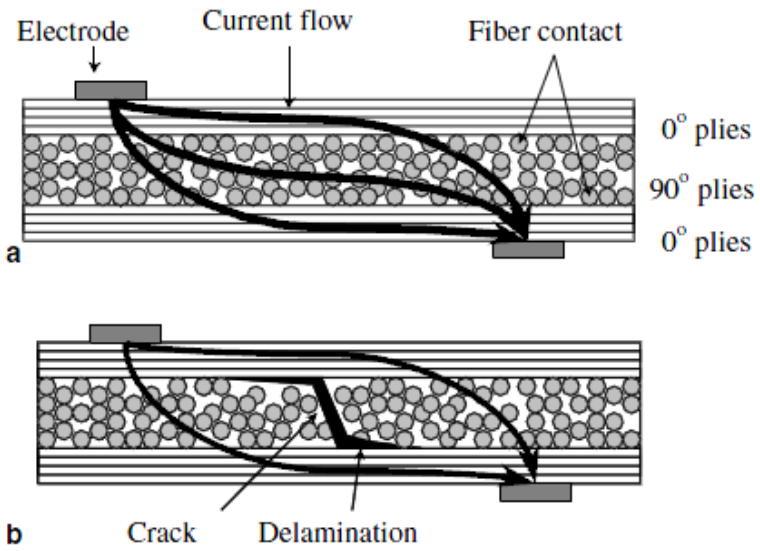

Figure 5: Schematic Presentation of a carbon composite when electrical current is applied. (a) Electrical network of the fiber in a CERP laminate. (b) Electrical network is broken with a delamination [15].

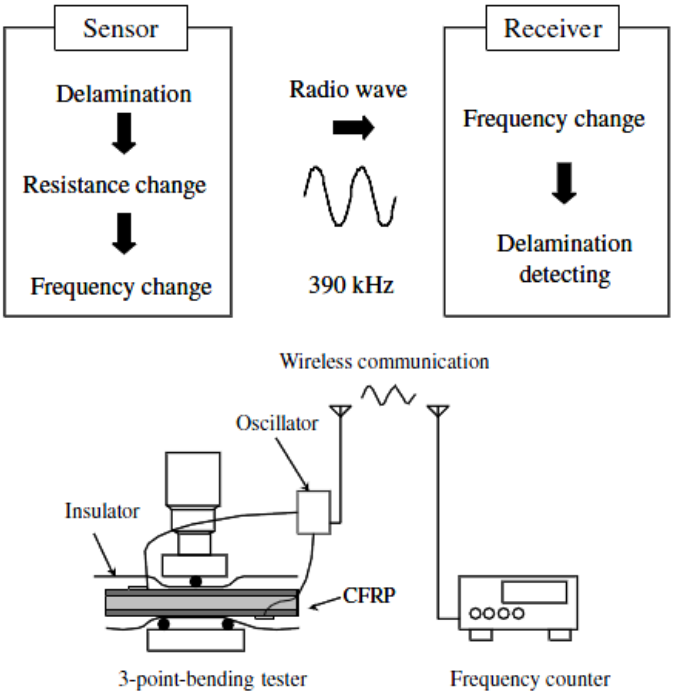

Figure 6: Electrical resistance-based wireless delamination detecting system [15].

2.2 Soft Elastomeric Capacitors (SECs)

2.2.1 Introduction

As literature review in previous section implies, when implementing a long-term SHM system for geometrically large scale civil structures, the task is becoming more complicated in terms of the cost-effectiveness of existing automotive monitoring solutions. The concepts of oft elastomeric sensors have been proposed previously in multiple literature in which a patch antenna is designed and functions as a transducer that encodes surface strain into its resonant frequency [16]. Also a self-healing sensor skin that is fabricated using copper-clad polyimide sheets has been presented for damage detection using this skin [17]. In reference [18], a composite electrical resistance strain sensor based on single wall nanotubes (SWNTs) was formed and experimentally tested, and results showed that it is able to detect a small crack through its under dynamic loading.

In order to achieve the objective of this study, an innovative sensor network comprised of multiple soft elastomeric capacities (SECs) has been designed and presented for large-scale application, more specifically, for wind turbine blades. The objective is to provide a cost-effective solution for SHM application. Additionally, a group of SECs are deployed and distributed in array form and used as surface strain gauges. The fabrication will be presented, and discussion about sensing principle and sensor performance follow that presentation.

2.2.2 Sensor fabrication

The SEC proposed by authors [4] consists of three layers: a nanocomposite mix elastomer serving as dielectric for the capacitor, which is sandwiched between two high-conductive electrodes. A thermoplastic elastomer (SEBS Dryflex 500120, $\rho = 930$ kg/m^3) is used to form nanocomposite mix. It is doped with titanium dioxide (TiO_2 - Sachtleben R 320 D) in order to enhance permittivity and robustness in the material with respect to mechanical tempering. The electrodes are composed from same SEBS mix but with a certain concentration of carbon black (CB) particles. Figure 7 shows the completed process of SEC fabrication. It is started with a dissolution of SEBS using toluene solution. Part of the solution is used to produce dielectric with a mixing of TiO_2 whereas sonication is performed to disperse the particles. SEBS-TiO_2 solution is then drop-casted on a glass surface, which is coated with Teflon sheet. At the same time, CB particles are added to the rest of the SEBS/toluene solution to increase conductivity of the mix, and it is dispersed using ultrasonic tip. Once SEBS-TiO_2 solution is dried completely, the CB solution will be painted on both sides of the polymer. At last, two copper strip cables are attached on two corners of the patch. A completed sample of SEC is shown in Figure 8. Each SEC has dimension of 7 cm by 7 cm.

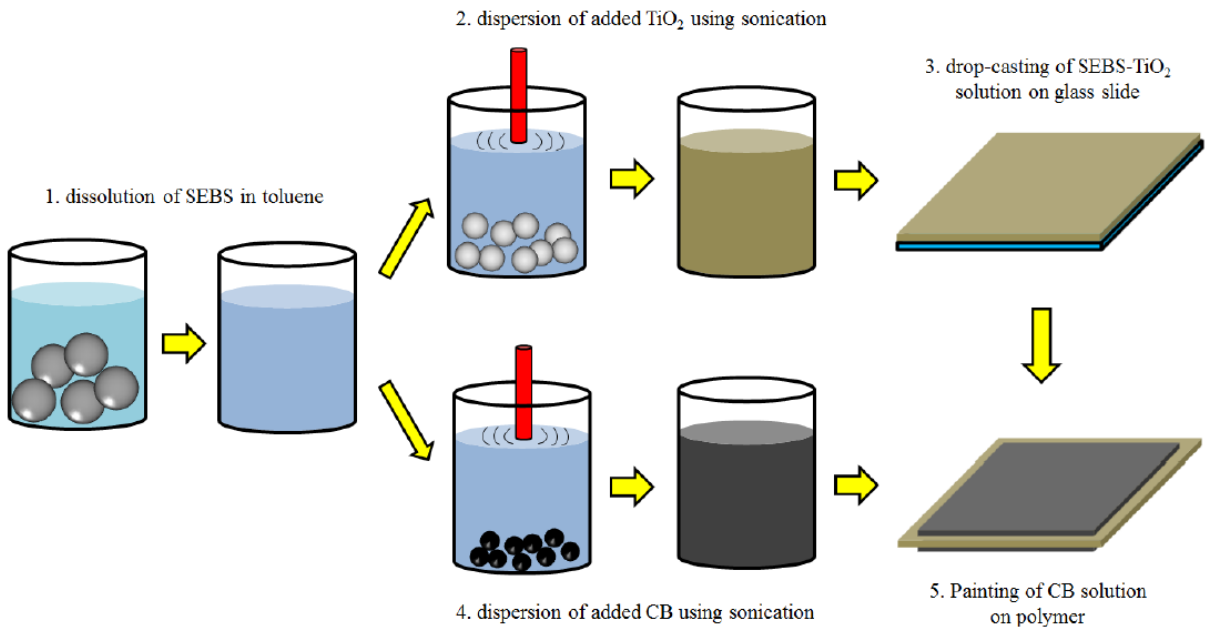

Figure 7: Fabrication process of SEC using drop casting method [4].

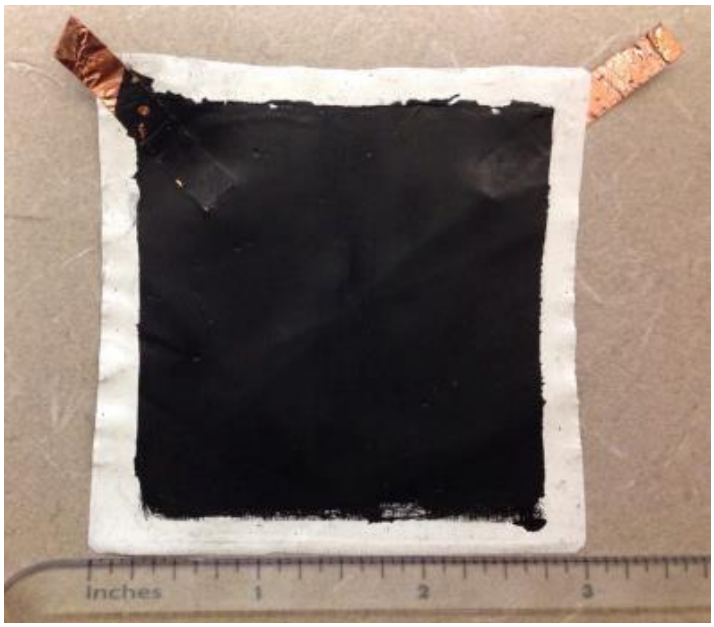

Figure 8: SEC sample.

2.2.3 Sensing principles

As mentioned in CHAPTER 1, the capacitance of a SEC can be expressed as:

$$C = e_r e_0 \frac{A}{h} \qquad (Eq. 1)$$

Where C is the nominal capacitance of an SEC, e_0 = 8.854 pF/m is the vacuum permittivity, e_r is the dimensionless polymer relative permittivity, and $A = w \times l$ is the area of an SEC with width w and length l, and h is the height. As illustrated in Figure 9, the height h consists of the height of dielectric h_d, and the height of the conductive plates h_p, ($h = h_d + 2h_p$).

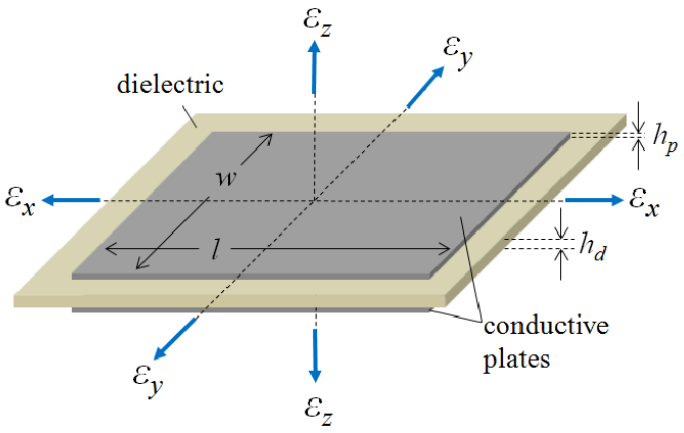

Figure 9: Schematic of deformations for SEC unit [19].

An SEC is then adhered on the sensing surface in the xy-plane using epoxy when applying it, and the geometry change in x and y directions will lead to strain in both directions, ε_x and ε_y. In the meantime, strain ε_z will be induced only depending on the effect of Poisson's ratio of SEBs ($\nu \approx 0.49$ [20]). Since SEC is mechanically modeled to be an incompressible solid, the volume remains the same ($\Delta V = 0$) after SEC deforms Δl, Δw and Δh:

$$wlh = (w + \Delta w)(l + \Delta l)(h + \Delta h) \qquad (Eq. 2)$$

Expending the expression shown above, vanishing higher order terms and combining like terms:

$$\Delta wlh + w\Delta lh + wl\Delta h \approx 0 \qquad (Eq.3)$$

Dividing Eq. (3) by w, l, h successively, the expression reads:

$$-\frac{\Delta h}{h} = \frac{\Delta h}{h} + \frac{\Delta h}{h} \ or - \varepsilon_z = \varepsilon_x \varepsilon_y \qquad (Eq.4)$$

A small change of capacitance C can be expressed from Eq. (1) using differential ΔC:

$$\frac{\Delta C}{C} = \left[\frac{(w+\Delta w)(l+\Delta l)}{(h+\Delta h)} - \frac{wl}{h}\right]\frac{h}{wl} \qquad (Eq.5)$$

Simplify Eq. (5) and divide by w, l, h successively for both numerator and denominator; also, eliminate term $\frac{\Delta h}{h}$ in denominator since it is relatively small compare to 1:

$$\frac{\Delta C}{C} = \frac{\Delta l}{l} + \frac{\Delta w}{w} + \frac{\Delta w \Delta l}{wl} - \frac{\Delta h}{h} \qquad (Eq.6)$$

If vanishes term $\frac{\Delta w \Delta l}{wl}$, substitute the expression of - $\frac{\Delta h}{h}$ from Eq. (4) into Eq. (6), then a new relationship occurs between change in capacitance and strain ε_x and $\varepsilon_y$with a gauge factor of 2:

$$\frac{\Delta C}{C} = 2\left(\varepsilon_x + \varepsilon_y\right) or \ \frac{\Delta C}{C} = 2\varepsilon_s \qquad (Eq.7)$$

Because ε_s represents SEC readings since it only measures unidirectional strain, the expression reads Eq. (7) as:

$$\frac{\Delta C}{\varepsilon_s} = 2C \ \ or \ \ \frac{\Delta C}{\Delta l} = \frac{e_0 e_r w}{h} \qquad (Eq.8)$$

Up until now, one can relate change in capacitance to strain with a gauge factor of 2 according to Eq. (7). The transformations shown in Eq. (8) represent the sensitivity of the sensor. It is possible to enhance the sensitivity in the following ways: (1) decrease the thickness of the

sensor; (2) increase the width of the sensor; (3) improve the dielectric permittivity. Also, ±20% of variance of sensitivity is expected because of manual fabrication discrepancy [4].

2.2.4 Data acquisition system (DAQ)

The data acquisition system (DAQ) used for data collection is Acam PCap01-EVA-KIT. It consists of a main board, a plug-in module, a Windows-based evaluation software, and the PICOPROG programming device. The PICOPROG device is used to connect the DAQ system to the PC through a USB interface. The computer software offers user-friendly options and configurations for a single PCap01 chip for capacitance measurement. For SECs, one side of electrical wires are soldered and connected to two copper cables on SECs, with the other side connected to a bread board with multiple channels. The devices and the channels connections for SECs are presented in Figure 10:

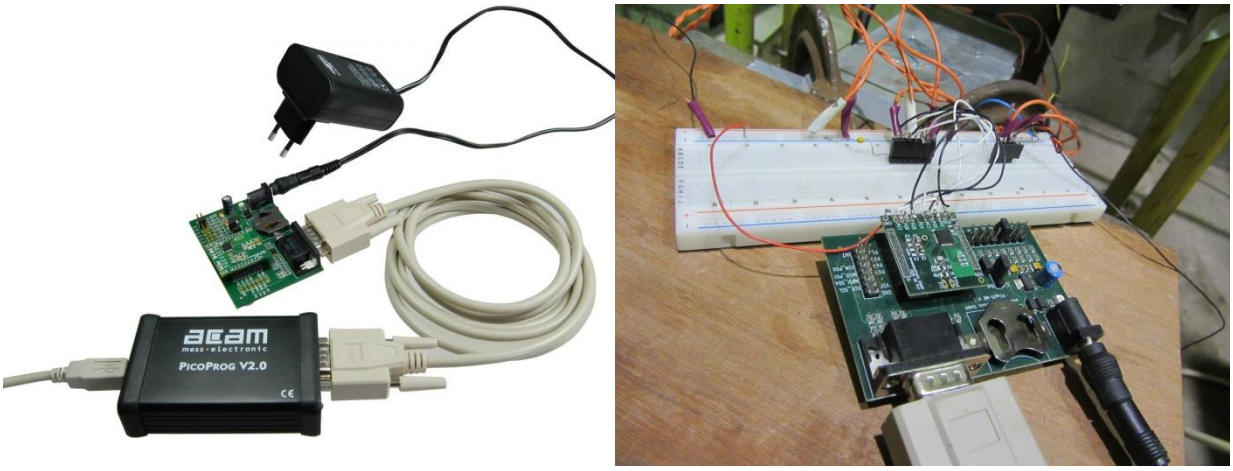

Figure 10: DAQ Acam PCap01-EVA-KIT [21].

2.3 Model Characterization and Experimental Verification

2.3.1 Model characterization

Based on the Eq. (7) derived in previous section, we are able to assume that strain data from one SEC satisfy the following equilibrium equation:

$$\varepsilon_s = \varepsilon_x + \varepsilon_y \qquad (Eq.9)$$

ε_s is in a unit of microstrain and is calculated by $\varepsilon_s = \frac{\Delta C}{C \times 2 \times 10^6}$. As long as the data taken from SECs were obtained, they are validated using the following equilibrium equation:

$$\varepsilon_s = \frac{\varepsilon_{x1} + \varepsilon_{x2}}{2} - \frac{\varepsilon_{y1} + \varepsilon_{y2}}{2} \qquad (Eq.10)$$

Where, ε_{x1} and ε_{x2} are readings from two RSGs along x-direction around a SEC, ε_{y1} and ε_{y2} are readings from two RSGs along y-direction around a SEC.

2.3.2 Experimental model verification

An aluminum plate with dimensions of 18 in. ×12 in. ×0.5 in. was selected to perform static loading tests. The plate was fixed on one of the short edges. The monitored plate surface was sanded and coated with acrylic enamel. The proposed sensors network was developed on the coated plate surface. Six soft elastomeric capacitors (SECs) were deployed by distributing a thin layer of epoxy on the plate surface, and they were numbered in two rows longitudinally. Seventeen resistance strain gauges (RSGs) were mounted and coated with water-proof solutions. Four RSGs were assigned to each SEC in order to measure strain along x and y directions, two RSGs for each direction. The AutoCAD drawing was provided below in Figure 11 with dimensions in details. The experimental setup for the entire plate is shown in the Figure 12.

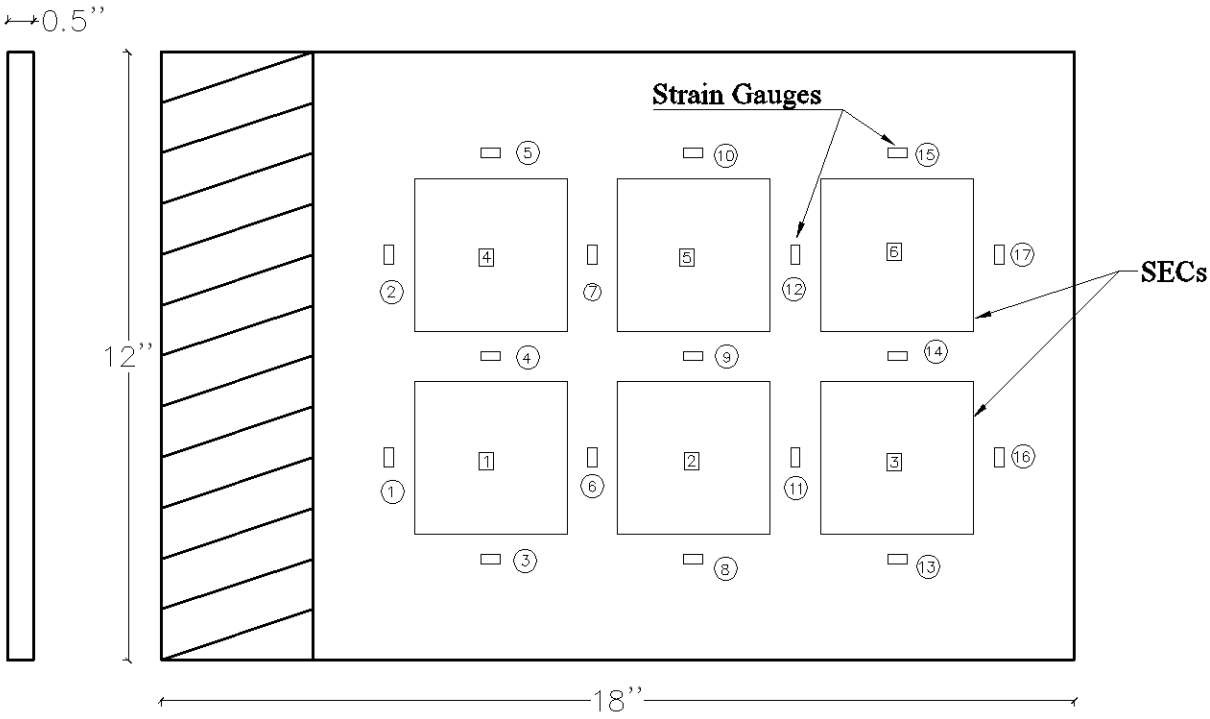

Figure 11: Aluminum plate dimension and distributions of SECs & RSGs.

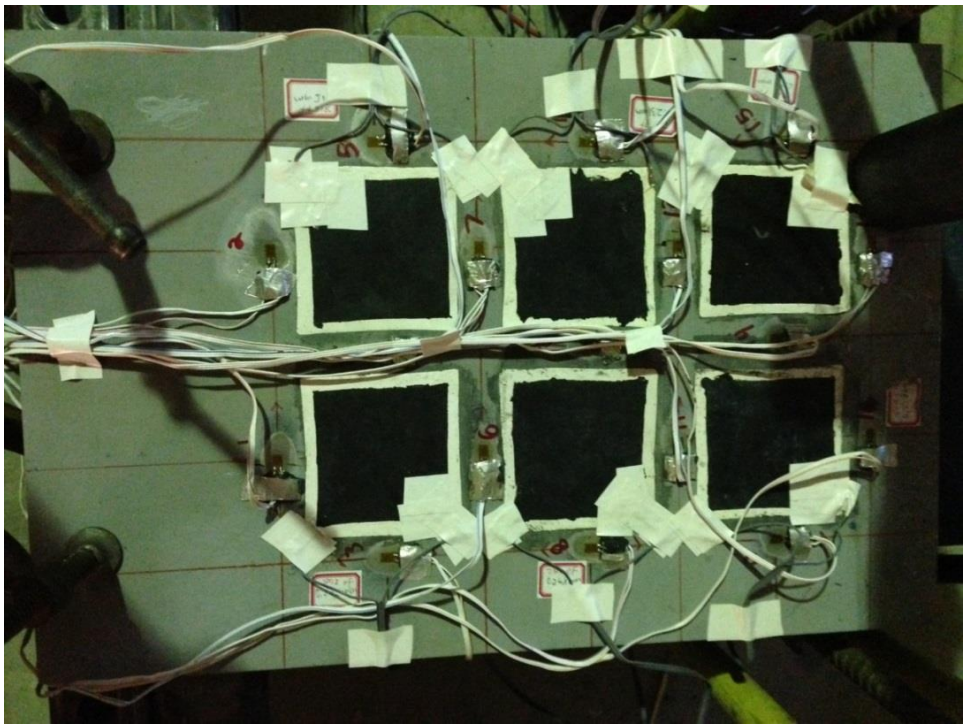

Figure 12: Experimental setup of the aluminum plate, SECs and RSGs.

The tests were conducted under three loading cases: point load at the center of the plate tip, point load at two corners of the plate tip. The load was applied by a hand-operated hydraulic test system. Tests were repeated three times for each loading case.

For SEC, data were obtained using an off-the-shelf data acquisition system (ACAM PCap01), sampled at 250.523 Hz. Strain gauges data were acquired using a Hewlett-Packard 3852 data acquisition system sampled at 2.176 Hz. The readings from SECs were to be compared against RSGs with resolution of 1με (Vishay Micro-Measurements, CEA-06-500UW-120).

2.3.3 Results and conclusions

Once the capacitance signals were recorded by DAQ, they were imported in MATLAB. The environmental noises of the signals were filtered by *filter* function by creating a numerator coefficient vector and a denominator coefficient vector in MATLAB. Strain signals could then be achieved after the transformation operation occurred in MATLAB. Strain data from RSGs were also recorded and compared with strains measured by SECs. Results from SEC #5 were taken and presented in Figure 13:

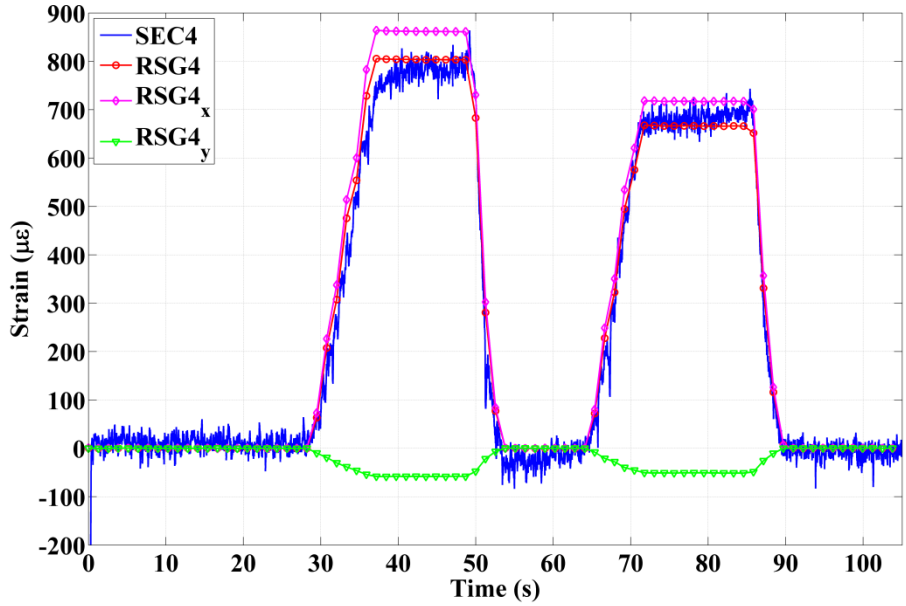

Figure 13: Strain results comparison between SEC #5 and surrounding RSGs.

As we can see in the figure, blue, pink and green lines represent the results from SEC #4, RSGs in the x-direction and RSGs in the y-directions respectively. According to the results from RSGs, 870$\mu\varepsilon$ and -70$\mu\varepsilon$ are identified to be the maximum values for ε_x and ε_y. A set of unidirectional strain data were calculated by averaging the strains from RSGs for both directions x and y, and it was visualized with a red line. By comparing the blue line and the red line, it is evident that the measurements taken by SEC unit have good agreements in values taken from traditional resistive strain gauges. Therefore, it can be concluded that the characterization of the model, which is shown in Eq. (9), has been approved to be rational to a certain extent. Once the assumption is validated, it can be then used to develop a strain fitting algorithm for strain decomposing assignment. The process will be presented in details in CHAPTER 3.

CHAPTER 3 ALGORITHM DEVELOPMENT AND VALIDATION ON SYMMETRICAL PLATE

3.1 Introduction

An algorithm that is based upon least square estimation has been developed to fit the strain surface, and then it was applied to decompose the unidirectional strain signals into two normal directions by estimating the coefficient matrix. According to Jingzhe Wu [22], both polynomial and biharmonic formulations can perform the task while a polynomial formulation works more accurately and effectively. Therefore, only polynomial formulation will be used in this study. The unidirectional strain signals were simulated using a FEM of a cantilever plate. The boundary conditions were determined as fixed-free because it is the same boundary conditions as wind turbine blades. Therefore, the flexural analysis on the plate is of considerable importance. Also, a simple plate is an ideal model to be investigated for verifying the proposed algorithm for strain decomposition of an SEC unit. To perform a decent analysis of a simple plate, it is important to employ a powerful computer-aided tool in order to predict the behavior of plate accurately. Finite element (FE) software is one of the most reliable choices to analyze the behavior of the plate. A cantilever plate with 0.805m (length) by 0.7m (width) by 0.02m (thickness) was taken and analyzed using FE software ANSYS. The fixed-free boundary conditions were decided in order to simulate the behavior of the wind turbine blade in the real applications. The general aluminum material properties were used to specify a real constant of the element. Three different loading cases were applied to simulate various loading conditions in realistic situations as well as to test the performance of the proposed algorithm: (1) a

concentrated load at the center tip, (2) a concentrated load at the corner tip, and (3) a uniform pressure over the entire plate,. First the finite element modeling of the cantilever plate in ANSYS will be demonstrated. Afterwards, the development of the algorithm is provided in details because the algorithm can be applied once the unidirectional strain signals were extracted from FE analysis results. Lastly, the decomposed results are described in how they were obtained and compared with exact values from ANSYS under different loading cases.

3.2 Rectangular Plate Modeling in ANSYS

Starting with a simple situation, an aluminum plate with dimensions of 0.805m (length) by 0.7m (width) by 0.02m (thickness) was examined. The dimension of the plate was designed on purpose in order to have enough space to adopt a 7 by 8 matrix of SECs. The fixed-free boundary conditions were determined in order to be consistent with the boundary conditions for wind turbine blades. The material properties can be found in Table 1.

Table 1: Material properties of aluminum.

Density (kg/m^3)	2700
Young's Modulus (Pa)	7×10^{10}
Poisson Ratio	0.35

In ANSYS, the model was created by defining the dimensions of the plate using Create-Area command. Element type SHELL181 was used to define the plate. According to the ANSYS user manual, SHELL181 is a suitable element for analyzing thin shell structures. Each element has four nodes with 6 DOFs for each node (translations in x, y, z and rotations in x, y, z). It is well-suited for linear, large rotation, and/or large strain nonlinear applications. Change in

shell thickness is also accounted for nonlinear analysis. In addition, SHELL181 can be used for layered applications for modeling composite material properties like those in a wind turbine blade. The geometry, node locations, and the element coordinate system for SHELL181 are shown in Figure 14. For element type options, bending and membrane were chosen for K1 (element stiffness) and all layers were used for K8 (storage of layer data), respectively.

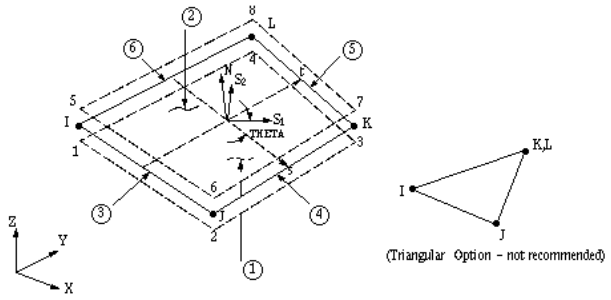

Figure 14: Geometry, node locations and element coordinate system for SHELL181.

Once the element type was assigned to the model, material properties and real constant were specified. In this case, linear isotropic material was used. Mesh was generated by defining mesh size manually as 0.035m for considering both computing effectiveness and convenience of assigning SECs locations. The boundary conditions were that one of the short edges was fixed and the other threes boundaries were free. The completed plate finite element model is shown in Figure 15. Geometry, element size, and boundary conditions are included.

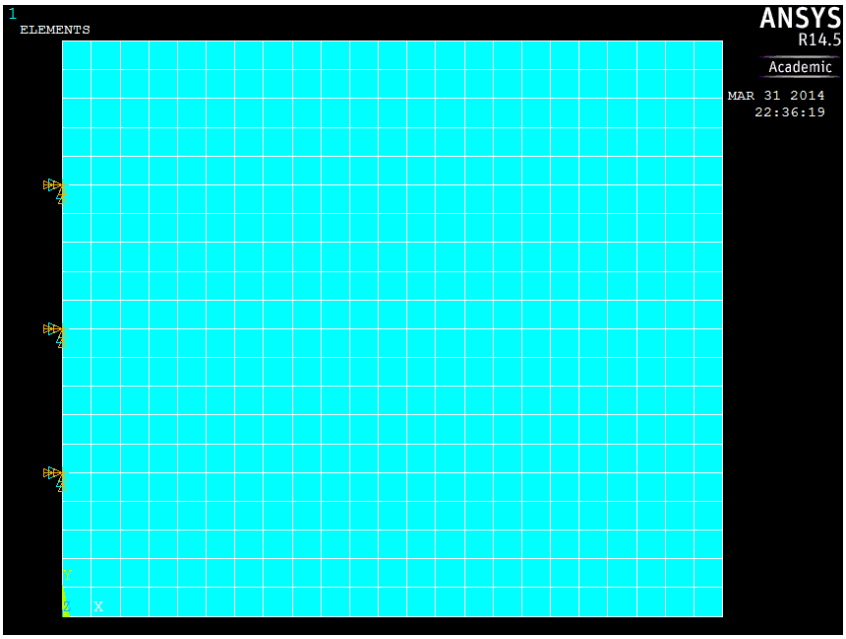

Figure 15: Completed finite element model of the plate.

3.3 Dynamic Analysis Configuration in ANSYS

Transient dynamic in ANSYS is a technique that can be used to determine the dynamic response of a structure under any general time-dependent loads. For our case, it is well-suited to perform an analysis that needs to determine time varying strain. The basic equation of motion solved by transient dynamic analysis is the following:

$$m\ddot{u} + c\dot{u} + ku = p(t) \qquad (Eq. 11)$$

In total, three different loading cases were performed on the plate: (1) a concentrated load at the center tip, (2) a concentrated load at the corner tip, and (3) a uniform pressure over the entire plate. The basic format of harmonic equation was used for load functions: $f(t) = Psin(\pi t)$. Based on the classical thin plate theory, it was considered to be a small deflection if the maximum plate deflection is relatively small when comparing against its thickness, 0.02m in this case. Therefore, multiple harmonic load equations were assumed, tested, and adjusted, and

three final versions listed in Table 2 are utilized. Maximum deflection of the plate for each case was calculated in ANSYS, and it was recognized with an acceptable level comparing it to plate thickness.

Table 2: Harmonic load functions for three loading cases.

Loading Cases	Load Functions, (N), (N/m^2)	Maximum Deflection (m)
Point Load at Center Tip	$P(t) = 1500 \times sin(0.25\pi t)$	0.0102
Point Load at Corner Tip	$P(t) = 2000 \times sin(0.25\pi t)$	0.0099
Uniform Pressure on plate	$P(t) = 10000 \times sin(0.25\pi t)$	0.0104

The solutions control configuration for transient analysis was demonstrated, and it is shown in the following figures. The duration for dynamic analysis was 10 seconds with 0.2 seconds of time increment, which results in 50 load substeps in total. Ramped loading was selected, and it increased the load linearly from the previous substep's level to the most current substep's final value. Nodal and element solutions for strain, stress and displacement were written into the results files for every load substep. Furthermore, it is also necessary to point out that when extracting results from ANSYS, nodal strains were taken from the top layer of the plate on a global coordinate basis.

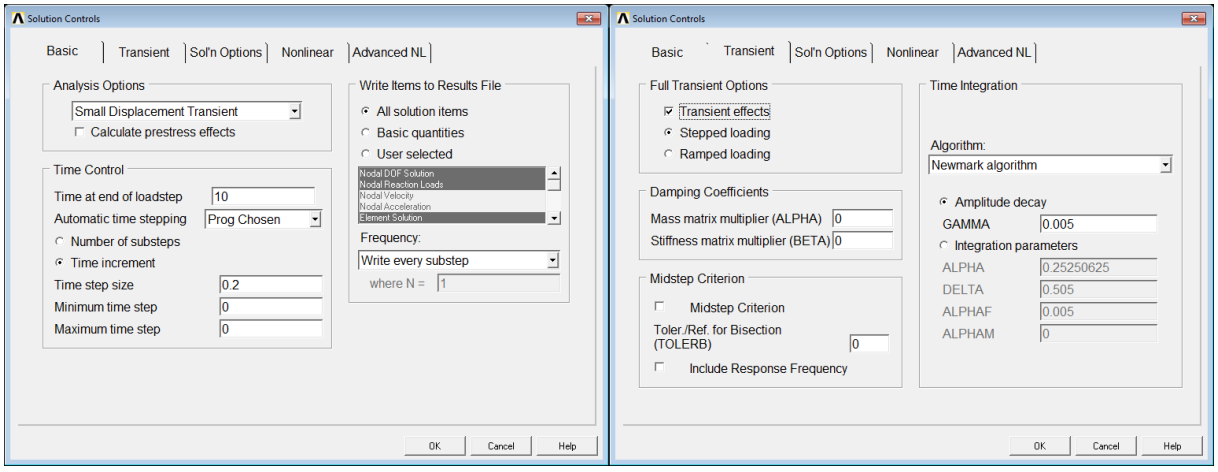

Figure 16: Solution control of transient analysis in ANSYS.

3.4 Strain fitting Algorithm

3.4.1 Applications of least square estimation

Least square estimation is a very common method utilized to find the approximate solution for overdetermined systems. The main process involves estimating parameters by minimizing the sum of the squares of the errors between the observed data and the expected data. The method has been widely used in structural engineering, such as in shape reconstruction. Tessler et al. used a least squares variational method for the inverse problem of full-filled reconstruction of elastic deformations in plates and shells. The authors used a completed set of strain measurements that are consistent with first order shear deformation theory to minimize the errors. A simple plate subjects bending was taken as an example to demonstrate how the displacement solution was reconstructed from the discrete strain measurements using the proposed algorithm. The results show that the method is able to exactly predict the displacement response, if the exact strains are used. The authors also concluded that the proposed algorithm can be used for real-time structural health monitoring applications with the full power of the finite element method [23]. Glaser R et al. developed a least square-based method that uses strain or/and curvature data to reconstruct the shape of a beam. The study compared the reconstruction results using three sets of input: (1) displacement, (2) strain, and (3) a combination of displacement and strain. Moreover, the proposed method was compared against traditional reconstructions techniques using position data and combined data as input. The goal was to develop an efficient method for real-time shape monitoring of beam type structures [24]. Nishio M et al. presented a shape reconstruction algorithm using a finite element model of the target structure. The application of the algorithm, which started with estimating the strain functions

using least square estimator, was conducted on a composite laminate specimen. The input strain data were acquired by a group of Brillouin-scattering-based optical fiber sensors, which were embedded into the specimen. It was found that the accuracy of reconstruction can be greatly improved by using weight values that were determined from the non-uniformity index of the strain distribution profile [25]. According to Jones R T et al. [26], a strain surface fitting algorithm had been developed to determine the full deformation filed of a cantilever plate, which subjects arbitrary loading conditions. Sixteen fiber bragg grating sensors were mounted on the target plate to harvest the strain information. A two-dimensional polynomial function was assumed to represent the normal strain in longitudinal direction. Sequentially, the coefficients of the assumed function were evaluated by minimizing errors between measured strain values and predicted values. Based on the plate theory, the displacement field can be derived by integrating the strain function twice. By comparing the results with experimental data, it is found that the algorithm is able to predict the displacement with acceptable accuracy.

The strain surface fitting algorithm utilized in this thesis is also based upon least square estimation. It will be presented and illustrated in details in the following section.

3.4.2 Strain fitting algorithm development

The bidirectional nodal strain data that extracted from ANSYS simulation were used to construct signals for SECs by summing strain in x and y directions, from Eq. (9):

$$\varepsilon_s = \varepsilon_x + \varepsilon_y \qquad (Eq.9)$$

The relationship shown above was drawn from the sensing principal and assumption made in CHAPTER 2. Two polynomial functions that represent strain in x and y directions are needed to be assumed in order to create and fit strain map of the plate. Also, based on the classical plate theory, the following relationships exists between strain and displacement [27]:

$$\varepsilon_x = -z\frac{d^2w}{dx^2} \;\; and \;\; \varepsilon_y = -z\frac{d^2w}{dy^2} \qquad (Eq.12)$$

Where, $\varepsilon_x \; and \; \varepsilon_y$ denote to normal strain in x and y directions, w represents out-of-plane displacement, and z is the distance from the surface to the centroid of the plate. Therefore, a polynomial function that is able to represent the displacement of cantilever plate needs to be developed. Selecting the order of the polynomial displacement model requires satisfying completeness and compatibility conditions. In addition, the pattern of the function should be independent of the orientation of the local coordinate system. which is the geometric isotropy property. Pascal triangle for two-dimensional polynomial equation was therefore used as a basic rule. In accordance with the results taken from multiple tests using various trial functions, the order of the function was optimized as sixth for the plate in both x and y orientations:

$$\mathrm{w(x,y)} = \sum_{i=0,j=0}^{n} a_{i,j}x^i y^j \qquad (13,5)$$

Where $n = 6, \; a_{0,0} \ldots a_{n,n}$ are parameters that need to be solved. It is needed to notice that $a_{0,0}$ should be eliminated due to cantilever plate boundary conditions at the fixed end, x and

y are coordinates at node of interest. The polynomial functions for ε_x and ε_y then can be obtained by taking partial differential equations showing in Eq. (12) with respect to x and y, respectively, and they are represented in the following form:

$$\varepsilon_x = \boldsymbol{A_x C_x} \qquad (Eq.14)$$

$$\varepsilon_y = \boldsymbol{A_y C_y} \qquad (Eq.15)$$

By summing Eqs. (14) and (15):

$$\varepsilon_s = \boldsymbol{AC} \qquad (Eq.16)$$

Where, $\boldsymbol{C_x}$, $\boldsymbol{C_y}$ and $\boldsymbol{C}$ are sensor placement matrices. As soon as the strain functions were defined, strain map for the plate was fitted using least square algorithm by first estimating coefficients $\boldsymbol{A}$ matrices by minimizing error E for n sensors:

$$E = \sum_{i}^{n} (\varepsilon_i - \widehat{\varepsilon_i})^2 \qquad (Eq.17)$$

Where, the *hat* denotes an estimated value for i^{th} sensor, Eq. (17) leads to:

$$\widehat{\boldsymbol{A}} = (\boldsymbol{C}^T \boldsymbol{C})^{-1} \boldsymbol{C}^T \varepsilon_s \qquad (Eq.18)$$

Before estimating $\boldsymbol{A}$ matrix, boundary conditions for plate boundaries need to be investigated and enforced into the coordinate matrix.

At the fixed end, $\varepsilon_y = 0$:

$$\frac{\varepsilon_y}{\varepsilon_x} = 0 \;\; or \;\; \varepsilon_s = \varepsilon_x \qquad (Eq.19)$$

At the top and bottom edges:

$$\frac{\varepsilon_y}{\varepsilon_x} = -\upsilon \quad \text{or} \quad \varepsilon_s = (1-\upsilon)\varepsilon_x \qquad (Eq.20)$$

Where, υ is the Poisson's ratio of aluminum, Eq. (20) was obtained by substituting $\sigma_y = 0$ into the following stress strain relationship [28]:

$$\sigma_y = \frac{E}{1-\nu^2}\left(\varepsilon_y + \upsilon\varepsilon_x\right) \qquad (Eq.21)$$

Where E is Young's modulus. Eq. (21) was yielded by solving constitutive equations through Hooke's law for stress components σ_x, σ_y [28].

At the free end:

$$\frac{\varepsilon_y}{\varepsilon_x} = -\frac{1}{\upsilon} \quad or \quad \varepsilon_s = \left(1-\frac{1}{\upsilon}\right)\varepsilon_x \qquad (Eq.22)$$

Similarly, Eq. (22) can be derived by substituting $\sigma_x = 0$ into:

$$\sigma_x = \frac{E}{1-\upsilon^2}\left(\varepsilon_x + \upsilon\varepsilon_y\right) \qquad (Eq.23)$$

In accordance to Huang et.al (2003) [29], stress singularities in elastic plate frequently occur due to boundary conditions along the plate edges, especially for sharp corners. Based on the investigation of simulation results extracted from ANSYS, the BCs on two corners along fixed end were interfered by BCs on the two sides and the fixed end. Thus, it was determined to take it into account by averaging BCs in Eqs. (19) and (20) for fixed end corners:

$$\frac{\varepsilon_y}{\varepsilon_x} = -\frac{\upsilon}{2} \quad or \quad \varepsilon_s = \left(1-\frac{\upsilon}{2}\right)\varepsilon_x \qquad (Eq.24)$$

For two corner nodes on the free tip, the BCs appear to change unpredictably by investigating the simulation results. Consequently, no BCs were enforced for those two corners. Once aforementioned boundary conditions were enforced into the coordinate matrix, matrix $\boldsymbol{A}$ can be obtained and then $\widehat{\varepsilon_x}$ and $\widehat{\varepsilon_y}$ were able to be evaluated by substituting $\boldsymbol{A_x}$ and $\boldsymbol{A_y}$ back into Eqs. (14) and (15). The results of estimated strain map are presented in the next several sections regarding different loading cases and sensor arrangements for the rectangular cantilever plate.

3.5 Validation of the Proposed Algorithm

A group of the sensors consisting of 56 SECs were deployed to perform multiple test to evaluate the performance as well as to verify the accuracy of the proposed strain fitting algorithm. The sensors were uniformly organized in a 7 by 8 matrix form. The total number of the sensors was decided by considering both estimating accuracy and computational effectiveness.

One of the governing factors to achieve decent estimations in strain fitting algorithm is evaluation of coefficient matrix $\boldsymbol{A}$, which involves the inversion problem of coordinate matrix $\boldsymbol{C}$. In fact, the strain between adjacent SEC units along x or y direction is approximate linearly distributed for small deformation. In other words, one or more predictor variables in the model are correlated so that one could be linearly estimated from the others with a nontrivial degree of accuracy. In this case, a multicollinearity problem usually arises when an approximate linear relationship exists among one or more independent predictor variables. This problem could lead to inaccurate results of matrix inversion, or even results in an invertible matrix due to a high degree of multicollinearity. Consequently, boundary conditions of bending thin plates were

implemented and enforced into coordinate matrices in order to make the matrix invertible by increasing the rank. As it has been mentioned in the previous section, boundary conditions for two corners along fixed edge were derived by combining the boundary conditions along fixed end and top/bottom side, and no BCs were enforced for the two corner nodes along the free tip.

Considerations for arranging SECs around boundaries were taken from both idealized and realistic points of view: (1) For an idealized situation, the sensors should be placed right on the four boundaries (see Figure 17) in order to yield strain information as accurately as possible when enforcing boundary conditions; in other words, the closer the sensors are placed on boundaries, the more accurately the measured strain can match with theoretical boundary conditions; (2) In reality, it is difficult to attach sensors right on the boundaries due to the relative large dimension of SECs (7cm by 7cm); thus, all SECs along four sides have been moved toward the inner area of the plate by 3.5cm, as is given in Figure 18.

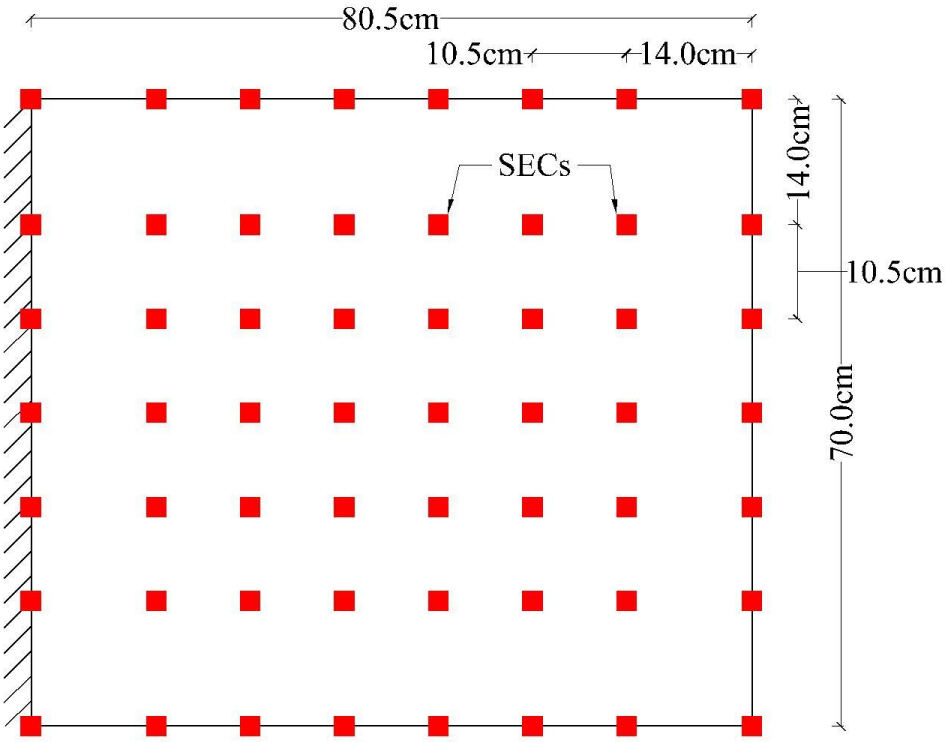

Figure 17: Arrangement of SECs (idealized).

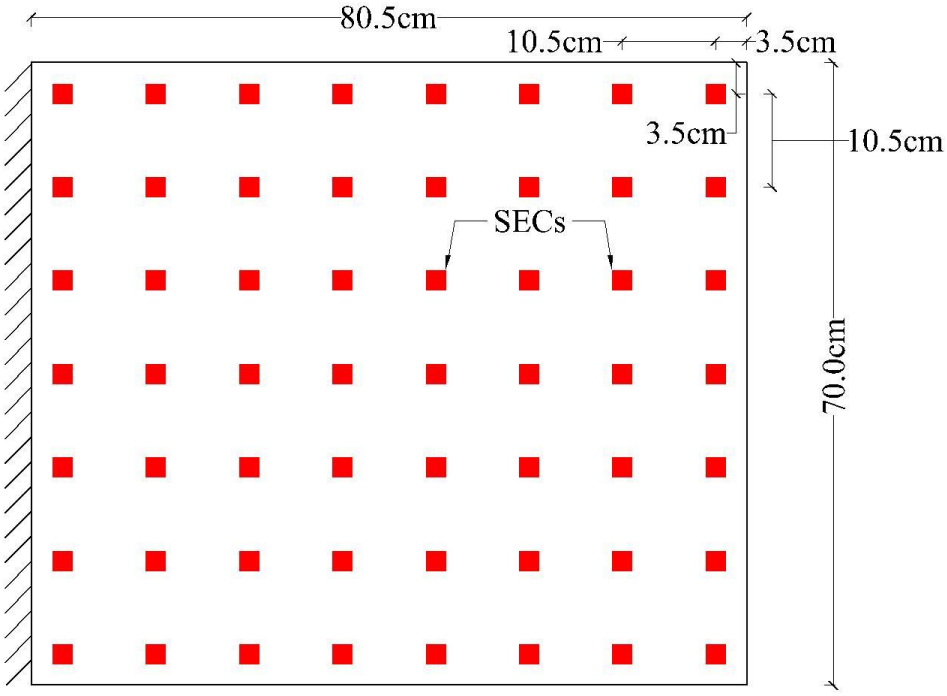

Figure 18: Arrangement of SECs (realistic).

3.5.1 Results of idealized secs arrangement for all load cases

Three transient load cases given in Table 2 were applied out-of-plane in sequence to the plate. The load locations on the plate are shown in Figure 19. The real bidirectional strain data were extracted and compared with estimated bidirectional strain obtained using proposed algorithm. The results from all three load cases were presented and compared simultaneously. The results for strain surface plots included strain data from all sensors; meanwhile the contour plots and time series plots for mean absolute percentage error, and root mean square of absolute error were only presented for inner sensor locations. In other words, strain data from all sensors located on four boundaries were excluded.

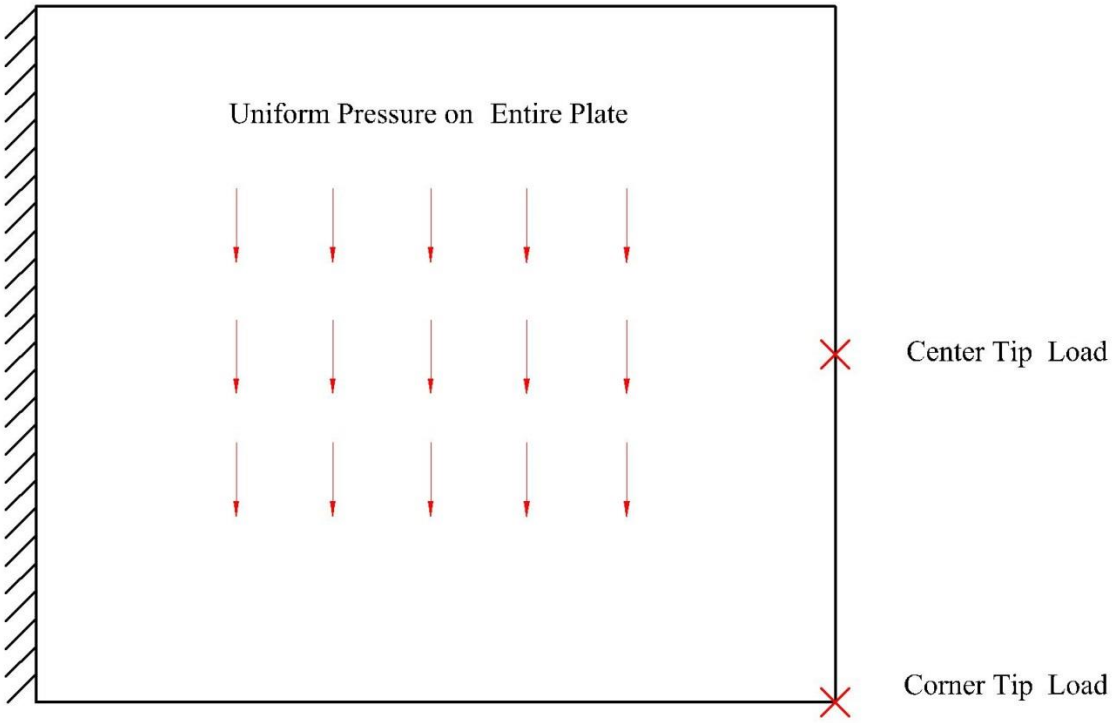

Figure 19: Schematic of three load cases on the plate.

3.5.1.1 Strain Surface Fitting Results

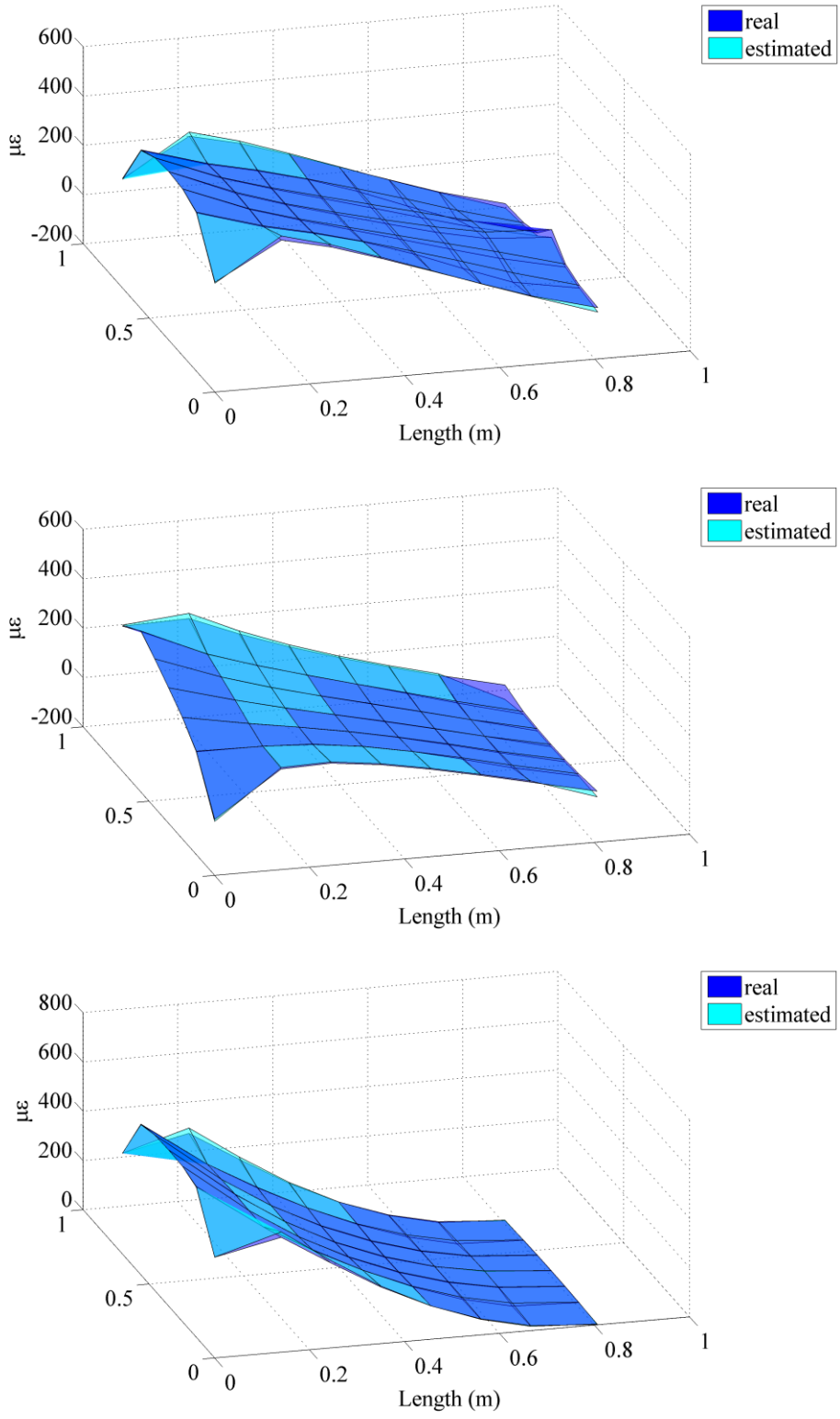

Figure 20: StrainX strain fitting for all load cases: center tip, corner tip, pressure (idealized).

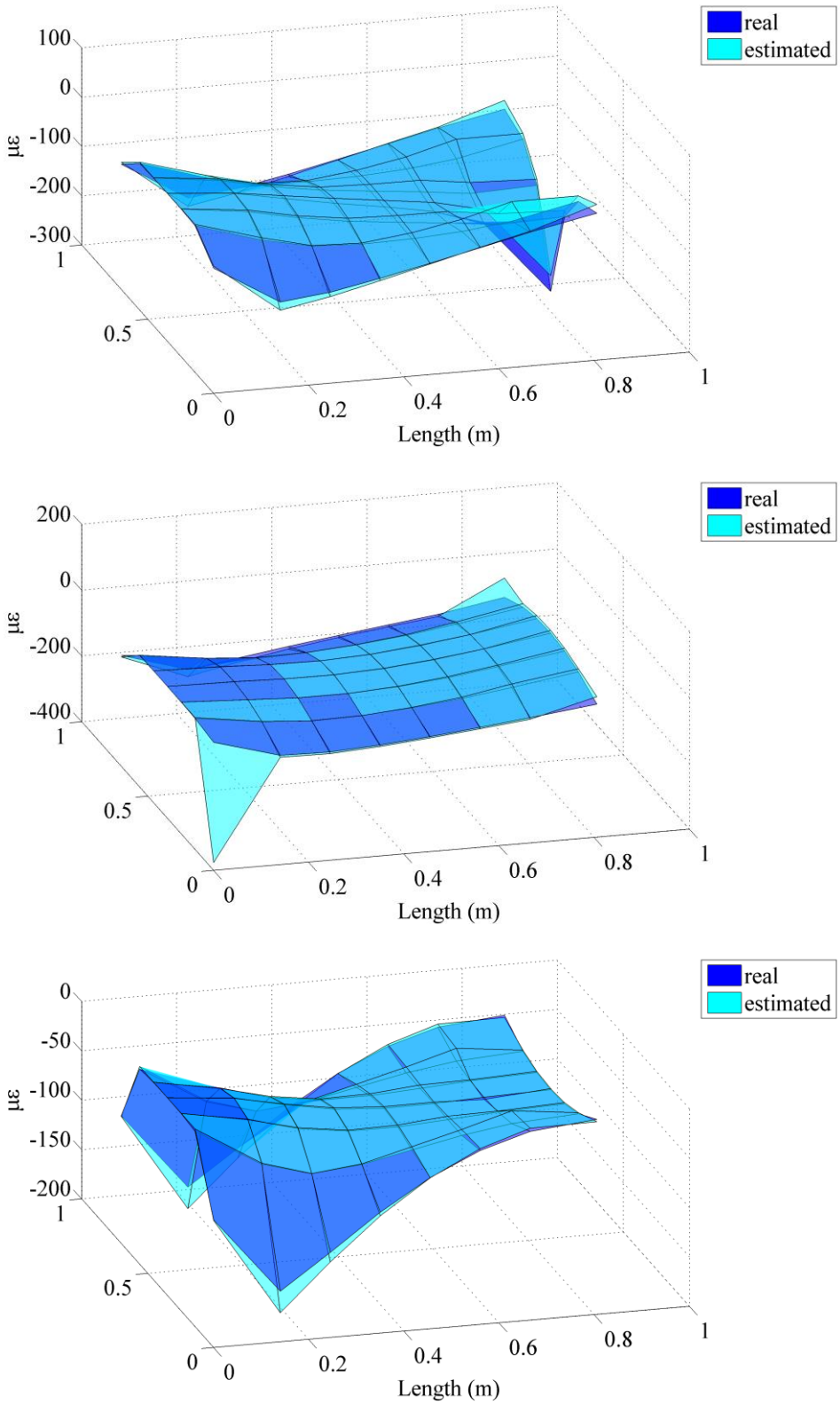

Figure 21: StrainY strain fitting for all load cases: center tip, corner tip, pressure (idealized).

The surface fitting results shown above for both x- and y-directions are taken at the 30th load step, which corresponds to the peak load amplitude. From the plots, the maximum strain in x-direction takes place near the clamped edge and decreases to zero at the tip of the plate, which makes sense because the stress in x-direction is maximum at the fixed-end and minimal at the free-tip; the trend is shown to be opposite for strain y of inner plate area. It starts from zero at the fixed end and keeps increasing toward the free end. In the meantime, strain y near the top and the bottom free sides show the same tendency with strain in x-direction, which matches the assumed boundary conditions for the thin plate. In general, the estimated strains have good agreements with the real strain data for all three loading cases. By comparing the results for both directions, it is found that the overall predicting accuracy for strain x is better than strain y. In addition, strain x around internal area and boundaries close to the second half of the plate has been underestimated, which is in accordance of overestimations of strain y for the same region. For concentrated load on both center and corner tip, we can see the estimating error becomes relatively large at the points where the loads are applied as well as for boundary corners. Moreover, it is noticed that under the corner concentrated load, there is a spike in strain y at left bottom corner along clamped edge. This spike is probably because the combination BCs for these two nodes can no longer hold since the corner load is inducing torsion effect for the plate while the BCs are derived from thin plate bending behaviors.

3.5.1.2 Mean Absolute Percentage Error (MAPE) on Entire Plate

The percentage error of estimation for each sensor node has been calculated for each time step, and the mean value was obtained by averaging absolute percentage error for all nodes from all time steps. The equation of MAPE is given as follows:

$$MAPE = \frac{1}{n}\sum_{t=1}^{n}\left|\frac{\varepsilon - \hat{\varepsilon}}{\varepsilon}\right| \times 100\% \qquad (Eq.25)$$

Where n = 50, which is the total number of time steps. It should be noticed that MAPE is only calculated for inner sensor locations, that is, strain data from all sensors located on four boundaries are excluded.

Contour plots of MAPE for ε_x and ε_y are presented in Figure 22 and Figure 23, respectively. The distributions of errors for load cases of center tip and pressure are approximately symmetrical along the center line of the plate which coincides with the author's expectation because both load cases were generating almost pure bending. It can be easily observed that the maximum percentage errors are concentrated at two corner nodes along the free edge for both ε_x and ε_y. This concentration is probably because no BCs were applicable for these two corner nodes when performing boundary condition enforcement. Consequently, the operation of matrix inversion could be inaccurate due to information absence for the two free tip corners. From the contour plots, it is noticeable that the regions close to these two corners have been influenced accordingly, and errors were gradually decreasing toward the clamped edge of the plate. For ε_y, 45% is recognized as the maximum percentage error in the load case of uniform pressure; meanwhile the maximum error of 126% occurs at points where the corner tip load was applied. For ε_x, however, the maximum error of 22% from corner load case is marked as the

smallest error compared to the others. Thus, it can be concluded that torsion of the plate has much more effect for $\varepsilon_y$than ε_x. The estimating accuracy for inner plate area has been identified as more sensitive to the two free corners under center tip loading than the other two load cases. In terms of overall performance, the algorithm works more steadily under uniform pressure loading since the percentage error for both $\varepsilon_x$and ε_y are pretty close. More importantly, the errors of areas near clamped edge have been controlled within 5% and 20% for $\varepsilon_x$and ε_y, which is meaningful since areas near the fixed-end are vulnerable and suffer significant stresses.

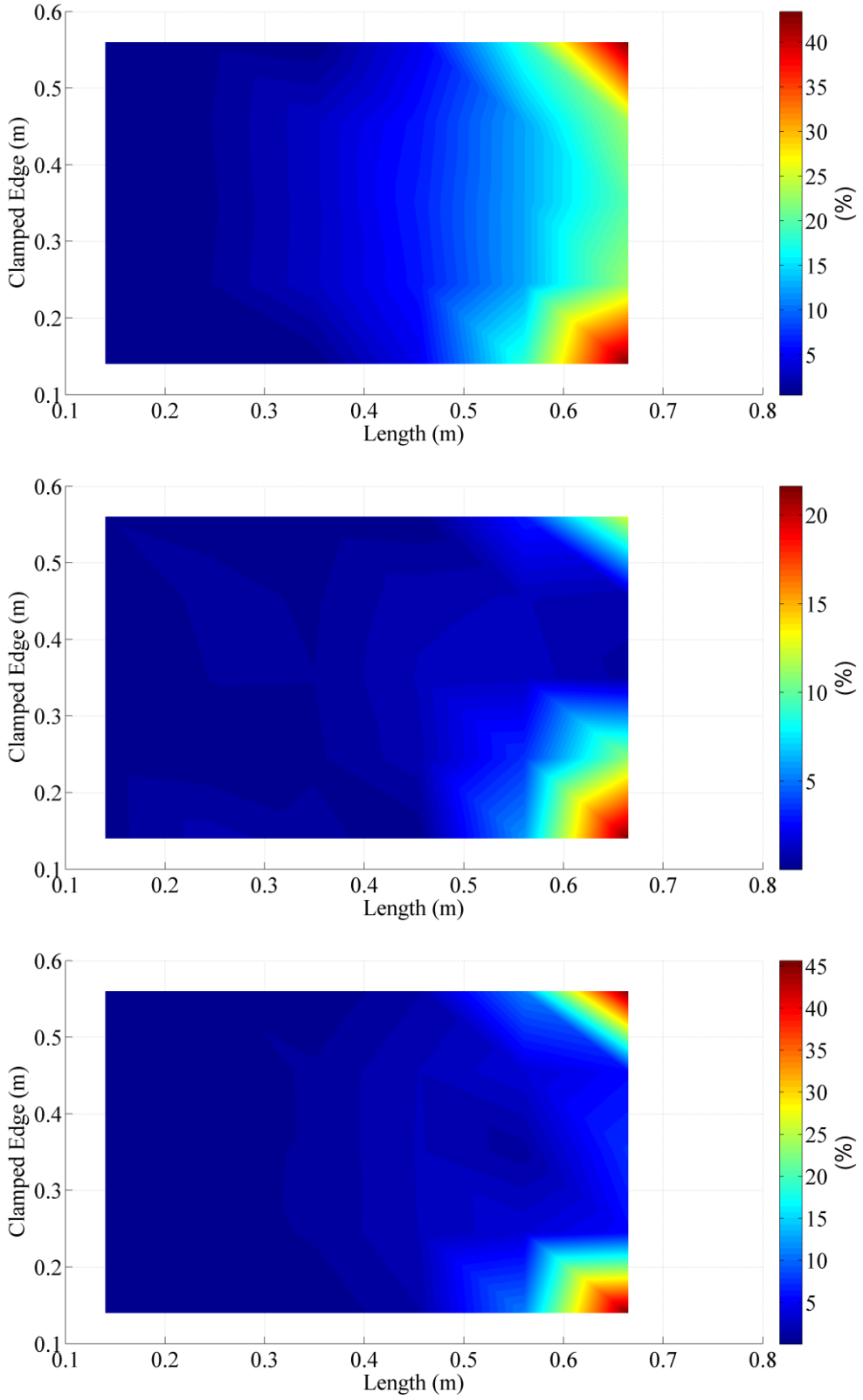

Figure 22: StrainX MAPE for all loading cases: center tip, corner tip, pressure (idealized).

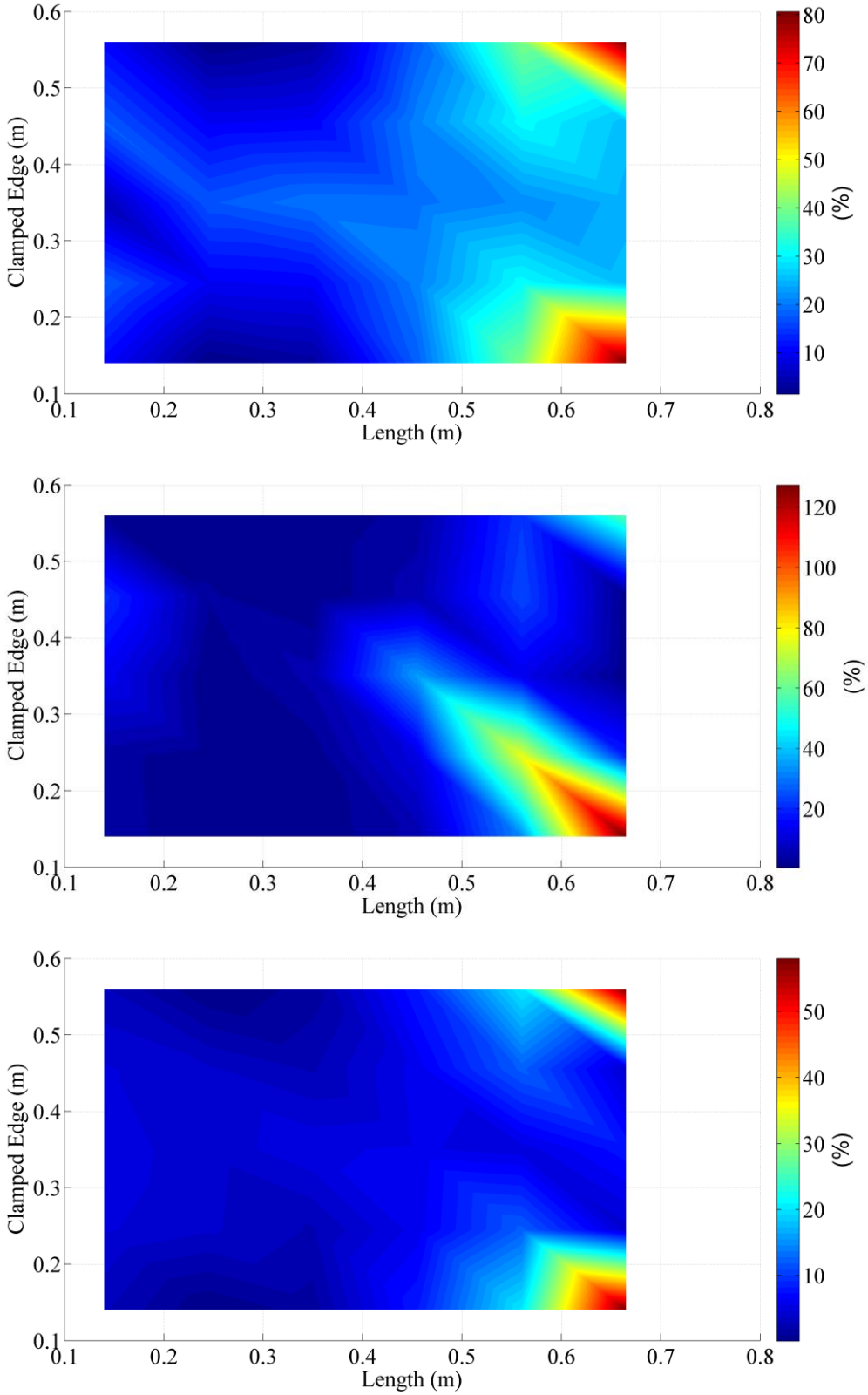

Figure 23: StrainY MAPE for all load cases: center tip, corner tip, pressure (idealized).

3.5.1.3 Mean Absolute Percentage Error (MAPE) on Entire Plate over Time Series

In the previous section, the percentage error has been presented over the entire plate by averaging all the time steps for each sensor node. At this point, only one percentage error has been calculated for the entire plate by averaging all sensor nodes for each load step. Then, Figure 24 and Figure 25 were obtained by plotting each percentage error versus each load step for all three load cases; and also, only the data from inner sensor nodes were extracted and presented. These plots are helpful to investigate and understand how the amplitude of load affects the estimating accuracy of the algorithm.

As we can see in the plots, the blue line represents the MAPE over all the plate, while the green line shows the load amplitude's change over time series. For ε_x, the percentage errors are roughly around 9.3%, 2.1% and 5.1% for the center load, the corner load, and the pressure respectively; in the meantime, 22%, 16.8% and 9.3% are marked on the plots for $\varepsilon_y$under three load cases. Hence, it is undeniable that the performance of the algorithm performs better under uniform pressure than under concentrated load in terms of both directions. In addition, the algorithm has been validated since the errors are shown to be very stable over the change of amplitudes of all loading cases, namely, the accuracy level of the algorithm is independent of load amplitudes. Lastly, we can clearly observe that there are two noticeable spikes in each plot at the point which load amplitude is zero. The errors were either suddenly dropping or jumping for all loading cases, while the magnitude of errors changed are relatively small, probably because of the effect of zero load amplitudes, which result in zero strains over the plate. The specific reason still needs to be investigated. The points adjacent to zero load points, however, are shown to have no affect possible. Thus, the spikes could be negligible because no significant events will happen when applied loads are almost zero.

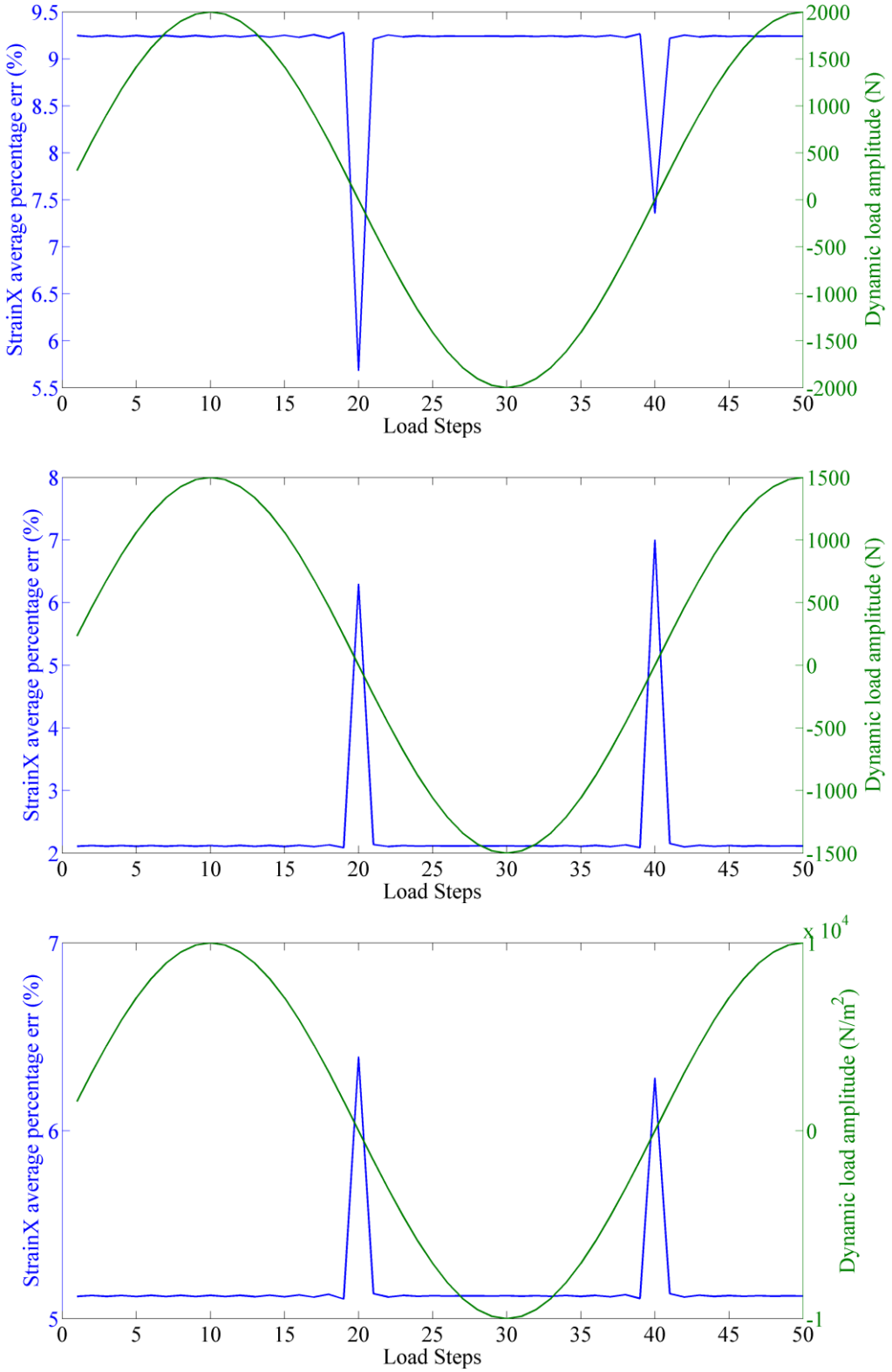

Figure 24: StrainX MAPE MPAE of entire plate over load steps for all load cases: center tip, corner tip, pressure (idealized).

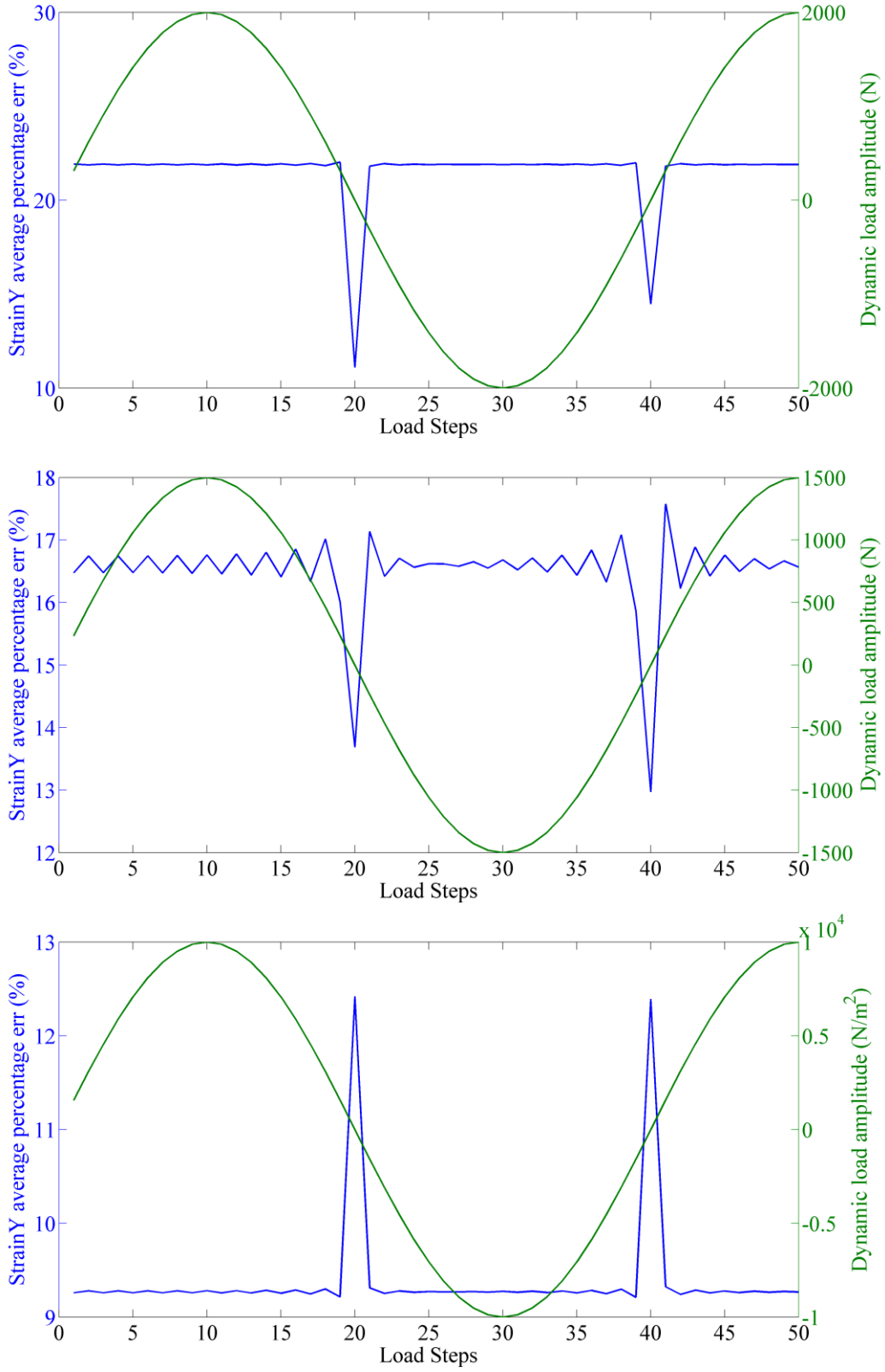

Figure 25: StrainY MAPE MPAE of entire plate over load steps for all load cases: center tip, corner tip, pressure (idealized).

3.5.2 Results of realistic secs arrangement for all load cases

3.5.2.1 Strain Surface Fitting Results

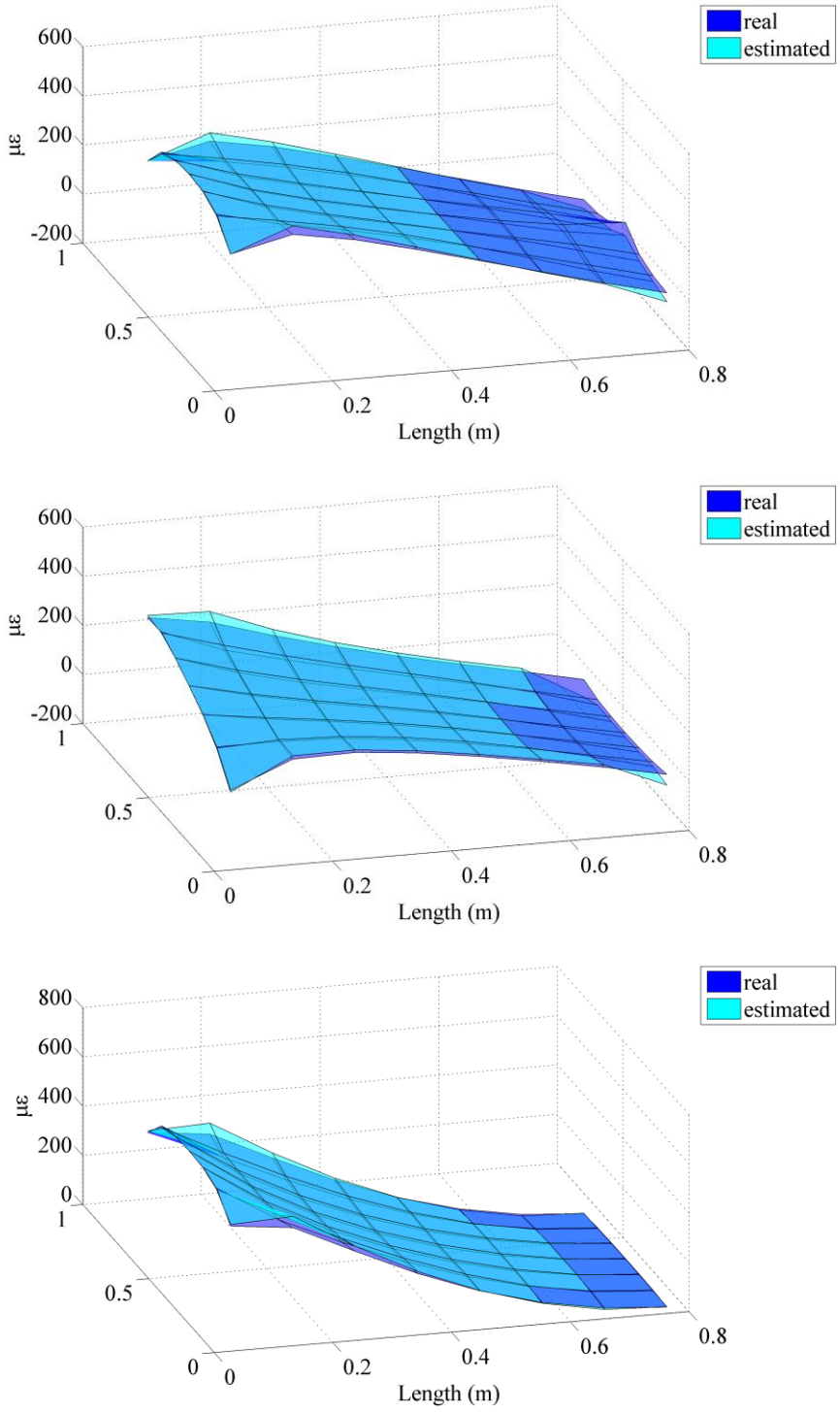

Figure 26: StrainX strain fitting for all load cases: center tip, corner tip, pressure (realistic).

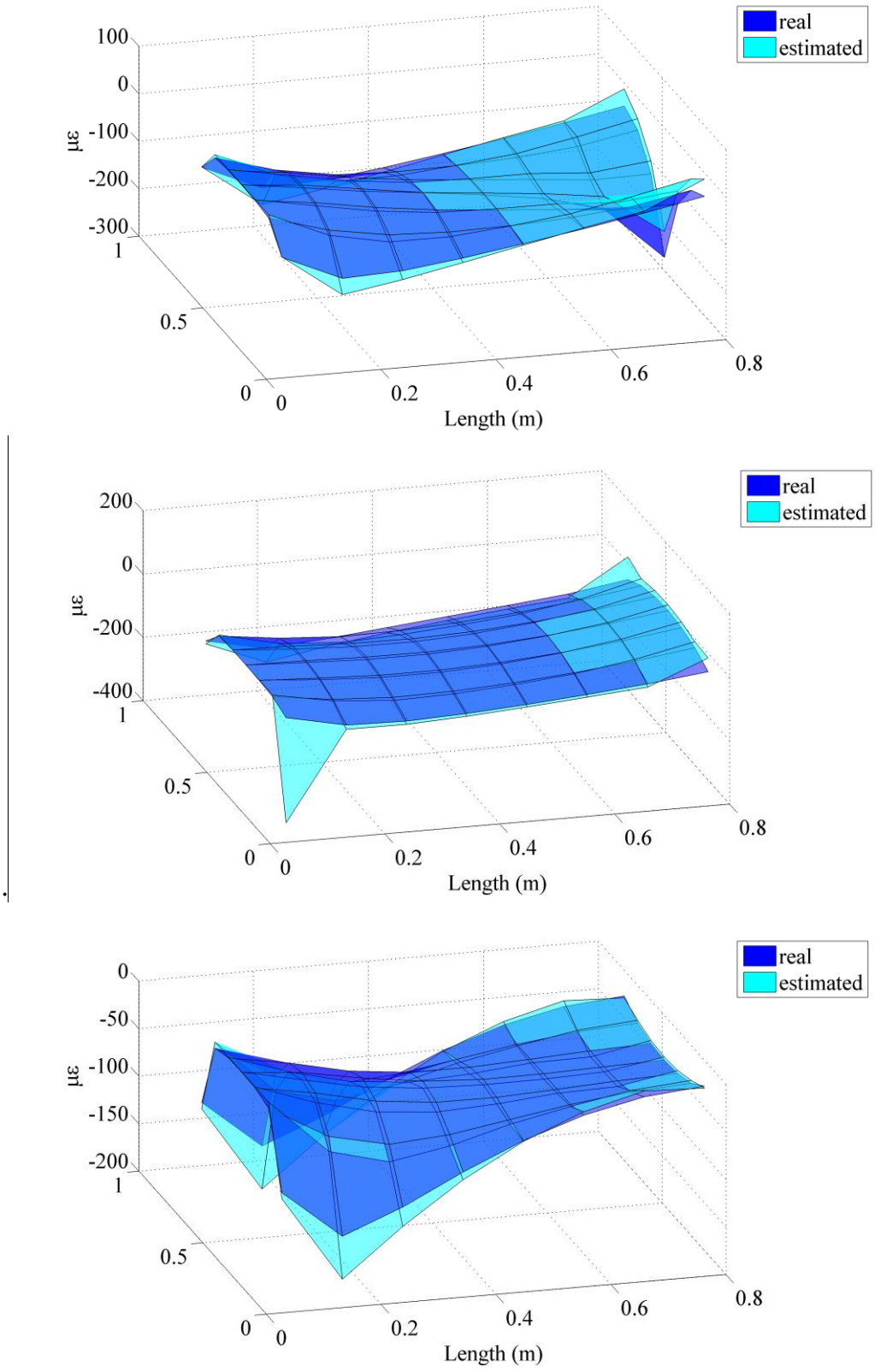

Figure 27: StrainY strain fitting for all load cases: center tip, corner tip, pressure (realistic).

As shown in Figure 26 and Figure 27, the trends and the shapes for realistic sensor arrangement are very similar to the results shown in the previous section for idealized sensor arrangement. By comparing results from two sensor arrangements, however, we found that the algorithm is generally overestimating for ε_x (underestimating for ε_y) under realistic arrangement while is shown to be underestimating for ε_x (overestimating for ε_y) under idealized sensor placement.

3.5.2.2 Mean Absolute Percentage Error (MAPE) on Entire Plate

The mean absolute percentage error contour plots are presented in Figures 28 and 29. The maximum error for ε_x is 25% under center load and for ε_y is 190% under the corner load. It also can be easily observed that for each load case, the large errors of ε_x focus on most of tip areas. By contrast, the large errors for ε_y are unlikely following a certain pattern, but most of large errors concentrate close to fixed end. For the center tip load, the errors are also relatively large around two free end corners, which are not showing for the other two load cases. In addition, the distribution of the error of ε_y is more discrete on the entire plate than ε_x. The error map for ε_x under pressure has a minimum range of 2% to 12% whereas the minimum error range for ε_y is from 4% to 47% for the center load. In the case of corner load, the estimating accuracy of ε_y is more sensitive than the one of $\varepsilon_x$for the effect of torsion. Taken as a whole, the performance of the algorithm under pressure is relatively better for both directions in terms of the fact that most of the errors are under 7% for ε_x and under 30% for ε_y.

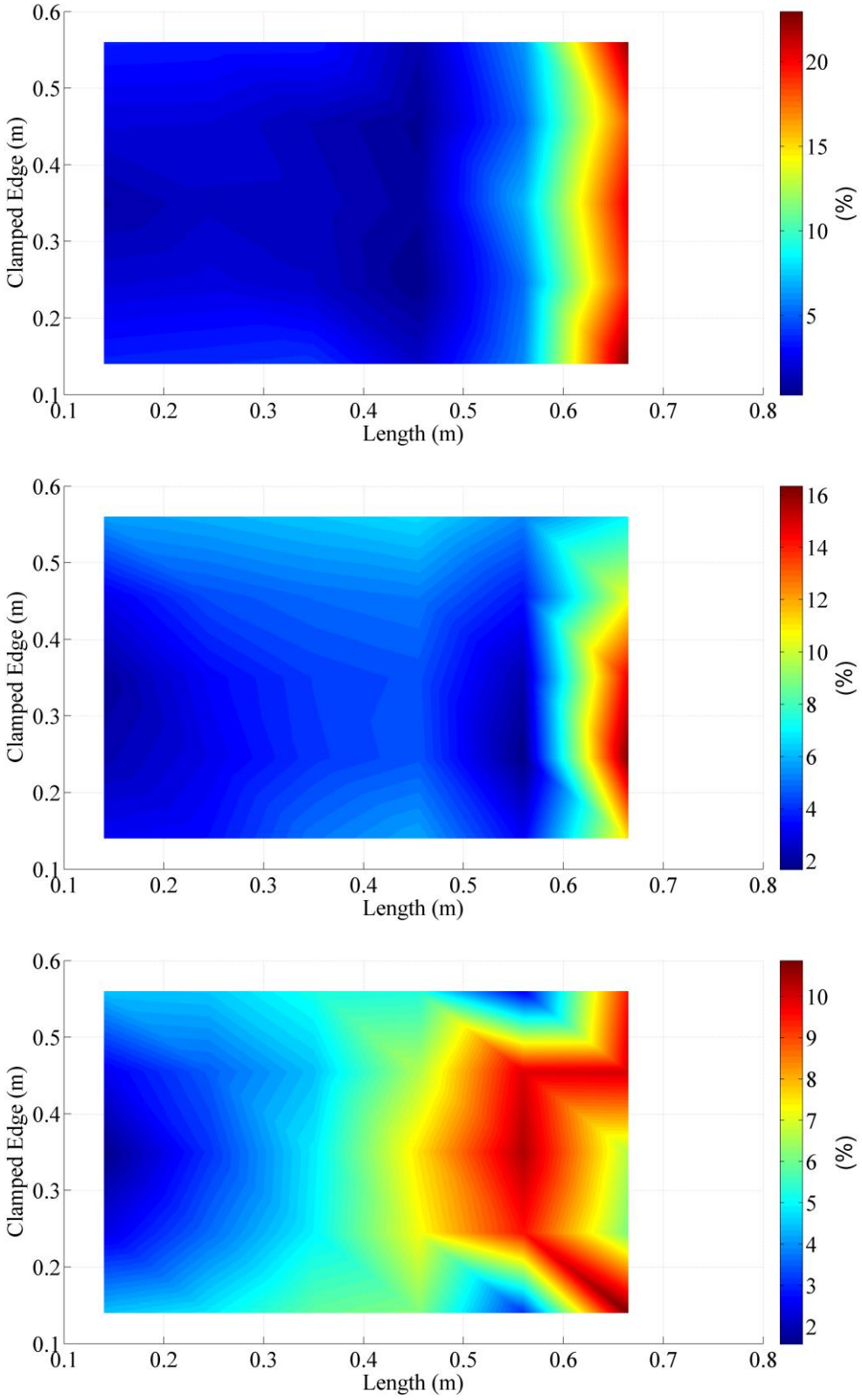

Figure 28: StrainX MAPE for all load cases: center tip, corner tip, pressure (realistic).

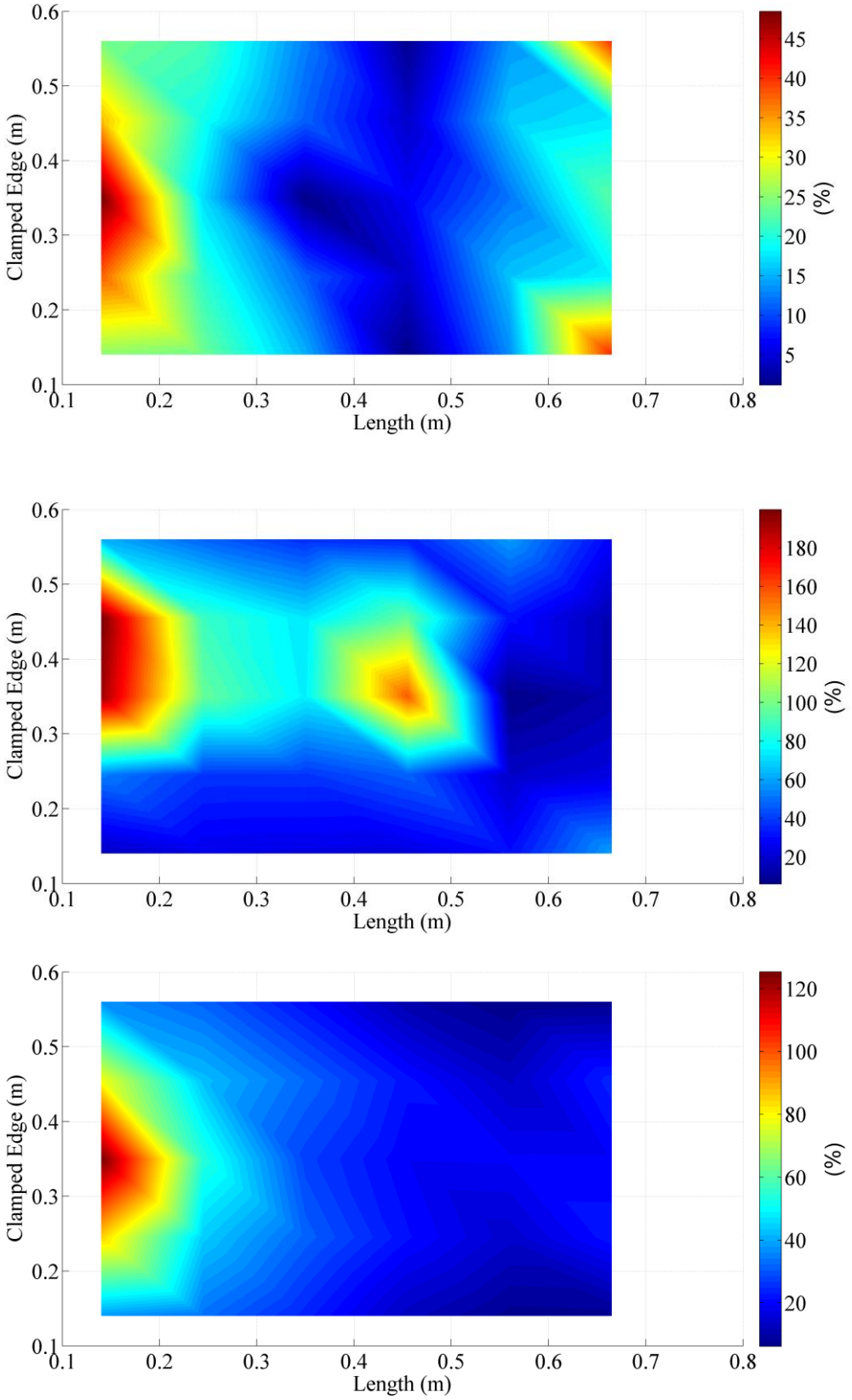

Figure 29: StrainY MAPE for all load cases: center tip, corner tip, pressure (realistic).

3.5.2.3 Mean Absolute Percentage Error (MAPE) on Entire Plate over Time Series

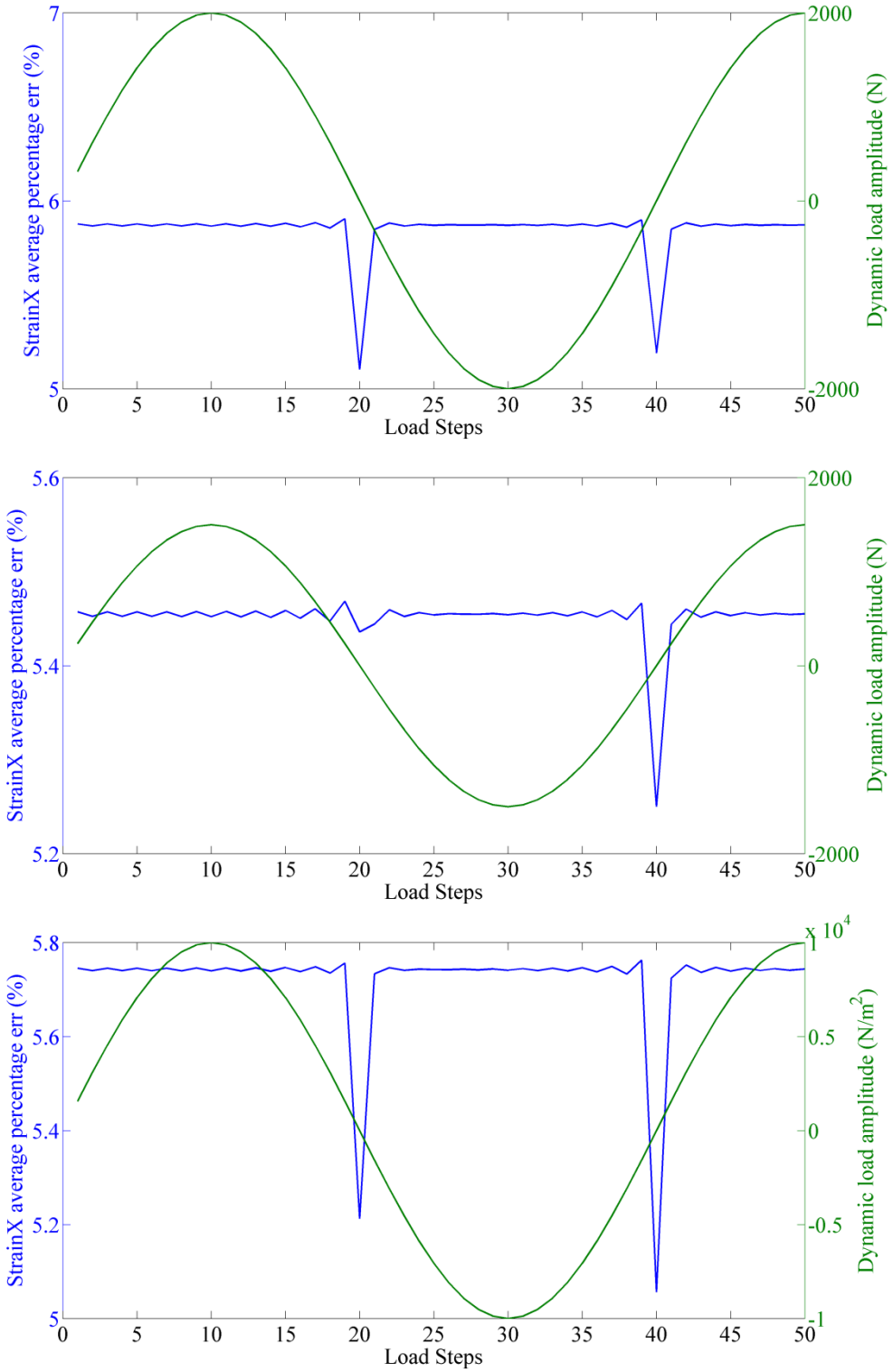

Figure 30: StrainX MAPE vs load steps comparison for: center tip, corner tip, pressure (realistic).

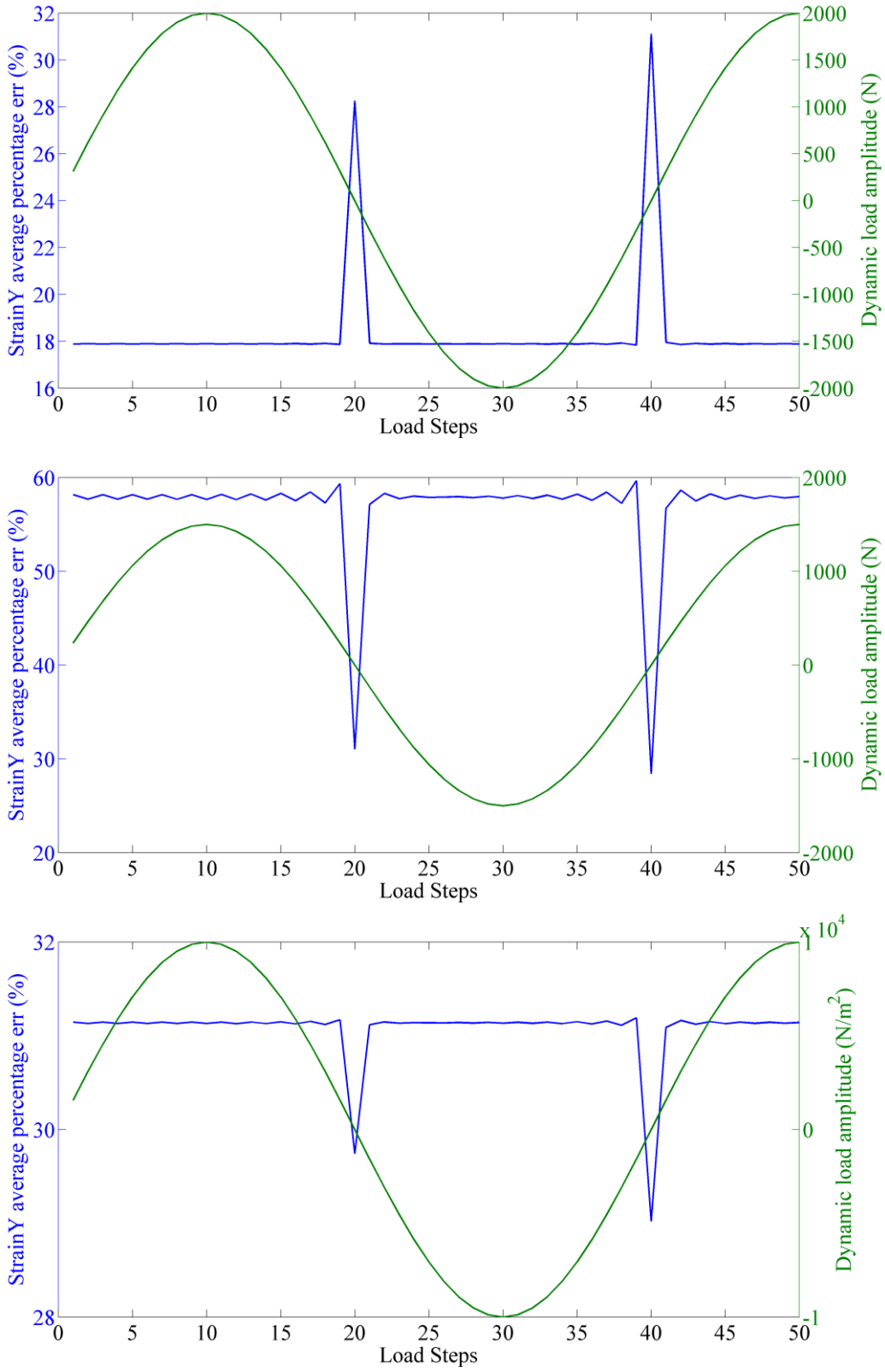

Figure 31: StrainY MAPE vs load steps comparison for: center tip, corner tip, pressure (realistic).

As discussed in the previous section regarding the spikes in the MAPE versus time series plots shown in Figures 30 and 31, the spikes might be negligible since the spikes appear when the external applied loads are almost zero. The errors for both directions appear to be stable over the load steps under all load cases. For ε_x, the errors are pretty similar to each other in three cases, and the minimum error is 5.45% from the corner load. Nevertheless, the errors varied for ε_y with a maximum of 58% and a minimum of 18%. In the case of corner load, the change of errors over load steps is not as stable as it is in the other two, especially for points near zero load point.

3.5.3 Comparison of results from idealized and realistic arrangements

It is obvious that the results from both sensor arrangement types are different than each other. Therefore, the percentage error was calculated and compared between two different sensor arrangements in Tables 3–5 shown below. The calculation procedure is demonstrated here: First, the mean absolute percentage error for all inner sensors on the plate under one load step were calculated and averaged so that one averaging percentage error can be obtained for entire plate at one load step; then the first step was repeated for all fifty load steps; and finally the mean value was taken for these fifty averaged errors so that one overall percentage error was able to be defined for the entire plate under all load steps. This procedure has been applied for each load case as well as for each sensor arrangement. Similarly, the aforementioned process was also utilized to get standard deviations for percentage errors.

Table 3: Results comparison for two sensor arrangements under center tip load.

Sensor Arrangement	Point load at center tip			
	Percentage error (%)			
	Mean*		Standard Deviation*	
	x	y	x	y
Idealized	9.13	21.54	0.29	0.81
Realistic	5.84	18.36	1.01	2.23

Table 4: Results comparison for two sensor arrangements under corner tip load.

Sensor Arrangement	Point load at one tip corner			
	Percentage error (%)			
	Mean*		Standard Deviation*	
	x	y	x	y
Idealized	2.30	16.49	1.63	1.90
Realistic	5.45	56.83	0.15	5.52

Table 5: Results comparison for two sensor arrangements under uniform pressure.

Sensor Arrangement	Pressure over full plate			
	Percentage error (%)			
	Mean*		Standard Deviation*	
	x	y	x	y
Idealized	**5.17**	**9.39**	**0.05**	**0.21**
Realistic	5.72	31.07	0.12	0.63

** denotes that values are calculated from absolute percentage errors.*

For the center tip load, we can see that the mean errors for idealized arrangement are larger than the errors for realistic arrangement. While for standard deviation of percentage error, the one from the idealized case is much smaller than the one from the realistic case, which means the errors are more dispersed in the realistic case than the idealized case. By comparing the percentage errors between two directions, it was found that the errors for ε_y are much larger than the errors for ε_x. In the case of corner load, the mean errors for idealized case are much bigger than the errors for realistic case. The same trend has been shown for standard deviation except

for percentage error for x. In general, the performance of the algorithm is better as well as more stable for the idealized case. It is noticeable that the percentage errors of ε_y are much bigger than those of ε_x, especially for the realistic case. The maximum difference is more than 10 times. Again, this change could be because of high sensitivity of the algorithm for torsional load. It is clear that all the mean and standard deviation values for the idealized case are smaller than those values for the realistic case when subjecting uniform pressure over the entire plate. The standard deviation of percentage error for the idealized case was calculated as 0.05, which means the errors are very close to their expected value.

In comparing the three tables, it is not hard to reveal that the algorithm is functioning more accurately and with stability under uniform pressure. For different arrangements of sensors on the boundaries, estimation under the idealized case shows better agreements with real values than the realistic case. For all load cases and sensor arrangements, the accuracy of estimation is shown to be more accurate for ε_x than ε_y. Furthermore, the accuracy of estimating for ε_y is more sensitive to sensor arrangement than it is for ε_x.

CHAPTER 4 THE EFFECTS OF SENSOR ARRANGEMENT ON ESTIMATING ACCURACY

4.1 Introduction

A capable SHM system should be designed to monitor the properties of the structure. The performance of an SHM system essentially relies on the quality of information that can be extracted from the sensor data. This quality depends on type, number, and the location of sensors chosen for the structure. In some cases, engineering assessment and judgment are the basis of sensor location selection [30], while lots of efforts that focus on the development of various methodologies of optimal sensor placement (OSP) have been done in past several years. Starting from simple visual inspection and observation, new science-based methods were developed including Modal Kinetic energy (MKE) methods, which uses mode shapes to find the locations with the highest amplitudes and considers that for sensor placement [31]. Heo et al. [32] derived a kinetic energy optimization technique and applied it to real experimental data obtained from a model of an asymmetric long span bridge. Another method proposed by Carne uses the minimization of the off-diagonal terms in the modal assurance criterion matrix as a measure of the effectiveness of a sensor configuration [33]. One of the most cited OSP approaches was proposed by Kammer [34]. This method computes the modal contribution for each sensor pattern and eliminates the patterns with no significant contribution. The selected configuration maximizes the trace and determinant and minimizes the condition number of the Fisher information matrix corresponding to the target modal partitions. Genetic algorithms and neural networks were also utilized to an optimal location of the sensors [35, 36]. Cobb and Liebst

proposed a method that prioritizes the degrees of freedom to find the OSP [37]. The analyses were based on an eigenvector sensitivity analysis of a finite element model of the structure. Also, static flexibility approach was proposed by Flanigan [38]. This method optimizes the static transformation matrix assuming that the best degrees of freedom (DOFs) are those in which the finite element model mode shapes can be represented as a linear combination of static flexibility shapes. A reduced number of DOFs can be obtained using Guyan reduction by minimizing fitting errors of the least squares equation. The DOFs obtained are considered to be the sensor locations.

In most cases, the sensors deployed on the structures are installed permanently, and especially for large scale structures like wind turbine blades, the sensors are mounted sparsely or much less than the locations that are available on the structures [39]. One of the reasons for this fact is the ineffective high cost for large amount of sensors and their data acquisition instruments. Also, the regular maintenances for large amount of sensors could be difficult due to the limited accessibility of the structures. In addition, for the integrity of wired sensors, interference needs to be prevented from providing special care for the routing of the sensor cables, especially for optical fiber sensors [40].

4.2 Proposed arrangements of SECs

In this study, various arrangements of SECs were generated and utilized to perform strain decomposition tasks using proposed strain fitting algorithm. The decomposing strain results from uniform sensor placement were used as a basis to compare with results obtained from the other sensor arrangements. The idealized sensor placement on boundaries were used as a base pattern since it is able to obtain more accurate BCs if considering the possibility of deploying traditional

resistive strain gauges on the boundaries to extract the BCs. At the same time, the influence of boundary qualities on estimating accuracy can be excluded, and so univariate analysis can be achieved. Moreover, idealized boundary placement of SECs saves more inner spaces for a variety of SECs arrangement approaches. The uniform pressure load case was applied in that the performance of the algorithm is relatively more stable compared to the other two.

Instead of using the OSP technologies reviewed and mentioned previously, the SECs were arranged more on an information basis, which involves visual inspection and observation. The rationale is that extracted information from sensors will be different due to various sensor arrangements, and then the effect of arrangements of SECs on the estimating accuracy can be investigated.

4.2.1 Sensor amount remains the same as the uniform arrangement

First, different placement methods were examined in the case that the total number of the sensors (fifty six) maintains the same. As shown in the Figures 32 and 33, 26 SECs were placed on the boundaries in the same way as idealized uniform arrangement. 30 inner SECs were either concentrated on fixed-free ends (Figure 32) or stagger-distributed (Figure 33). The rationale for arrangement #1 is that the more the sensors were concentrated on fixed and free end, the more strain information should be extracted since the strains reach maximum at the fixed end for ε_x and at the free end for ε_y.

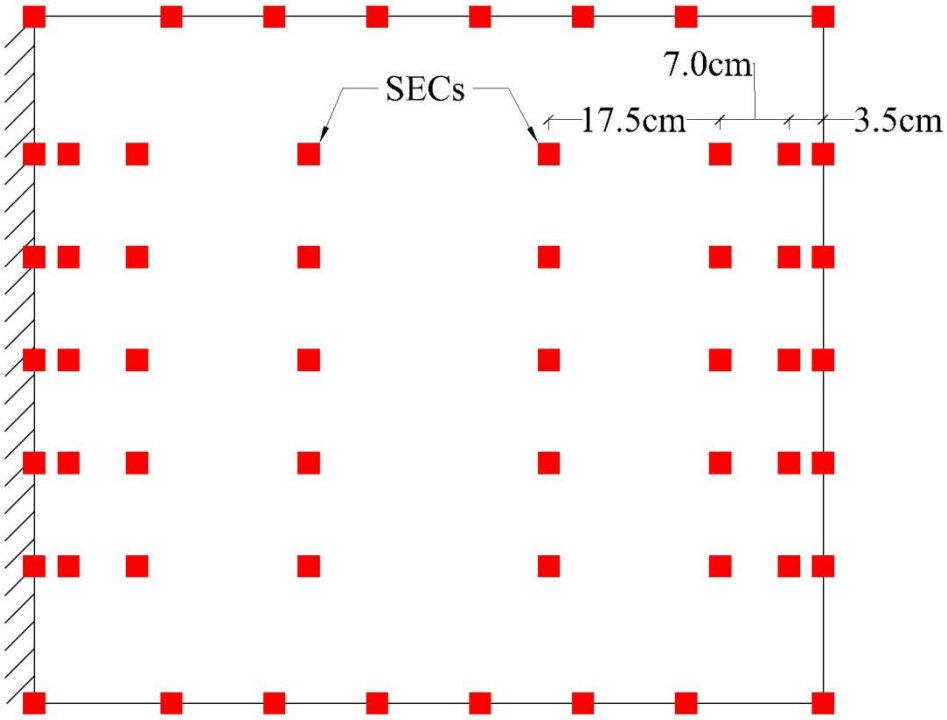

Figure 32: SEC arrangement #1: 56 SECs, fixed-free enhanced.

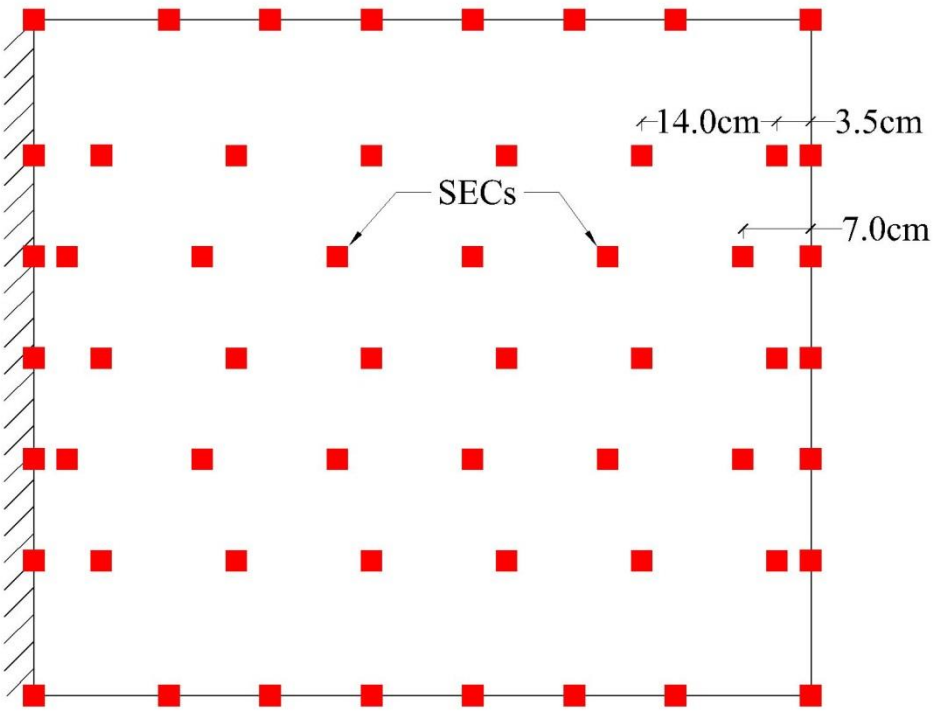

Figure 33: SEC arrangement #2: 56 SECs, inner staggered.

The strain signals from these SECs were constructed from FEA and were used to decompose the strains using proposed algorithm. The results were compared against uniform sensor placement and were presented in Figures 34–39.

The strain fitting 3D plots in Figures 34 and 35 shows that the two surfaces that represent real strain and estimated strain are close to each other for all three cases. The overlapped areas, however, between two surfaces were varying from each case. For ε_x, the algorithm tends to overestimate the strains around fixed and free tip ends when comparing to the results from uniform sensor placement; in the meantime, the ε_y were underestimated around fixed corners and the center area of the free tip. No certain pattern, however, can be found about how the estimation errors change near the fixed corners.

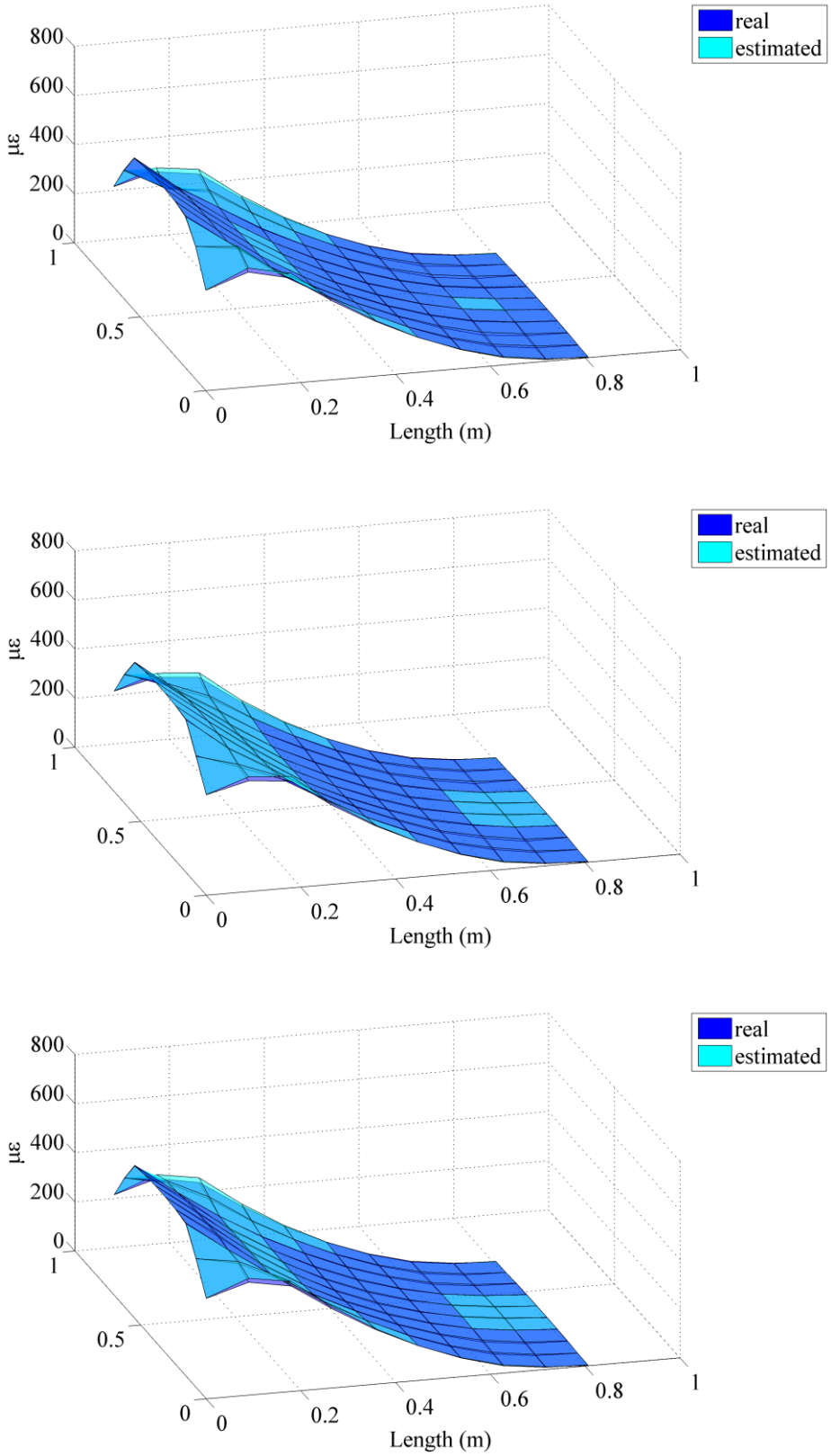

Figure 34: StrainX strain fitting for uniform pressure: uniform, arrangement #1, #2.

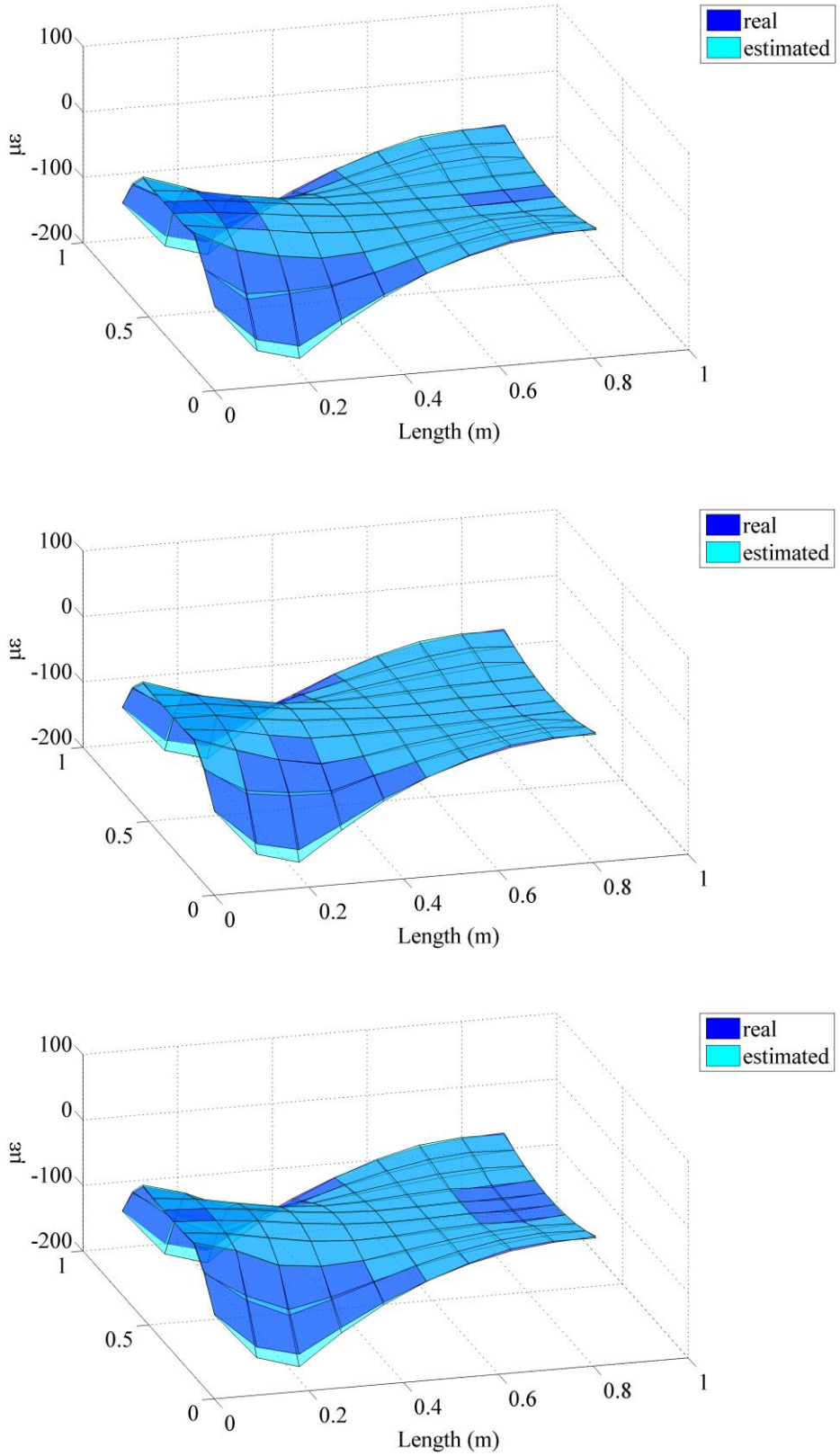

Figure 35: StrainY strain fitting for uniform pressure: uniform, arrangement #1, #2.

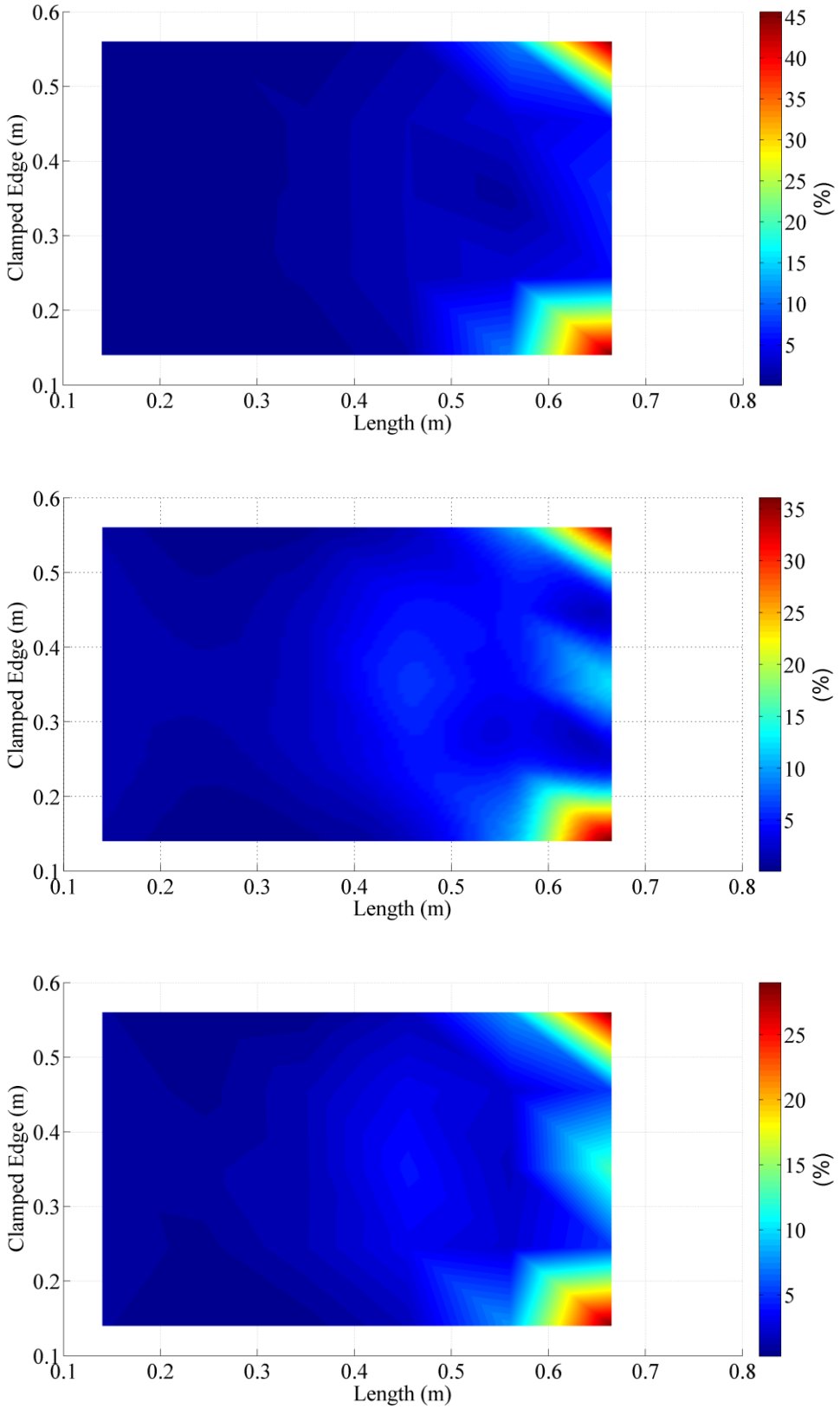

Figure 36: StrainX MAPE comparison for uniform pressure: uniform, arrangement #1, #2.

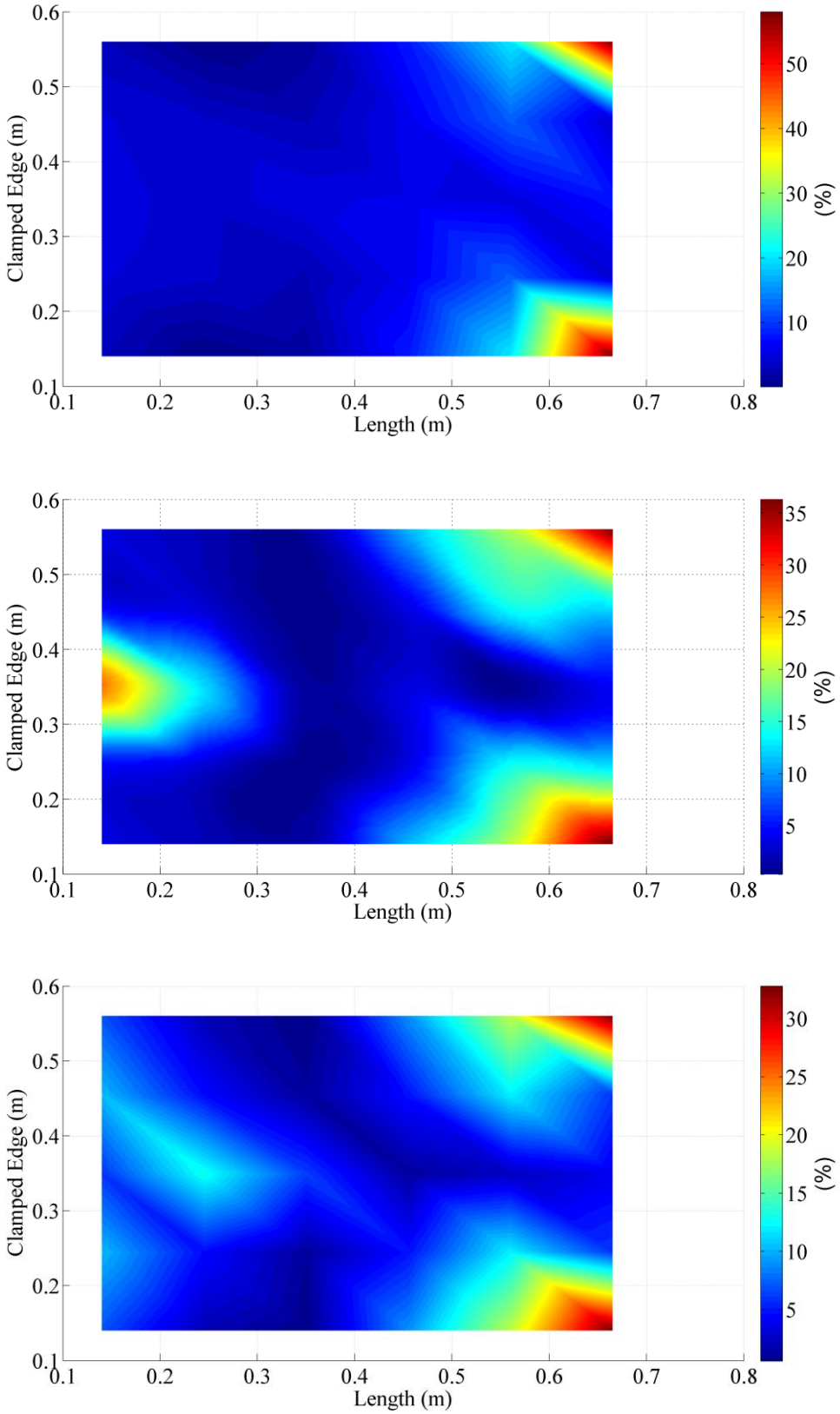

Figure 37: StrainY MAPE comparison for uniform pressure: uniform, arrangement #1, #2.

By looking at the maximum percentage errors showing in Figure 36, one may note that the maximum percentage error of arrangement #2 has the smallest value of 30% while the results from the uniform arrangement seem to have the largest percentage error around 45%. For all three cases, the maximum errors concentrated around two free corners, which can be explained by boundary condition absence of these two locations. The same trend can be found in MAPE map for ε_y. Arrangement #2 has the lowest maximum error of 33%, and the uniform arrangement has the largest maximum error of 57%. Besides the two free corners, percentage errors have tended to increase near the fixed end in both arrangements #1 and #2. Further study is needed to explain the phenomenon. The author thinks that the increase may be because of more sensors near the fixed end. The ε_y is minimal at the fixed, however, so that the system is not receiving the accurate boundary conditions.

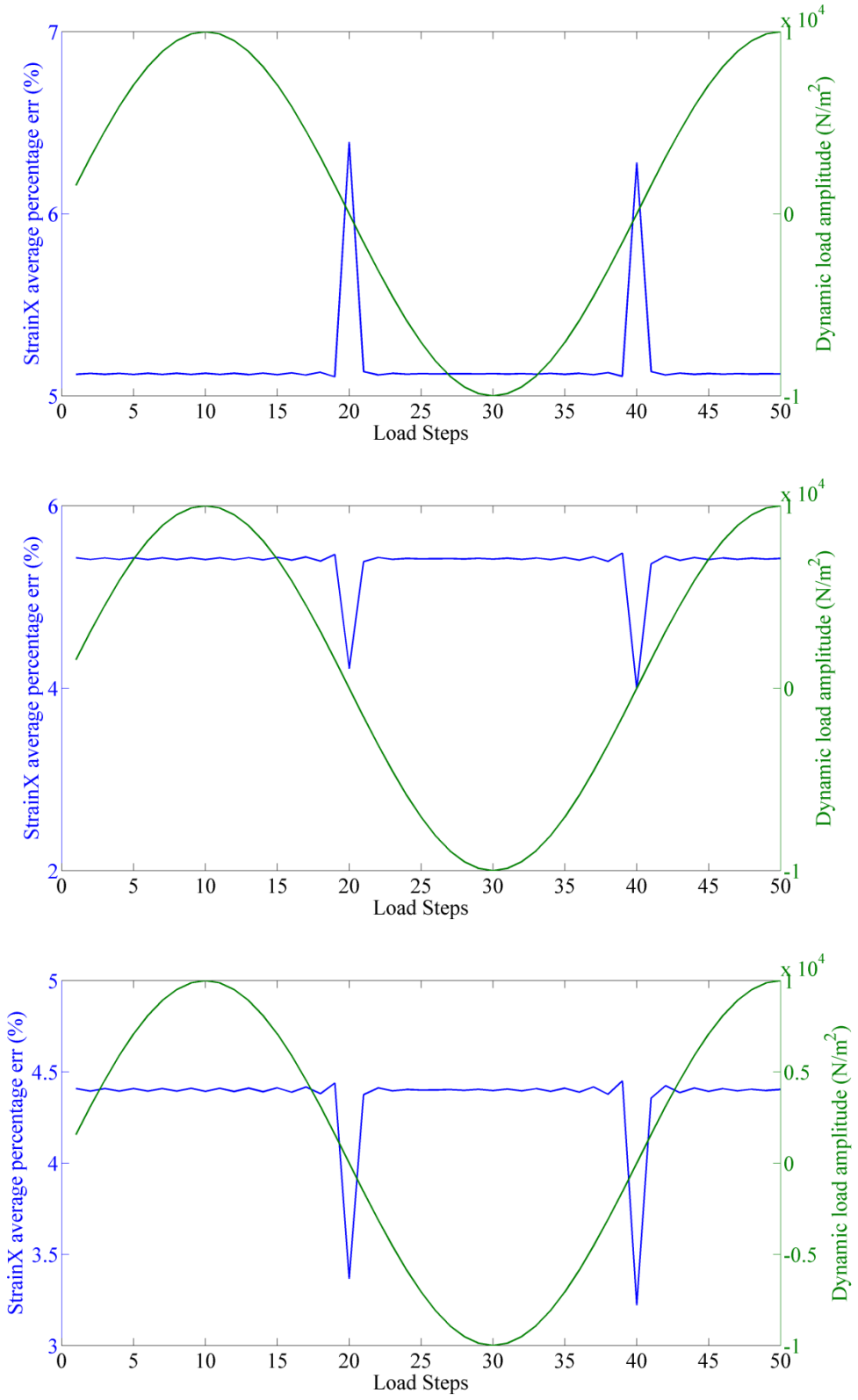

Figure 38: StrainX MAPE vs load steps comparison under uniform pressure for: uniform, arrangement #1, #2.

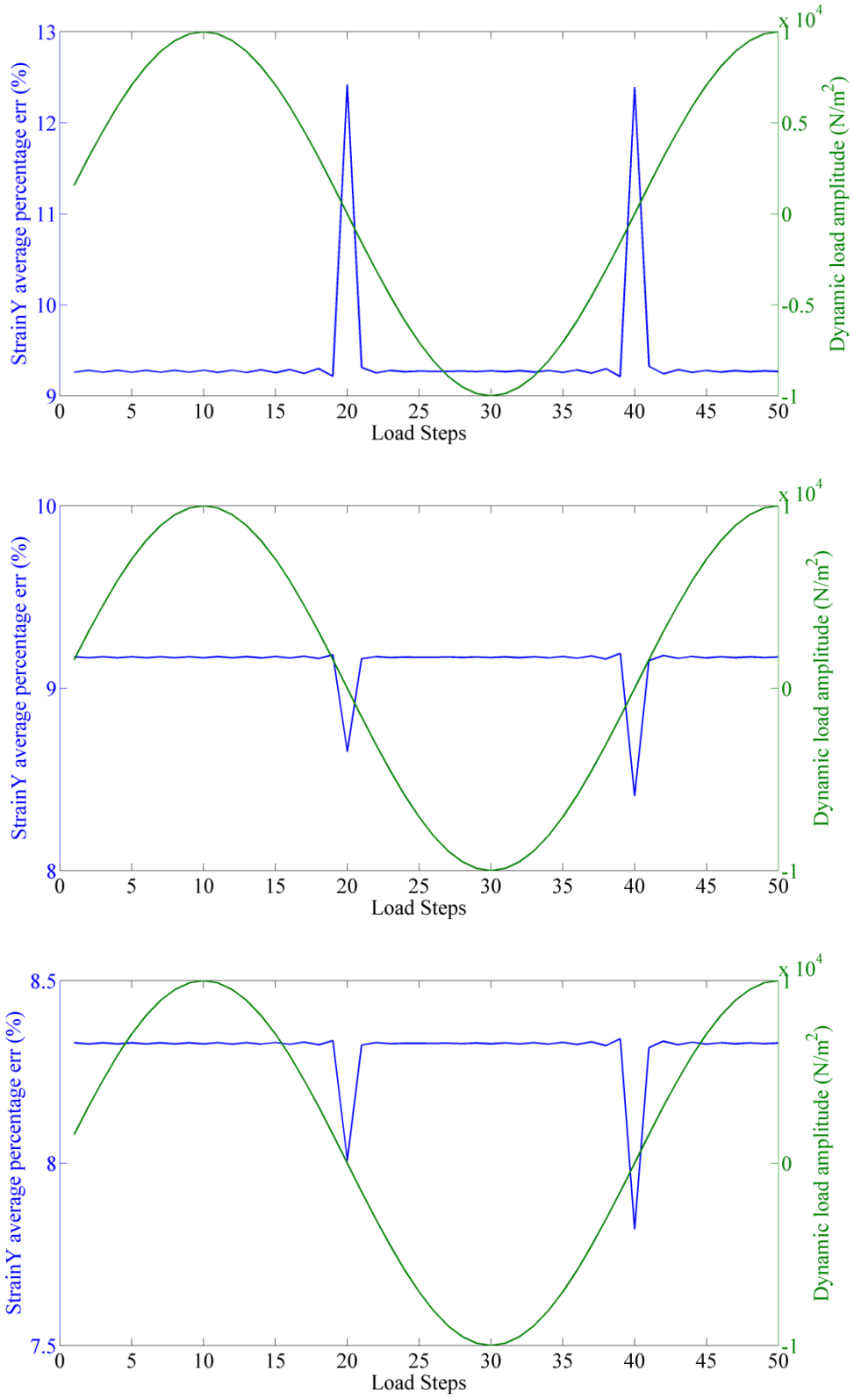

Figure 39: StrainY MAPE vs load steps comparison under uniform pressure for: uniform, arrangement #1, #2.

The performance of the algorithm can be seen more clearly in Figures 38 and 39 with load steps displayed. In Figure 38, the error from arrangement #2 has the lowest value around 4.4%. In contrast, arrangement #1 did not improve the estimating accuracy but increased the error instead when compared to the results shown for the uniform arrangement. The same trend is showing in Figure 39 for ε_y, but it is hard to tell the difference between uniform arrangement and arrangement #1. The resutls comparision will be provided in Section 4.3.

4.2.2 Various sensor amount

Secondly, as shown in Figures 40 and 41 in the next page, thirty inner sensors remained the same arrangement as idealized uniform placement, but the number of sensors on the boundaries has been diminished, which resulted in a reduced total number of the SECs. The rationale is that to test if the algorithm is able to accomplish the task with reduced information extracted from the system, better cost-effectiveness of the system can be achieved.

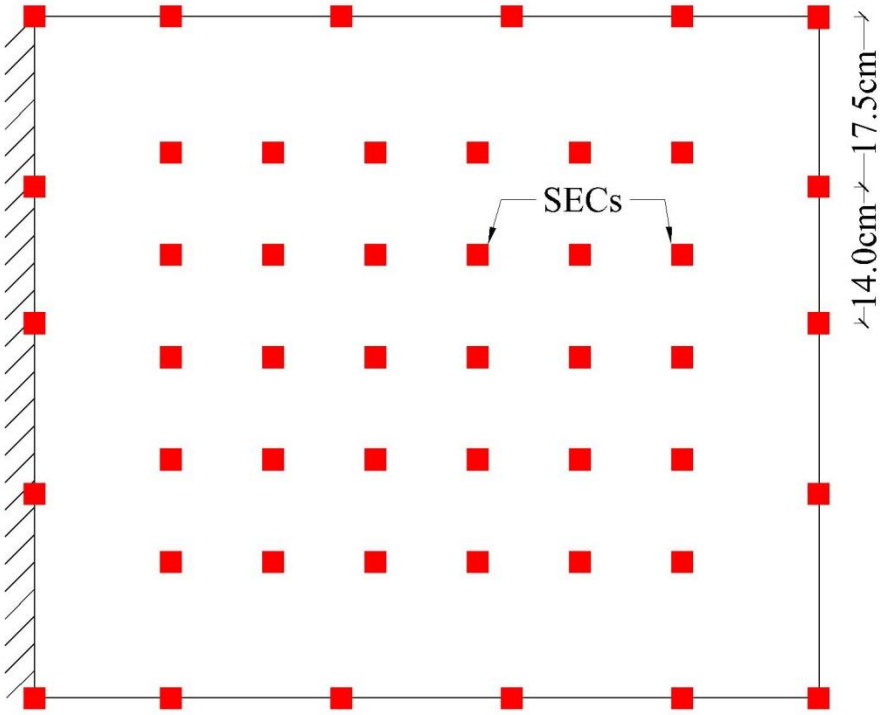

Figure 40: SEC arrangement #3: 48 SECs, boundary diminished.

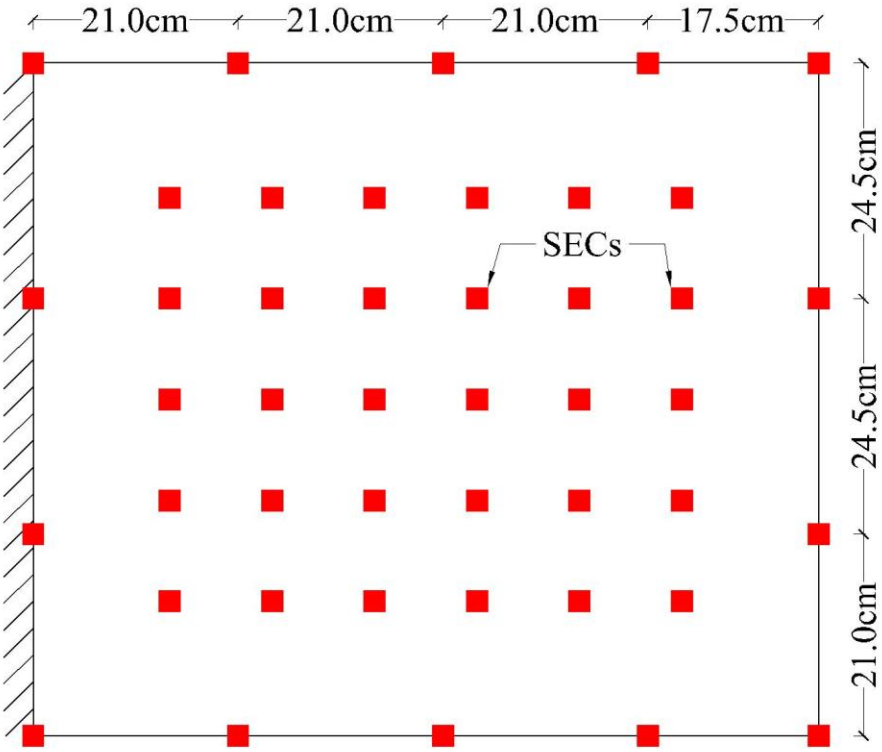

Figure 41: SEC arrangement #4: 44 SECs, boundary diminished.

The same decomposing process has been applied to both cases, and the estimating results were shown as follows. Also, the results were compared against the uniform arrangement. First, the 3D surface strain maps for two directions are presented in Figures 42 and 43. It is obvious that the algorithm tended to overestimate ε_x but to underestimate ε_y in arrangement #3. In arrangement #4 near the center areas, theε_x was underestimated and the ε_y was overestimated. The surfaces from arrangement #4 showed some differences than the other two cases. The MAPE contour plots were presented right after 3D surface plots to investigate the difference.

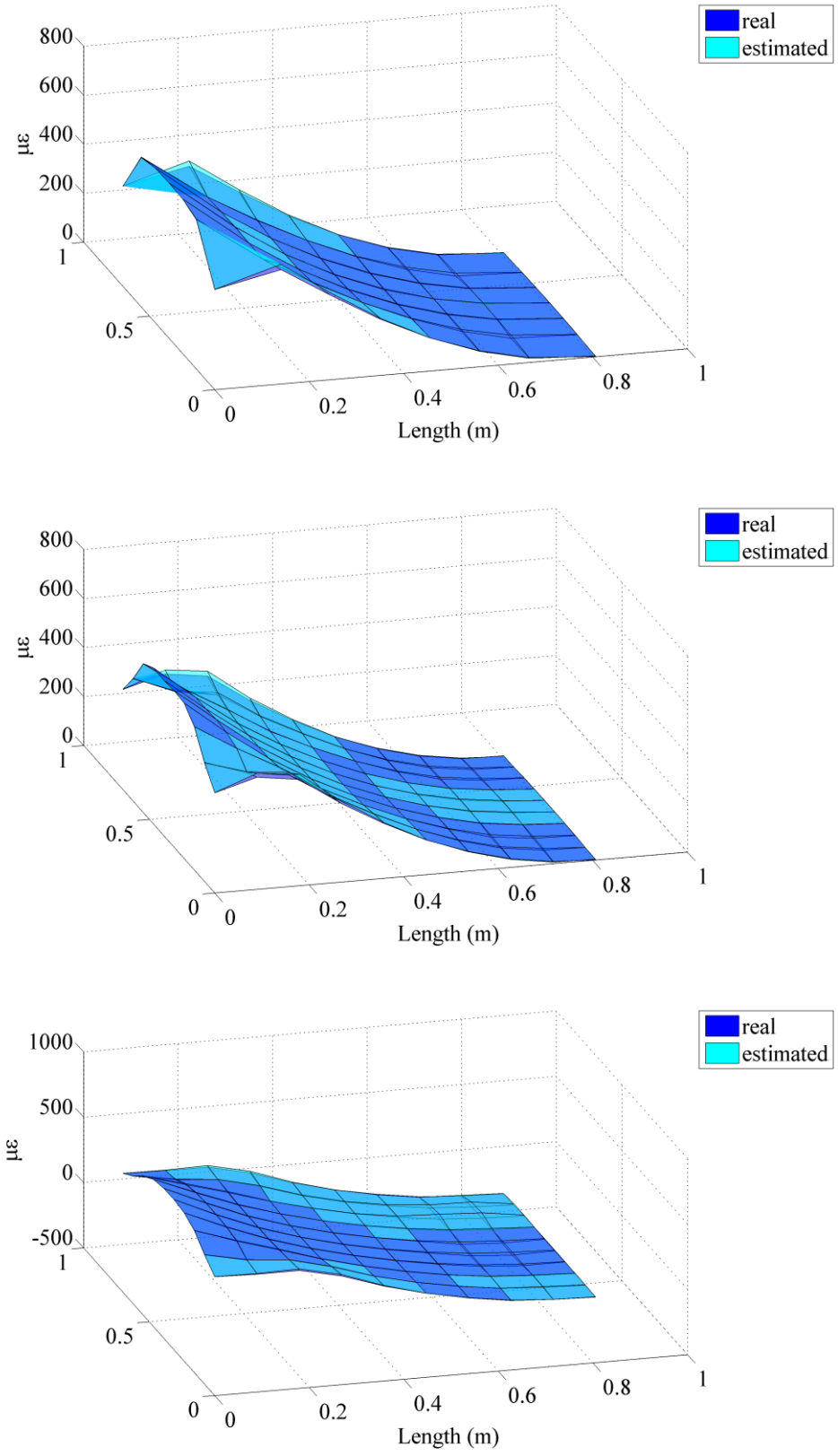

Figure 42: StrainX strain fitting for uniform pressure: uniform, arrangement #3, #4

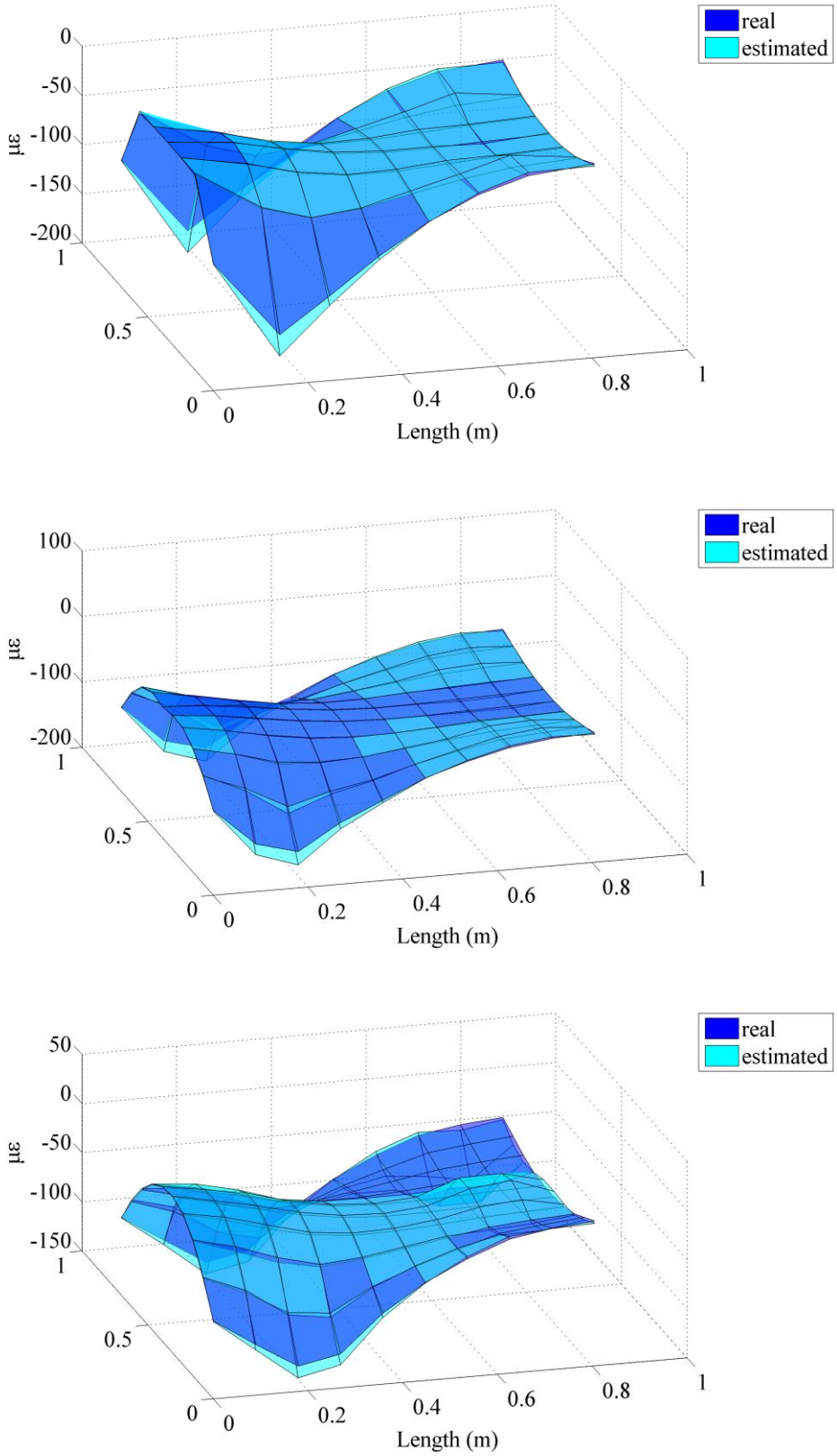

Figure 43: StrainY strain fitting for uniform pressure: uniform, arrangement #3, #4

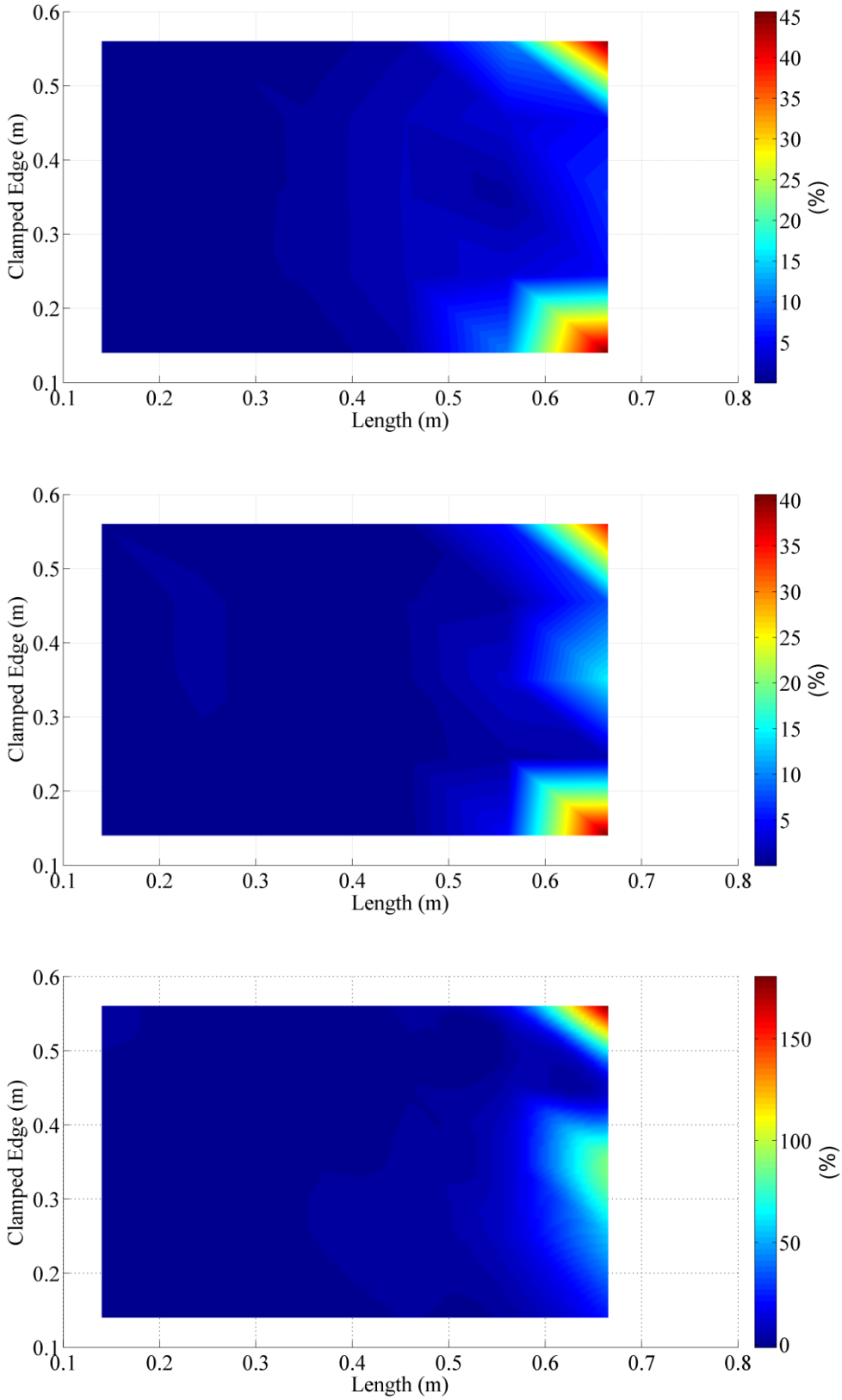

Figure 44: StrainX MAPE comparison for uniform pressure: uniform, arrangement #3, #4.

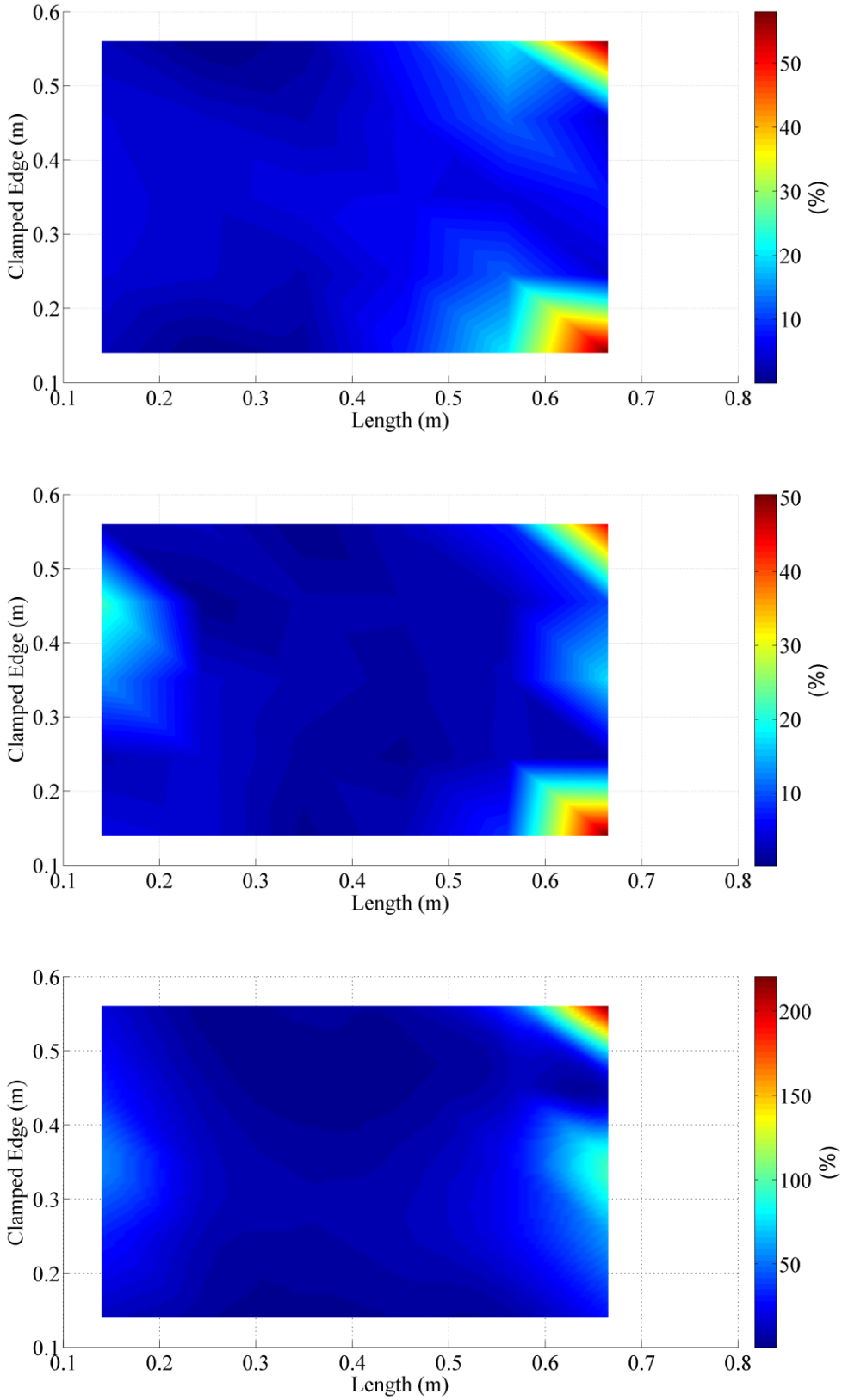

Figure 45: StrainY MAPE comparison for uniform pressure: uniform, arrangement #3, #4.

As shown in Figures 44 and 45, arrangement #3 has the lowest maximum percentage error among three cases for both directions. In contrast, the maximum estimating errors became extremely large for ε_x and ε_y in arrangement #4. In addition, the overall errors showing in the blue areas in case #4 fell in the range of 0-50%, which is much larger compared to the other two. Moreover, the maximum error focused only on the upper tip corner in case #4.

In order to compare the overall performance of the algorithm, the errors were plotted versus the load steps in Figures 46 and 47. According to the blue lines, the case #4 has reduced the percentage error for both ε_x and ε_y by comparing to the uniform case. Again, the estimating accuracy of the algorithm is independent of the load amplitude except for load steps that have zero magnitude.

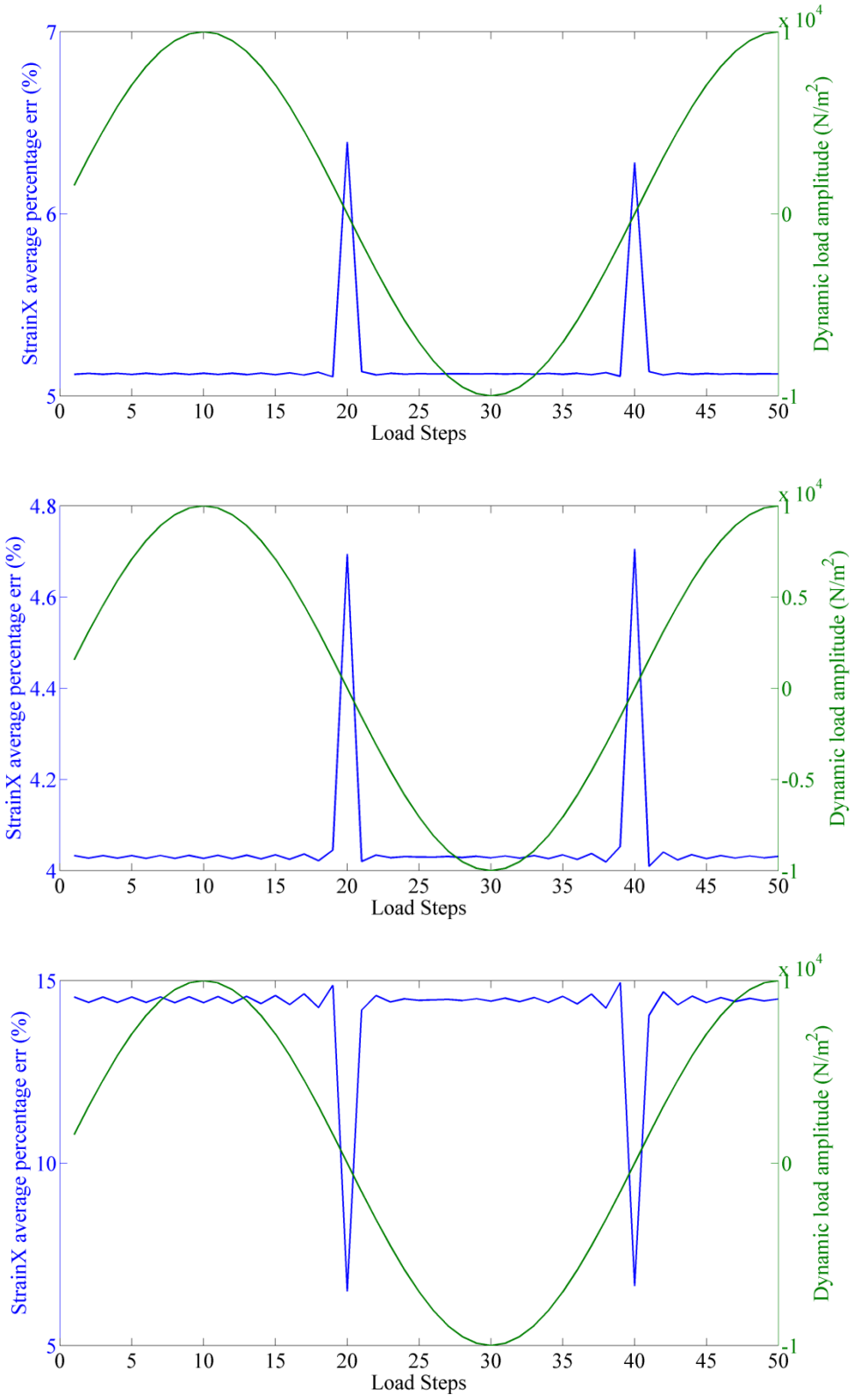

Figure 46: StrainX MAPE vs load steps comparison under uniform pressure for: uniform, arrangement #3, #4.

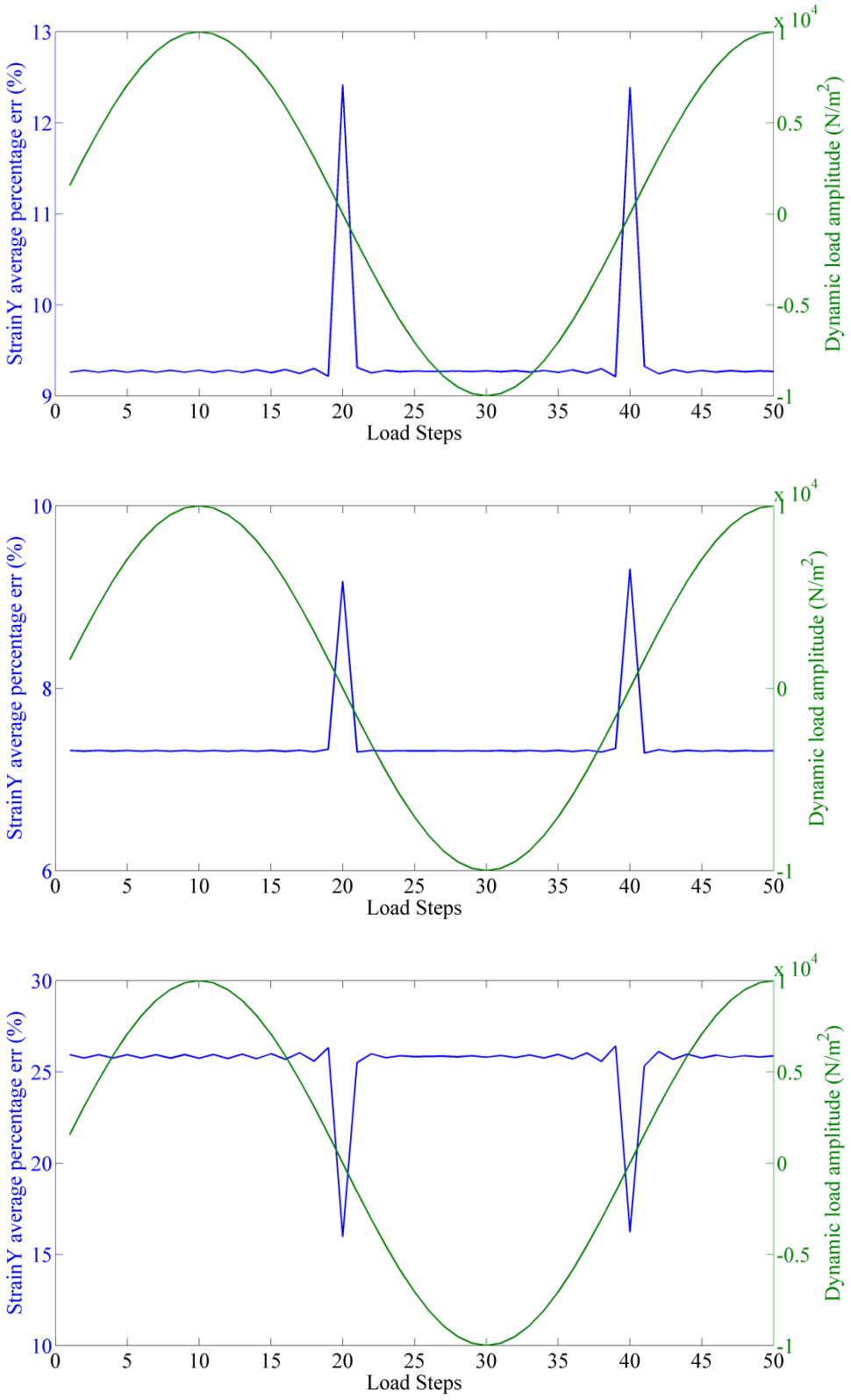

Figure 47: StrainY MAPE vs load steps comparison under uniform pressure for: uniform, arrangement #3, #4.

4.3 Results Comparison for Uniform and Proposed Arrangements

In this section, the results were summarized by averaging percentage error for all 50 load steps. Thus, the values from each case could be compared in Table 6 as follows:

Table 6: MAPE Comparison for different sensor arrangements.

Sensor Arrangement	Pressure over full plate				
	Percentage error (%)				Determinant of ($\boldsymbol{C'C}$)**
	Mean*		Standard Deviation*		
	x	y	x	y	
Uniform Arrangement	5.17	9.39	0.05	0.21	1.0621E-223
Fixed-free Enhanced #1	5.37	9.14	0.21	0.24	5.2171E-224
Inner Staggered #2	4.36	8.31	0.13	0.1	1.3491E-221
Boundary Diminished #3	4.06	7.39	0.04	0.25	8.7096E-234
Boundary Diminished #4	14.16	25.46	4.81	5.13	4.8642E-244

** denotes that values are calculated from absolute percentage errors.*
*** Matrix $\boldsymbol{C}$ is the sensor placement matrix.*

By comparing the mean value of percentage errors for both ε_x and ε_y, it is obvious that arrangement #2 and #3 are helpful for improving the estimating accuracy of the algorithm. The MAPEs for ε_x and ε_y from boundary diminished arrangement #3 are the lowest in comparison to other cases. For inner staggered arrangement #2, the mean error has been decreased by 15.7% for ε_x, and by 11.5% for ε_y when compared against the uniform arrangement. By looking at the standard deviation of MAPE, the errors of inner staggered arrangement #2 for ε_x appear to be more discrete from the mean value; while for ε_y, it has the smallest standard deviation with 0.1.

In order to investigate the effect of the sensor placement on estimating accuracy, the determinant of sensor placement matrix $\boldsymbol{C'C}$ has been calculated for each arrangement. It needs to be clarified that the determinant of $\boldsymbol{C'C}$ was taken before B.Cs had been enforced. Thus $\boldsymbol{C}$ was not invertible since the determinant was almost zero for each case, as showing in Table 6. In the

comparison of first three cases, which have same sensor amount, it is found that the larger the determinant is, the more accurate the algorithm estimated. According to the theory, square matrix is not invertible if and only if the determinant is zero, which provides the support to the statement that the further the determinant to zero, the more accurate inversion result can be obtained. The error of case #3, however, has been recognized as the smallest while it has the second largest determinant. This feature is probably because the sensor amount of case #3 is different than the uniform arrangement. Therefore, their determinants are not comparable. At last, the inversion of $\boldsymbol{C}$ in case #4 was not unique due to rank deficiency. As a result, the estimating accuracy was much lower than other cases.

CHAPTER 5 VERIFICATION OF THE ALGORITHM USING PROPOSED SENSOR ARRANGEMENTS ON BLADE-SHAPED PLATE

5.1 Introduction

In CHAPTER 3 and 4, the proposed strain-fitting algorithm was shown to be validated for performing the strain decomposition task on an aluminum thin plate under different sensor arrangements. The decomposed results have shown good agreements with the real bidirectional strain data extracted from ANSYS. In addition, inner staggered and boundary diminished sensor placements were identified as two cases which can improve the estimating accuracy.

In this chapter, the algorithm and the effect of two arrangements will be verified on a tapered plate. The tapered plate was designed based on CX-100 wind turbine blade that was manufactured by TPI Composites in July 2004. The overall baseline geometry of CX-100 blade was developed and designed based on ERS-100 blade [41] but with adjustments of the root transition area and the tips of the blade. The CX-100 is a 9-meter wind turbine blade comprised of fiber glass composite materials. In accordance with the corresponding project report provided by Sandia National Laboratories, the detailed design specifications of the CX-100 blade were obtained, and then have then been used to outline and create a tapered plate with the same external geometry of the blade model using multiple key points extracted. The detailed design and development of the plate will be discussed later. It is intended that the plate was designed to simulate the behavior of the wind turbine blade to some extent as well as to verify the feasibility of the application of the proposed strain-fitting algorithm. In order to provide practical and realistic results, the real wind speed data were acquired from the National Oceanic and

Atmospheric Administration's (NOAA) database to imitate the realistic loading environment of wind turbine blade. Once all the information were imported and built in ANSYS, the model was analyzed using similar dynamic configurations as used in CHAPTER 3 for the rectangular thin plate. Subsequently, the results of decomposed strain data using the proposed algorithm were presented and compared with the real strain data obtained from ANSYS. Mean average percentage error contour plots were provided and the estimating accuracy was discussed afterwards.

The study on this blade-shaped plate is important and helpful for understanding the behavior of the blade and for acquiring first-hand experience on application of the proposed strain decomposition algorithm on a real wind turbine blades in the future.

5.2 Blade-shaped Plate Development and Modeling in ANSYS

5.2.1 Plate geometry

The conventional carbon-spar CX-100 is a type of wind turbine blade which is created from the baseline external geometry of ERS-100 blade with several modifications at the root and tip sections. According to design specifications provided by Sandia National Laboratories [42], the CX-100 blade has a length of 9 meters and incorporates with S-series airfoils provided by National Renewable Energy Laboratory (NREL). Three types of airfoils, S821, S819 and S820, have been used for the in-board region (21% to 40%), 70% and 95% radius, respectively. The cross-section dimensions of the blade, including chord length and twist angles, are listed in Table 7. The assignment of airfoils for the three regions are given in the table as well. It is worth mentioning that the root section (up to station 400) has been simplified with a circle cross section with a radius of 0.3m.

Table 7: Modified CX-100 baseline platform dimensions.

Station (mm)	Chord Length (m)	Twist(deg.)	Airfoils
0	0.300	0	Circle
400	0.300	0	
1000	0.569	20.8	S821
1400	0.860	17.5	
1800	1.033	14.7	
2200	0.969	12.4	
3200	0.833	8.3	
4200	0.705	5.8	
5200	0.582	4	
6200	0.463	2.7	S819
7200	0.346	1.4	
8200	0.232	0.4	S820
9000	0.120	0	

Based on the cross-section dimensions shown above, six key points have been selected and used to generate the blade-shaped plate geometry: two key points, which are able to represent the width of the blade cross sections, were selected at each station 0mm (root), 1800mm (the widest) and 900mm (tip). The completed geometry is given in Figure 48. The plate has a length of 9m, a root width of 0.3m, a tip width of 0.12m and the widest width of 1.033m, which are the same values as chord lengths in Table 7. The thickness of the plate was determined as 0.035m which was based on the blade lamina thicknesses provided by the blade manufacturer. See the next section for details.

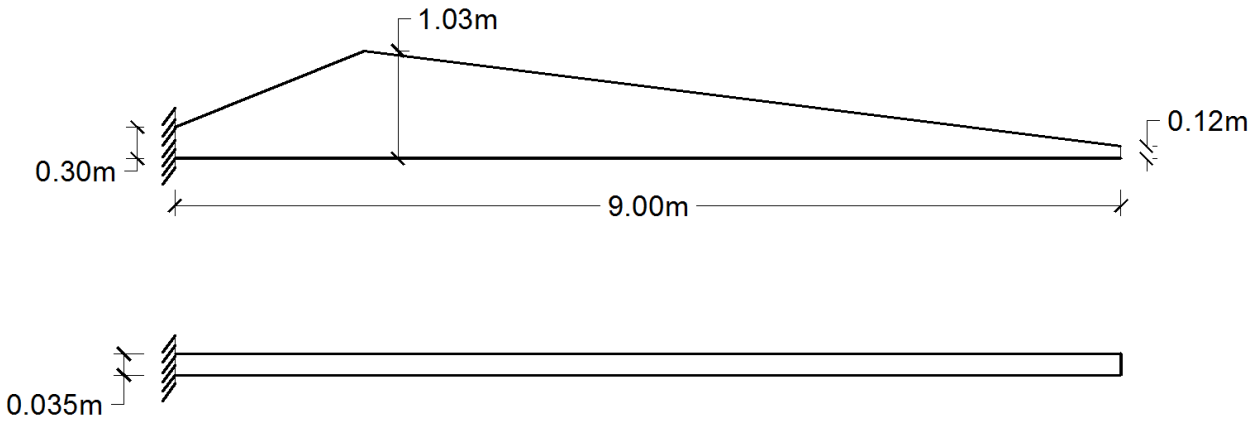

Figure 48: Blade-shaped plate geometry and dimensions.

5.2.2 Plate materials

The conventional fiberglass materials were used for blade-shaped plate, with consistent mechanical properties assumed for CX-100 blade materials. As stated in [42], micromechanics

calculations have been used to yield the stiffness of the unidirectional carbon-fiber material. The laminated material properties were obtained from [42], and are listed in Table 8.

Table 8: Lamina material properties for blade-shaped plate [42].

Material #	Layer #	Material Name	E_x (GPa)	E_y (Gpa)	G_{xy} (Gpa)	ν_{xy}	Density (kg/m^3)	Ply thickness (mm)
1	11	Gel coat	3.44	3.44	1.38	0.30	1230	0.26
3	10	Random mat	7.58	7.58	4.00	0.30	1687	0.76
5	9	end-grain balsa	0.12	0.12	0.02	0.30	230	12.80
6	7,8	DBM1708(±45 ° fiberglass)	9.58	9.58	6.89	0.39	1814	0.89
7	5,6	DBM1208(±45 ° fiberglass)	9.58	9.58	6.89	0.39	1814	0.56
8	4	C520 (0 ° fiberglass)	37.30	7.60	6.89	0.31	1874	9.20
10	3, 2, 1	Carbon-fiberglass triaxial fabric	84.10	8.76	4.38	0.25	3469	2.8, 3.2, 2.8

The material properties shown above are used to input into ANSYS material model database. By summarizing the thickness of each layer, one can get the total thickness of 34.72mm for the plate. The material number and layer number shown in the table were used only for alignment between material properties and layer thickness when configuring the section properties for SHELL181 in ANSYS. It is important that orthotropic material should be specified to the model instead of isotropic material, which was used for rectangular aluminum plate discussed in CHAPTER 3. Consequently, elastic moduli, shear moduli, and Poisson's ratios in three directions were required to be calculated. The information provided in above table, however, is not enough to determine shear moduli for the other two directions since the mechanical properties of orthotropic materials are largely dependent on how the fiber is oriented. Therefore, the material properties have been simplified by assuming transverse isotropic characteristic, which means the material properties are almost the same in any other directions

than the direction of perpendicular to the fiber's orientation. In addition, Poisson's ratio was assumed to be the same for each direction as well. As a result, directions y and z were equivalent, and the isotropic condition can be achieved.

$$E_y = E_z \qquad (Eq.26)$$

$$G_{xy} = G_{xz} \qquad (Eq.27)$$

$$G_{yz} = \frac{E_y}{2(1+\upsilon_{yz})} \qquad (Eq.28)$$

The material model was created for the plate as long as all the mechanical properties were obtained. Moreover, it is noticeable that for DBM1708 and DBM1208 fiber glasses, two section layers were generated with ±45° of fiber's orientation. It is the same orientation for carbon-fiberglass triaxial fabric: ±45 ° and 0 ° were used to establish three layers. A layout of all section layers generated by various materials is clearly shown in Figure 49.

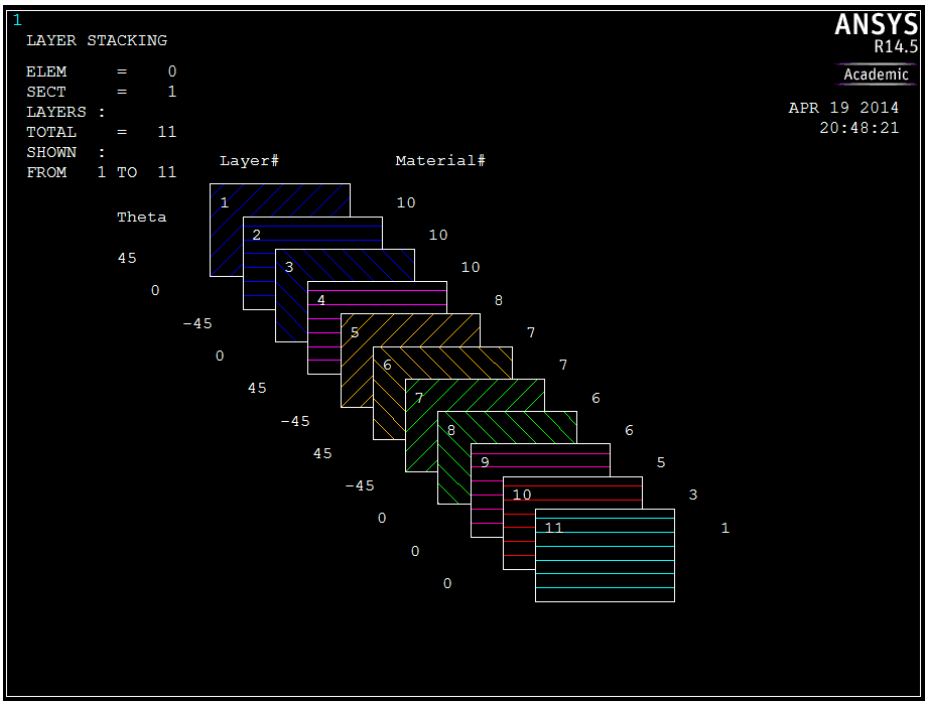

Figure 49: Lamina layout for blade-shaped plate.

5.2.3 Plate modeling and dynamic analysis configuration

The geometry and material information provided in the previous two sections were inputted into ANSYS platform. Mesh size was manually controlled as 0.1m by considering both analyzing accuracy and computational resources. The mesh attributes were configured using Cartesian coordinates system and material 1 (Gel Coat) since it is for the top layer. Moreover, the mapped mesh was employed instead of free mesh so that it is convenient to assign sensor locations according to mapped nodes. Once the settings were completed, the mesh was created automatically. The finite element model of the plate model is shown in Figure 50.

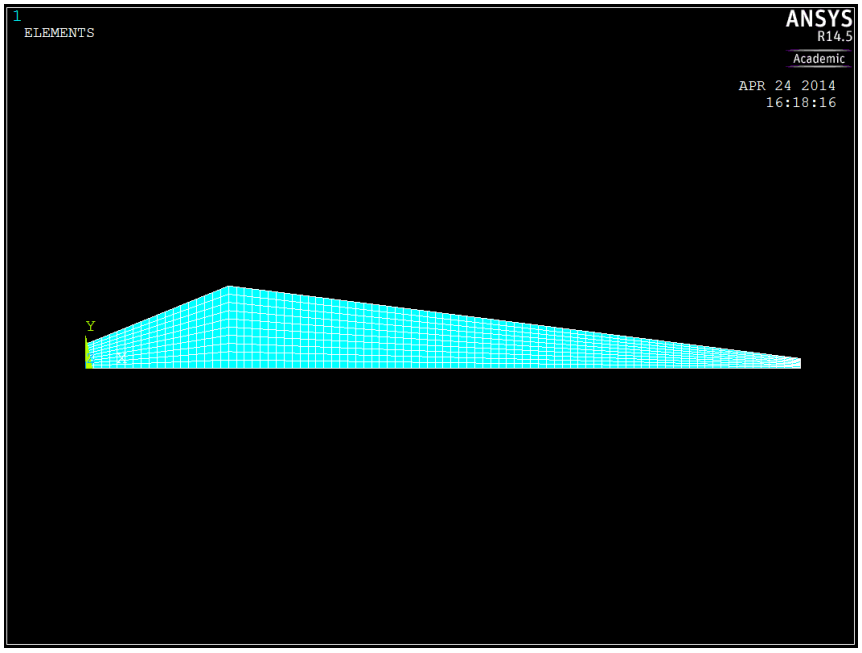

Figure 50: Finite element model of the plate with 0.1m mapped mesh.

The solutions control configuration in ANSYS APDL for transient analysis used in this chapter is similar to the one used in CHAPTER 3 but with transient options of stepped loading instead of ramped loading. The duration for dynamic analysis was 10 seconds with a 0.2 seconds time increment, which resulted in 50 load substeps in total. Nodal and element solutions for

strain, stress and displacement were written into results files for every load substep. Furthermore, when extracting the results from ANSYS, nodal strains were taken from the top layer of the plate on global coordinate basis.

5.3 Performance of Strain Fitting Algorithm on the Blade-shaped Plate

5.3.1 Wind turbulence simulation

The hybrid wind turbulence data that obtained from National Oceanic and Atmospheric Administration were used to simulate the realistic loading conditions of the wind turbine blades near off shore. The station FTPC1 (San Francisco, CA) was selected to extract the wind speed data that were sampled every 6 minutes. The simulation process mainly includes two parts: (1) identifying the physical appearance of the real wind speed by smoothing the wind speed time history data; and (2) producing turbulence spectrum to correlate with smoothed wind speed time history. As a result, the hybrid wind speed can be simulated as shown in Figure 51. Accordingly, the wind pressure can be generated based upon the wind speed, (Figure 52).

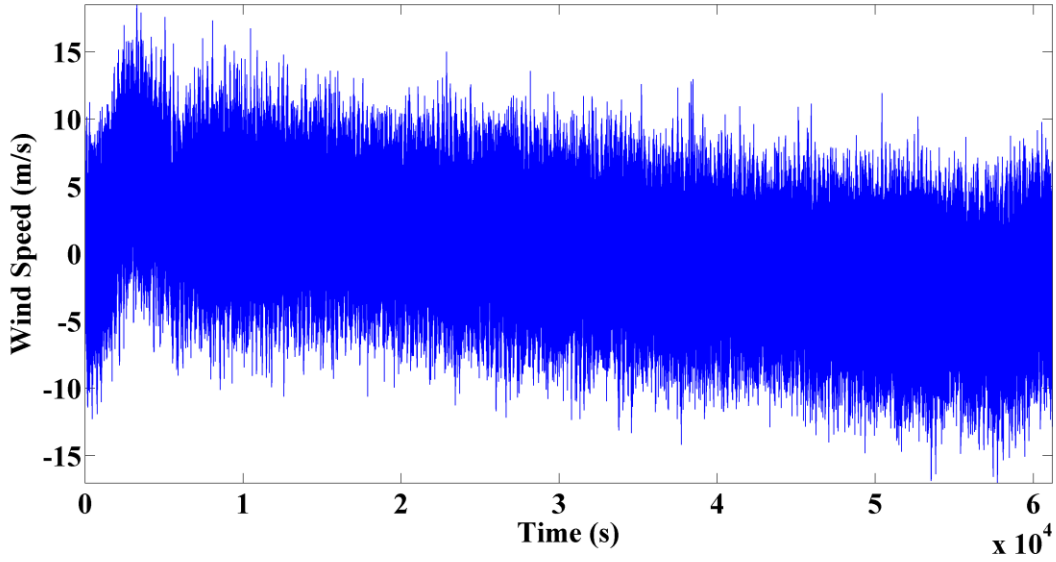

Figure 51: Simulated wind speed versus time.

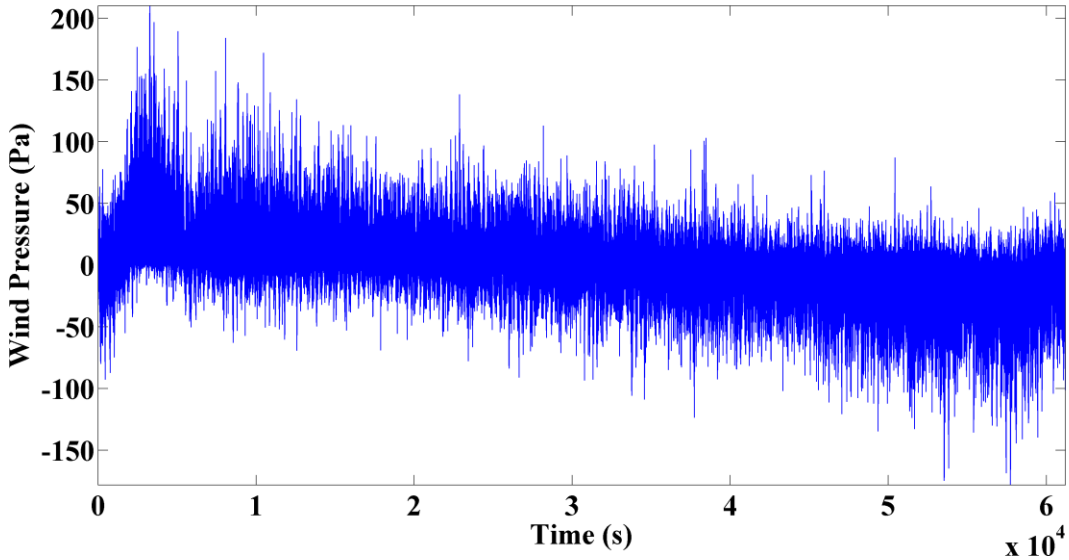

Figure 52: Simulated wind pressure versus time.

Figures 53 and 54 show two sets of wind pressures with 10-sec duration randomly extracted from the original data at 5Hz. In order to generate arbitrary wind load, the plate was divided into two regions such that two sets of wind pressure were applied perpendicularly to the plate (see Figure 55).

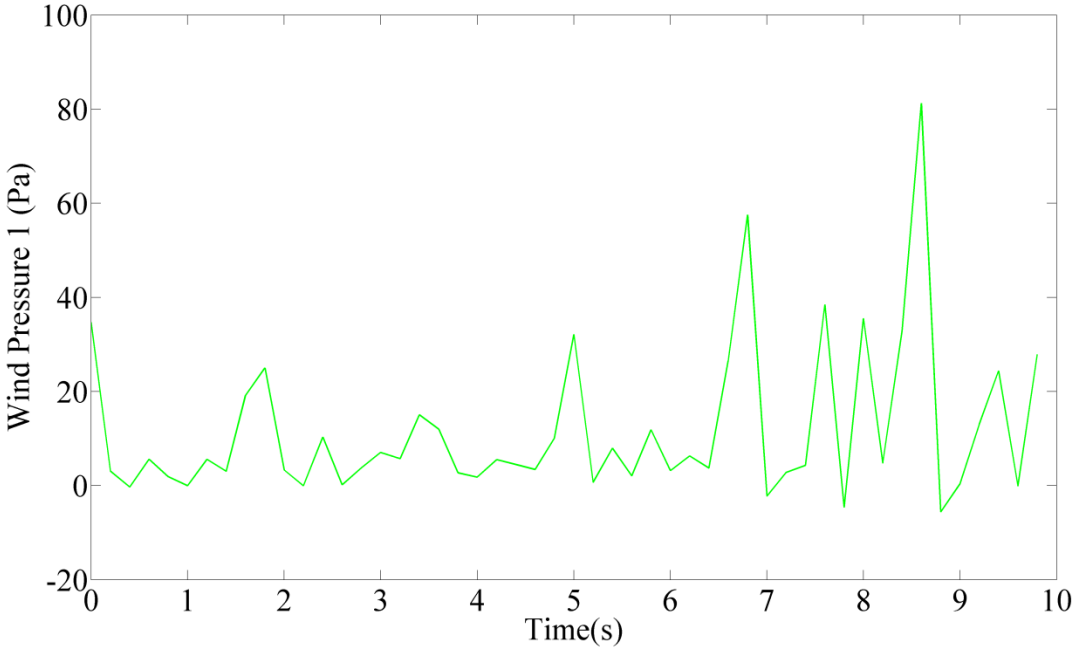

Figure 53: Random wind pressure #1, 10 sec @5Hz.

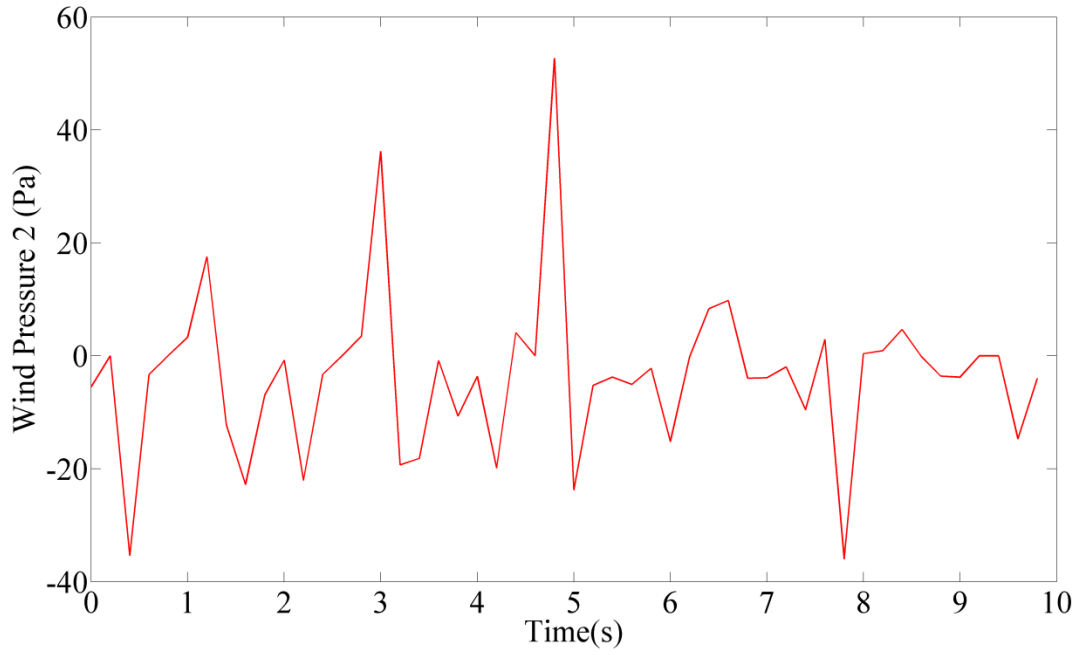

Figure 54: Random wind pressure #2, 10 sec @5Hz.

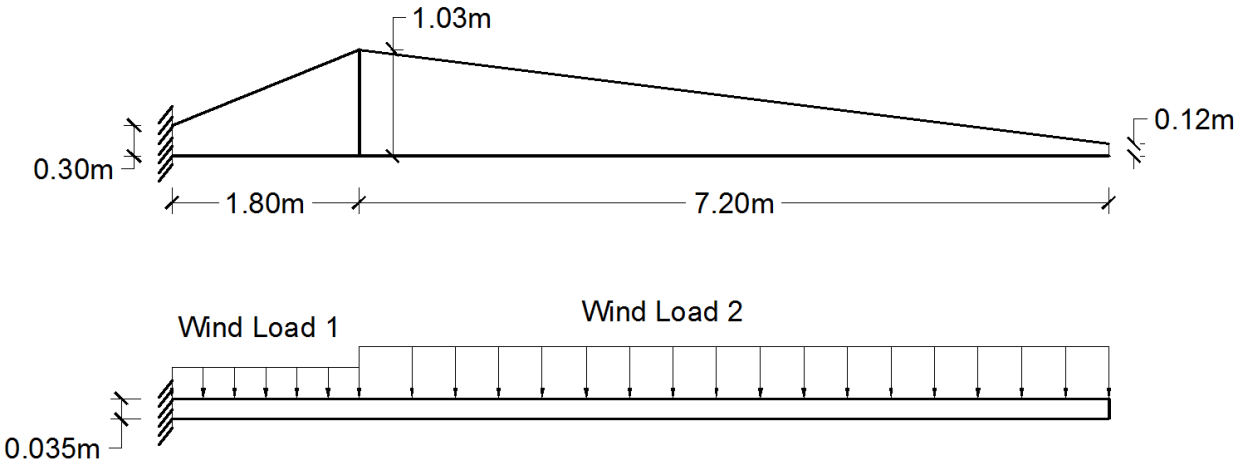

Figure 55: Loading condition of the plate.

5.3.2 Uniform and proposed sensor arrangements

As presented and discussed in CHAPTER 4, the strain decomposing results taken from uniform sensor placement were compared against the results from different sensor arrangements. The results show that the estimating accuracy has been improved by either staggering the inner sensors or diminishing the sensors on the plate boundaries. This conclusion was verified again in this chapter by rearranging the sensors in the same way that was used in CHAPTER 4 on the blade-shaped plate.

First, the uniform sensor arrangement will be illustrated. Due to the mapped mesh, the plate was equally divided into spaces with a distance of 0.1m longitudinally, and it was divided into 10 segments transversely. Considering the real size of an SEC, sensors were distributed every three nodes with a distance of 0.3m along the top and bottom edges. Then the inner sensor arrays were created based on the boundary sensor locations. The number of sensors along each cross section was customized in order to fit the corresponding width. The total number of sensors

were 142. The uniform arrangement is demonstrated in the first plot in Figure 56. For the second arrangement, the total number of sensors remained the same as in the uniform arrangement but with sensors staggered within the area of the plate. The last way is that the arrangement of all the inner sensors followed the same pattern as in uniform arrangement but with boundary sensors diminished from 62 to 43. As shown in Figure 56, the differences among three arrangements can be easily seen. In addition, only idealized boundary sensor arrangement has been used in order to perform a univariate test since: (1) the accuracy of the assumed boundary conditions will be affected if realistic boundary sensor placement is applied; (2) it is difficult to control the distance between the sensors and the boundaries to be consistent if applying realistic sensor arrangement due to the mapped mesh.

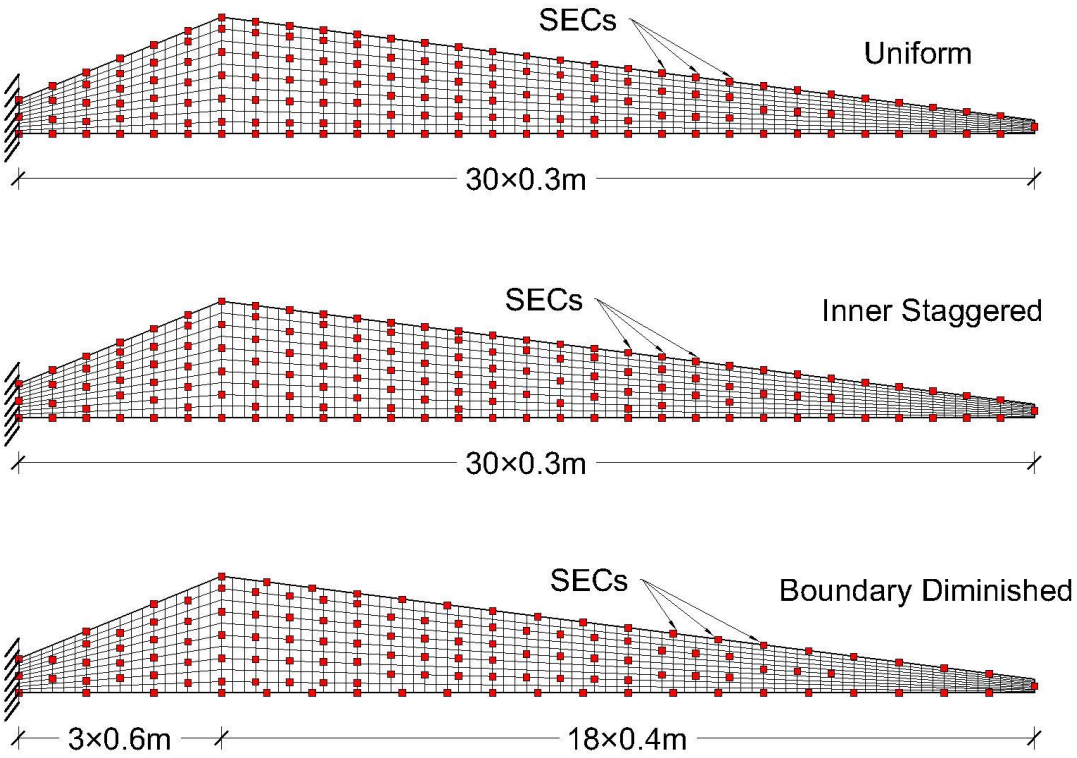

Figure 56: Sensor arrangements for blade-shaped plate.

5.3.3 Strain decomposing results comparison for different sensor arrangements

The dynamic analysis was performed using simulated wind turbulence in ANSYS, and bidirectional nodal elastic strain data were exported from the top layer of the plate. The proposed strain fitting algorithm was then applied to conduct the strain decomposition tasks. The procedures were repeated three times for all three different sensor arrangements. Multiple trials have been completed, and it is found that a polynomial function with 7^{th} order produces better results than a polynomial function with 6^{th} order. This finding might result because of the complexity of the skewed plate behavior. Therefore, the 7^{th} order polynomial function was used to assume displacement function. The results from the uniform sensor arrangement were compared against the two proposed arrangements. As the same in CHAPTER 3, the decomposing results were presented in the following forms: (1) 3D surface strain map; (2) MAPE contour plot; (3) MAPE versus load steps.

5.3.3.1 Strain Surface Fitting Results

The 3D surface strain map plots for three cases are shown below. One can see that the strains tend to decrease from the maximum value at the fixed end towards the tip of the plate, and a sudden change appears at the boundary of two loads due to the different wind load magnitudes. By looking at the two strain surfaces for both x and y directions in each plot, it is obvious that the estimating errors are fairly large near the fixed end. For strain x, the algorithm was underestimating the strain near the fixed end and was overestimating the strain near the free tip, see Figure 57. Also, strains on the inner areas close to the middle of the second part of the plate have shown to be underestimated, and the area appears to decrease if the sensor arrangements changed. The reason for this inner area shows the different trend than the

neighbors, and it is probably because strain y has been overfitted by using a 7^{th} order of polynomial displacement function, as could be seen in Figure 58.

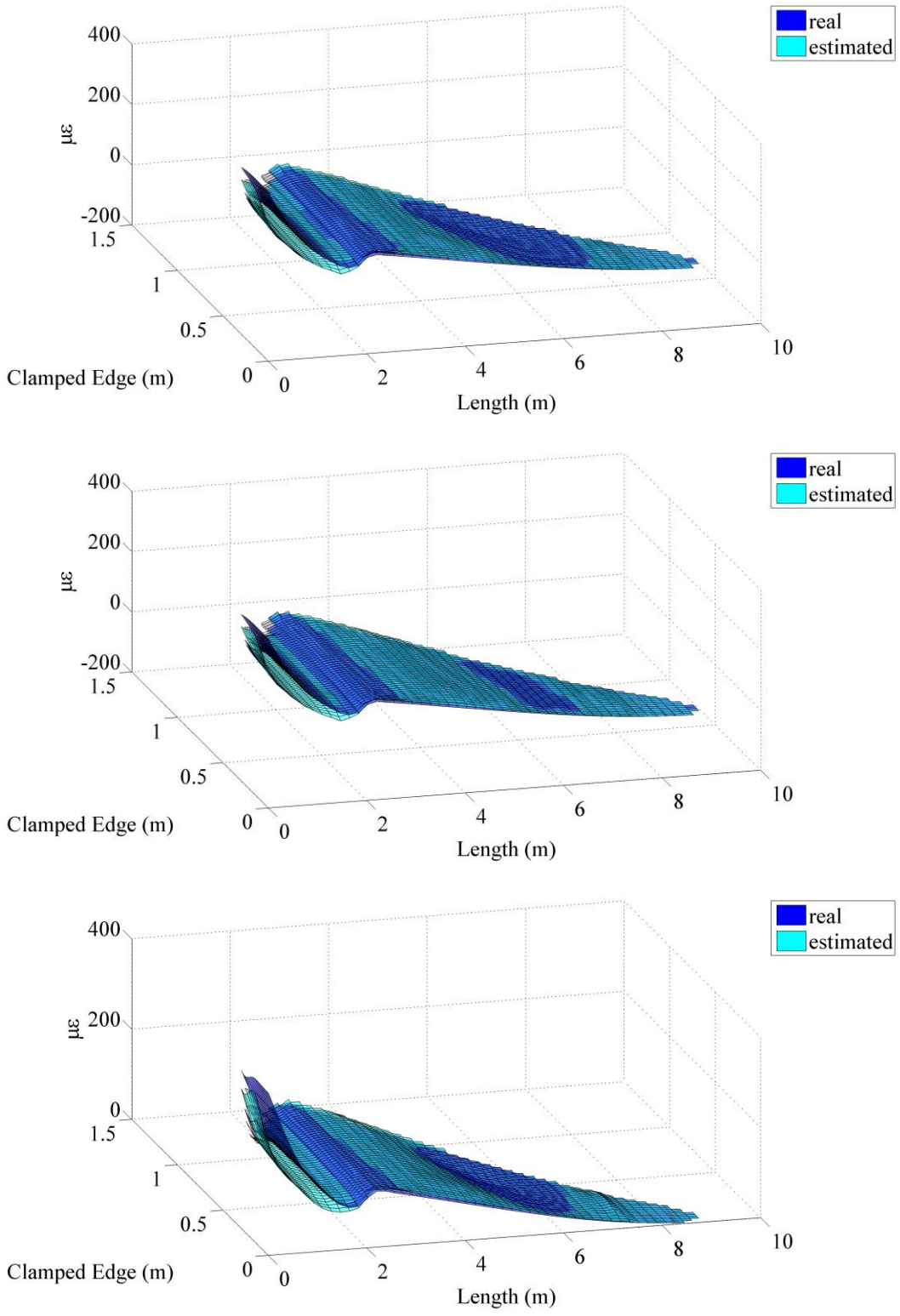

Figure 57: StrainX strain fitting for uniform pressure: uniform, arrangement #1, #2

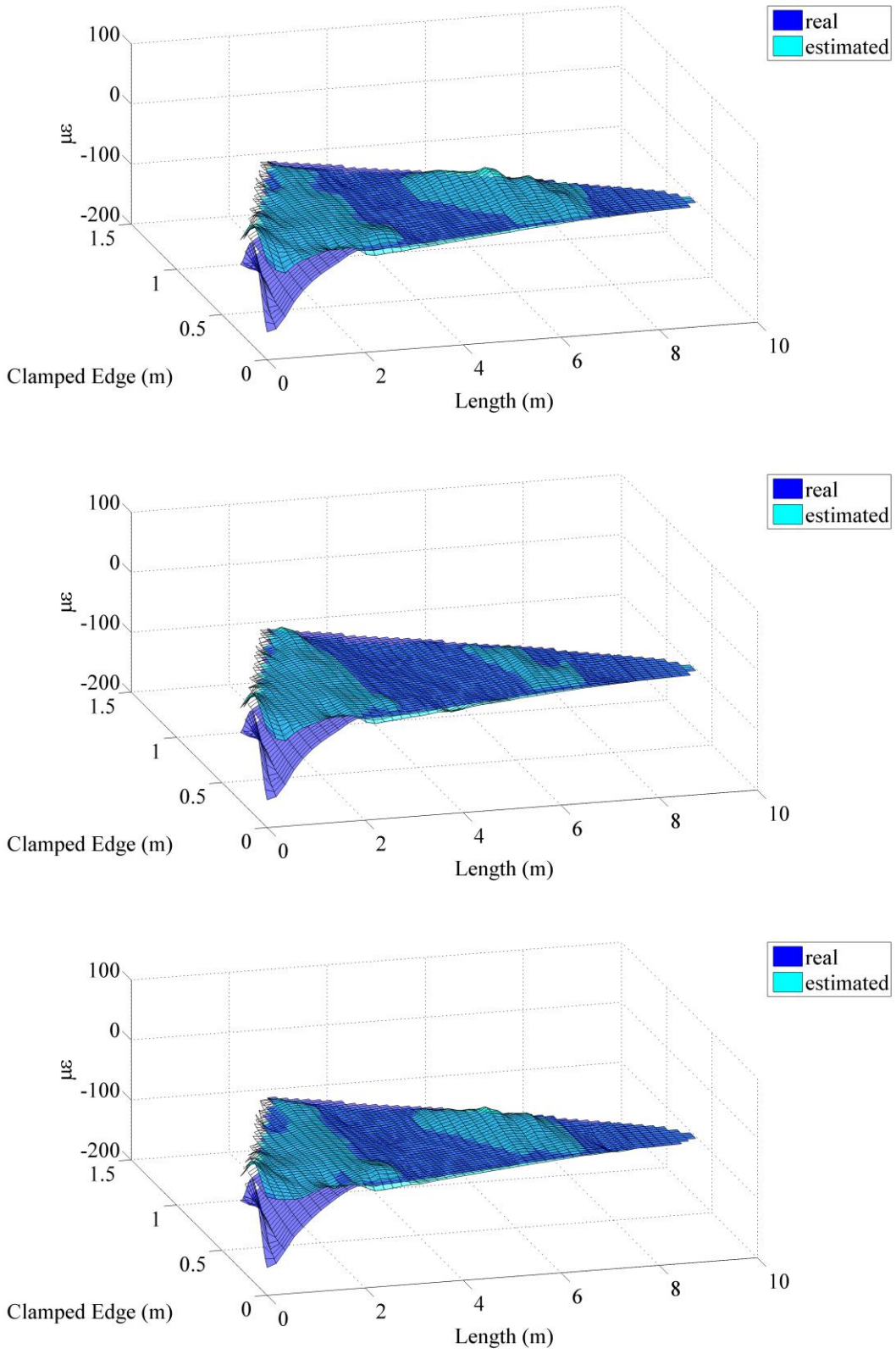

Figure 58: StrainY strain fitting for uniform pressure: uniform, arrangement #1, #2

5.3.3.2 Mean Absolute Percentage Error (MAPE) on Entire Plate

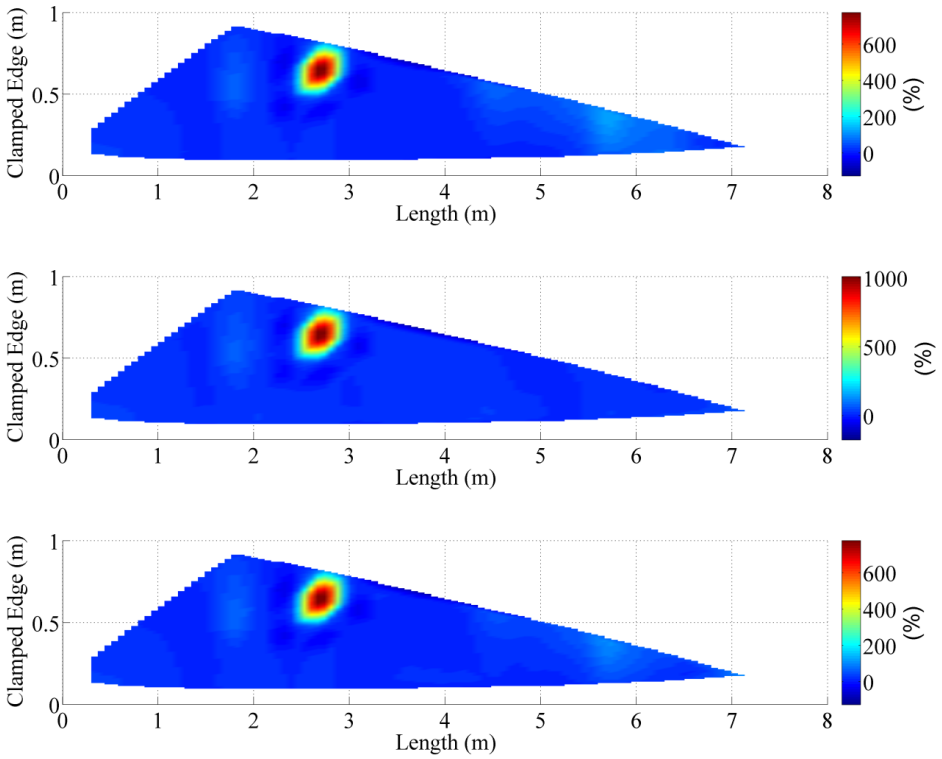

Figure 59: StrainX MAPE comparison for uniform pressure: uniform, arrangement #1, #2

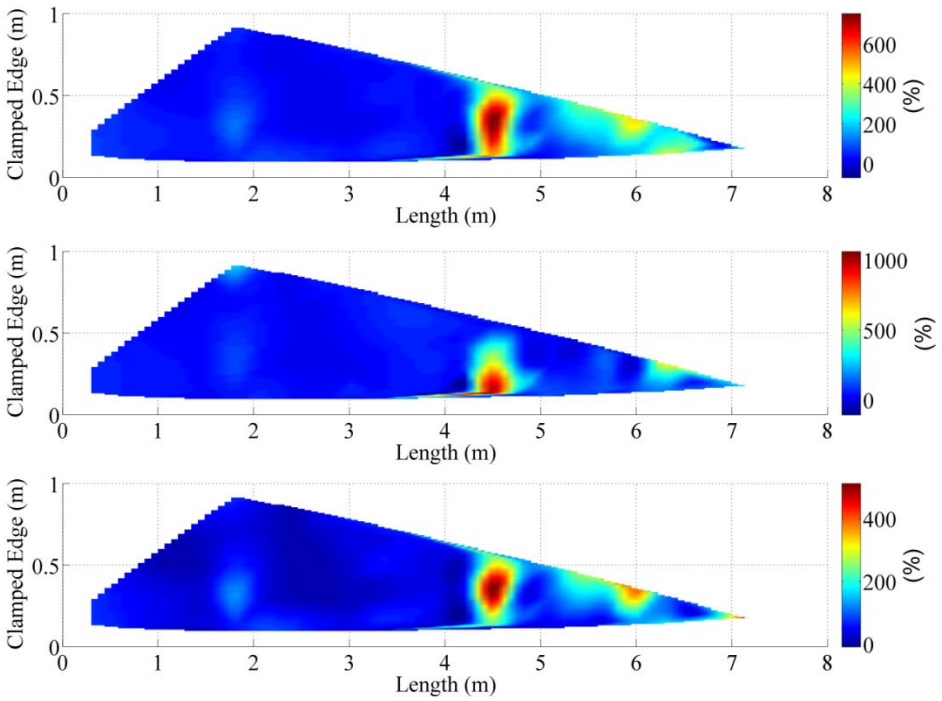

Figure 60: StrainY MAPE comparison for uniform pressure: uniform, arrangement #1, #2

Figures 59 and 60 show the contour plots of mean average percentage error for the inner plate area. For ε_x, the maximum error occurs close to the area, which has a sudden geometry change. The maximum error for ε_y, however, is located at x = 4.5m. Again, it could be explained that the strain y has been overfitted by using a higher degree polynomial function. Comparing the three sensor arrangements, the maximum errors for both ε_x and ε_y occurred to the staggered inner sensor arrangement with a value around 1000%. Boundary diminished arrangement seems to have the smallest errors. In addition, for ε_y, the errors near free tip are relatively large. Due to the low resolution for most of the plate area, it is not rational to conclude the performance of two proposed sensor arrangements only based upon the maximum errors. Thus, the same contour plots were presented in the next page using color bars with limited maximum value of 100%.

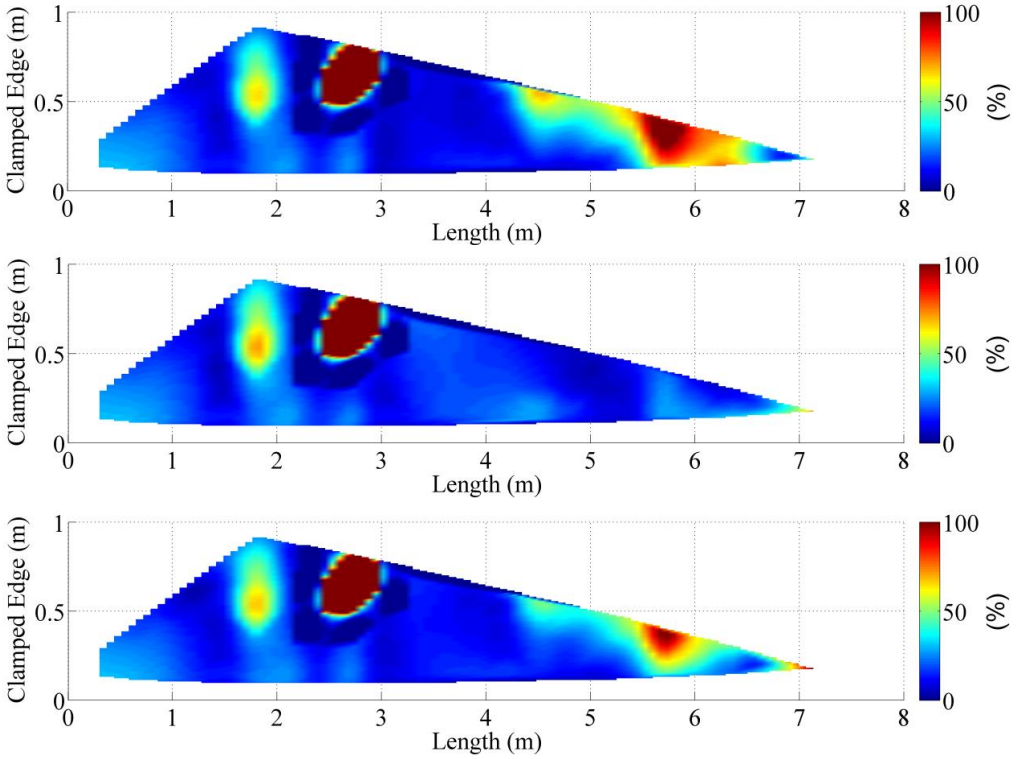

Figure 61: StrainX MAPE comparison for uniform pressure: uniform, arrangement #1, #2 (scaled)

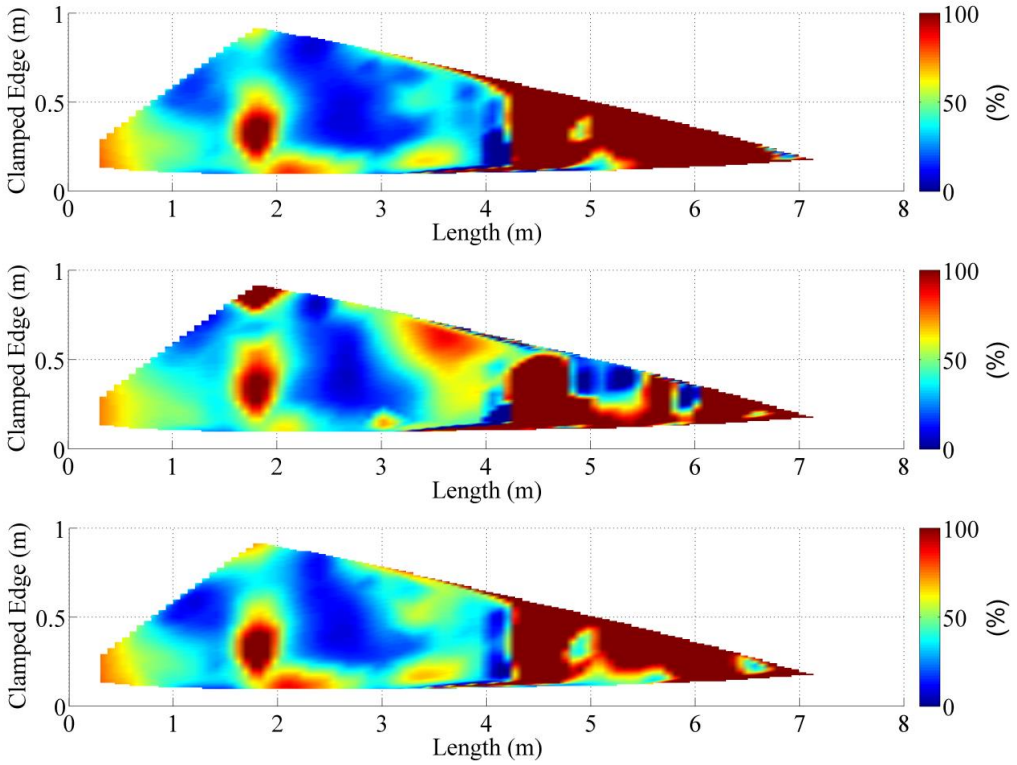

Figure 62: StrainY MAPE comparison for uniform pressure: uniform, arrangement #1, #2 (scaled)

As shown in Figures 61 and 62, the contour plots are more comparable among three arrangement cases. For ε_x, the errors are large at the free tip and the section with sudden geometry change. This feature coincides with the author's prediction because stress singularities always arise around the sharp corners for plates. The same tendency can be found in ε_y contour plots but with large errors (around 70%) near the fixed end as well. This tendency is probably because the estimating accuracy of the algorithm will be deficient when ε_y is very small at the fixed end. Furthermore, the dark red areas shown in the ε_y contour plot, which represent errors larger than 100%, concentrated on the free tip of the plate. It can be explained that the sensor quantities near the tip are very low due to limited space so that not enough information can be captured and used for estimation process. At last, it is obvious that the estimating accuracy has been improved using proposed sensor arrangements by looking at the error distributions shown in the contour plots, especially for inner staggered arrangement. The detailed comparison is provided in Table 9.

5.3.3.3 Mean Absolute Percentage Error (MAPE) on Entire Plate over Time Series

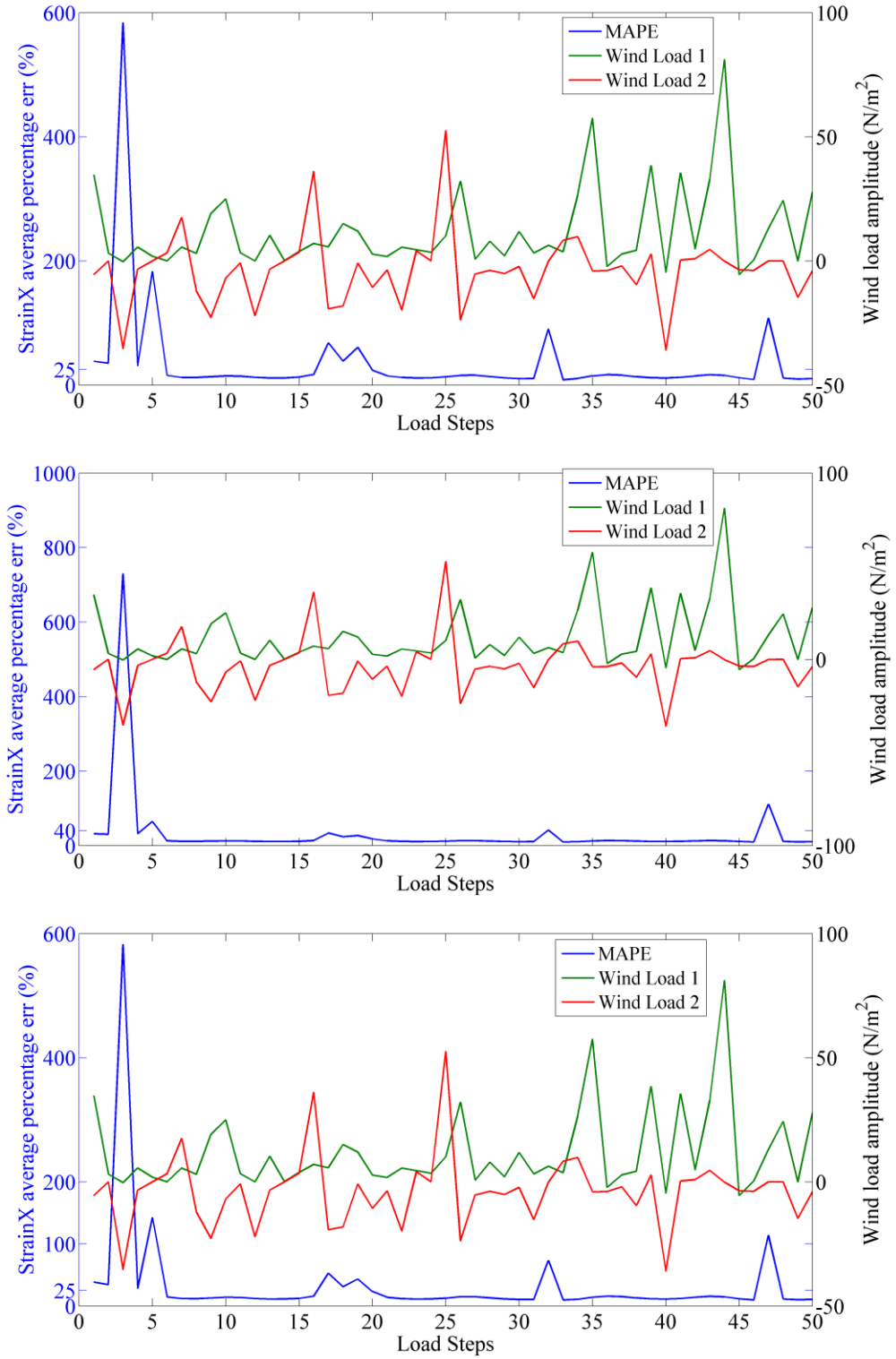

Figure 63: StrainX MAPE vs time comparison for uniform pressure: uniform, arrangement #1, #2

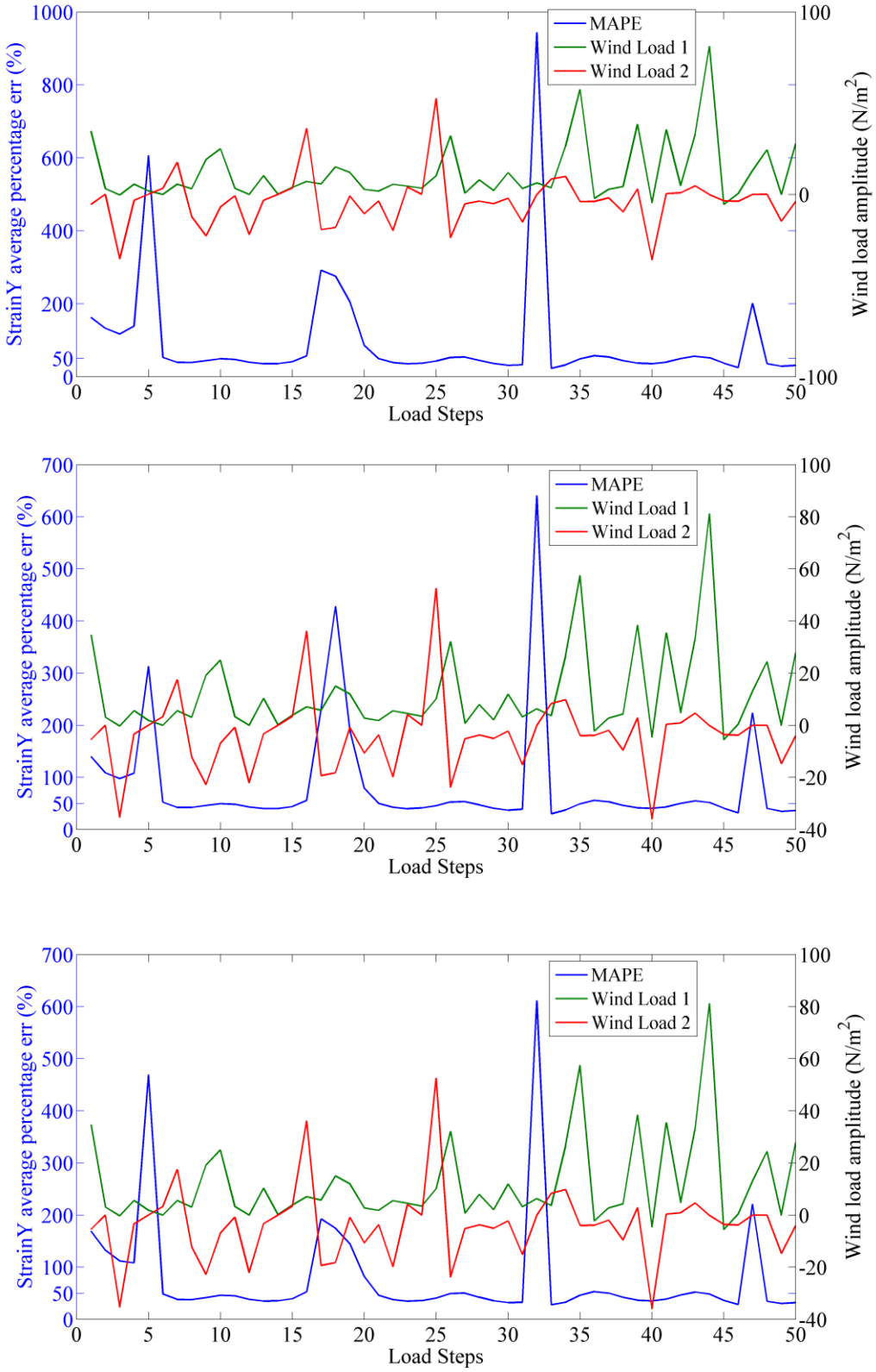

Figure 64: StrainY MAPE vs time comparison for uniform pressure: uniform, arrangement #1, #2

Two parts of wind load were applied on the two areas of the plate. The smaller wind load 1 was assigned to the area close to fixed, and the larger one (wind load 2) was distributed on the second part of the plate. In Figures 63 and 64, the MAPE of the entire plate over 50 load steps were plotted against the two wind load cases. It is clearly shown that the magnitudes of the wind loads were arbitrary so that it can simulate the realistic loading condition of the wind turbine blades. It is noticeable that a spike occurred at the third load step where wind load 1 almost equals zero while wind load 2 reaches the maximum negative value of 50Pa. The negative sign means the wind pressure is pulling the plate towards the positive z axis which resulted in compression on the top surface of the plate. For the other smaller spikes shown in the figures, one can find that these spikes usually occurred at the points where the summation of two wind loads are almost zero. The same situation has been encountered in CHAPTER 3 when applying the algorithm on the rectangular plate. In comparison of the MAPE for all three arrangement cases, the MAPE of ε_x from inner staggered arrangement seems to be the most stable one over the change in load magnitudes. In general, the overall performance of the algorithm for ε_x is more stable than ε_y when evaluating over load variance. Due to the difficulty of identifying the MAPE values in the plots for each case, the following table is provided in order to compare the estimating accuracy of each arrangement more efficiently.

Table 9: Results comparison for blade-shaped plate among three sensor arrangements.

Sensor Arrangement	Random Wind Pressure on Entire Plate				Determinant of $(\boldsymbol{C}'\boldsymbol{C})$
	Percentage error (%)				
	Mean*		Standard Deviation*		
	x	y	x	y	
Uniform_142nodes	35.39	95.87	625.78	637.88	1.3098E+17
Inner staggered	32.01	85.85	813.89	609.24	1.6698E+26
Boundary Diminished	33.17	79.73	625.30	420.80	3.8841E+20

** denotes that values are calculated from absolute percentage errors.*

Table 9 provides a detailed results comparison among three arrangements with mean errors by all load steps and the corresponding standard deviation. Apparently, the results from uniform sensor arrangement have the maximum percentage errors of 35.39% and 95.87% for ε_x and ε_y respectively. In the meantime, 32.01% is identified as the minimum error for ε_x and 79.73% for ε_y. It is shown that both proposed arrangements have improved the estimating accuracy of the algorithm. For inner staggered arrangement, error for ε_x has been reduced by 9.6% and error for ε_y has been reduced by 10.5%. Similarly, for boundary diminished arrangement, error for ε_x has been decreased by 6.3% and error for ε_y has been decreased by 16.8%. One can conclude that the estimating accuracy for ε_y is more sensitive than ε_x. Lastly, the determinant of $\boldsymbol{C}$ was calculated for each case, and it has shown the same results as those shown in Chapter 4: the inner staggered and boundary diminished sensor arrangements can increase the determinant of $\boldsymbol{C}$, which results in more accurate matrix inversion.

CHAPTER 6 CONCLUSIONS AND RECOMMENDATIONS

6.1 Conclusions

A sensing network consisting of a group of soft elastomeric capacitors (SECs) has been presented. This thesis introduces a study that has successfully utilized a proposed strain-fitting algorithm to decompose the unidirectional strains measured by SEC unit. The effect of different sensor placements has been investigated. Numerical simulations have been conducted on a rectangular plate with isotropic material properties and a blade-shaped plate with orthotropic laminated materials. The proposed strain-fitting algorithm then has been applied and validated to perform the strain decomposition tasks for both plates under various sensor arrangements. Several conclusions can be drawn as follows.

In general, for all load cases and sensor arrangements, the estimating accuracy of the proposed strain fitting algorithm is shown to be more accurate for ε_x than it is for ε_y. Meanwhile, the estimating accuracy can be improved by either staggering the inner sensors or diminishing boundary sensors on the plates. Furthermore, the algorithm performs better under pure bending loads (center tip point load, uniform pressure) than under torsional load (corner tip point load). Lastly, the estimating accuracy of the algorithm for ε_y is more sensitive to sensor arrangement than it is for ε_x.

6.1.1 Conclusions from validation on rectangular plate

The estimating accuracy of the algorithm varies with different loading cases. Based on the results from rectangular plate, it is found that the estimating errors become relative large at the regions where the concentrated loads are applied. Also, the maximum percentage error always occurs at the two corners along the free tip for both ε_x and ε_y. All of these findings are probably because the stress singularities always arise in two situations in structural analysis: (1) the concentrated load or moment acting upon plates and shells; (2) the sharp corners. For the maximum errors around free tip corners, it also can be explained that there are no applicable boundary conditions for these two nodes to be enforced. Therefore, the inversion results of matrices could be inaccurate due to a multicollinearity problem. Moreover, a spike has been found on the error contour plot for ε_y at the left bottom corner along the fixed end under the corner tip point load. This spike is probably because the BCs for two free end corners cannot hold anymore since the corner point load is inducing torsion effect while the applied BCs were derived from thin plate theory with bending behaviors. In addition, by comparing the MAPE contour plots for three load cases, the estimating accuracy for ε_y near the tip region of the plate is more sensitive than it is for ε_x.

If comparing the estimating mean absolute percentage error (MAPE) of the entire plate against a time series, several spikes can be easily observed at the time points where the load magnitude is zero. It is probably because no strain has been induced so that the program acquires useless data when applying the algorithm. Since no significant events will happen when applied loads are zero, however, these spikes are negligible. In contrast, the MAPEs at the other time

steps are fairly consistent; namely, the performance of the algorithm is stable over the change in load and is independent of load magnitudes.

According to the results obtained from the idealized and the realistic boundary sensor arrangements, it can be concluded that the estimating accuracy of the algorithm is higher in the idealized case than it is in the realistic case. Obviously, it is because the closer the sensors locate to the boundaries, the more accurate BCs they can obtain. Moreover, it shows that the algorithm is most likely to overestimate ε_x (underestimate ε_y) in the realistic boundary sensor arrangement, and to underestimate ε_x (overestimate ε_y) in the idealized boundary sensor arrangement.

Four ways of sensor placement have been performed and examined in terms of the number and locations of the sensors. It can be concluded that the inner staggered and boundary diminished sensor placements showed the positive effects on the estimating accuracy by increasing the determinant of sensor placement matrix. Moreover, some additional arrangement ways have been applied, and it is found that: (1) the proposed algorithm is not functioning properly if the total number of sensors on the boundaries is equal or greater than the amount of inner sensors; (2) under same arrangement of boundary sensors, the estimation is more precise if inner sensors are stagger-distributed and placed relatively close to fixed and free edges; (3) the error of estimation can be reduced if sensors on the boundaries are diminished possibly because of the imperfection of the plate's BCs obtained from the theory and consequently, it will lead to less accurate inversion results of coordinate matrices if more data on the boundaries are enforced; and (4) it is found that, a certain amount of sensors is required to be placed on the boundaries in order to ensure the full rank of the coordinate matrices. Otherwise the inversion results will be incorrect. Taking the rectangular plate as an example, besides four SECs located on the corners,

at least two more SECs for fixed and free edges, and three more SECs for top and bottom edges are required to perform accurate strain decomposition task.

6.1.2 Conclusions from verification on blade-shaped plate

Once the algorithm was validated on a rectangular plate, it has been applied to a blade-shaped plate with random wind pressure. Two positive sensor arrangements were verified as well. The results show that the algorithm has successfully decomposed the unidirectional strains with acceptable accuracy. This result means that the proposed algorithm is capable of performing the strain decomposition tasks for SEC networks regardless of material properties, loading circumstances, and geometry variations. The decomposing accuracy of the algorithm, however, will be highly affected by the aforementioned three factors. More importantly, the results verified that the two positive sensor arrangements successfully improved the estimating accuracy by increasing the determinant of the sensor placement matrix, which leads to more accurate matrix inversion. Additionally, compared with results obtained from the rectangular plate, the estimating accuracy of the blade-shaped plate is relatively low. This low estimating accuracy can be explained in that the shear deformation has been ignored when performing the numerical simulation as well as when assuming the displacement function. It might have accountable influence on the results, however, due to the thickness of the plate. Moreover, it is found that the estimating errors are relative large near the free tip of the plate. On one hand, this large estimating error is because of the effects of stress singularities near the tip corners; on the other hand, the amount of sensors located near the tip has been reduced a lot so that the information collected is not sufficient to conduct a good estimation.

6.2 Recommendations

According to the conclusions drawn in the previous section, several recommendations can be suggested to enhance the performance of the proposed algorithm as well as to improve the estimating accuracy. First of all, sensors should be placed as close as possible to the structure's boundaries so that accurate boundary conditions can be acquired in order to perform inversion of coordinate matrices precisely. In the case of limited spaces for SECs, one can be considered to employ traditional resistive strain gauges (RSGs) on the boundaries. Furthermore, due to the small size of the RSGs, they can be placed close enough to the boundaries. Therefore, the quality of boundary conditions can be ensured. Secondly, when applying sensors on the boundaries, it is not suggested to attach them around sharp corners or near regions that have sudden geometry change. This suggestion is because stress singularities always occur at these locations, and it will result in providing inaccurate boundary conditions to the system. Additionally, either using staggered inner sensor arrangement or diminishing the amount of sensors on the boundaries is most likely to improve the performance of the algorithm. Lastly, it has been observed that unusual estimating errors will occur when the applied load is zero. Therefore, the external loads should be monitored at all time so that the points that have zero load magnitude can be identified and corresponding estimating error spikes can be diminished when evaluating the performance of the algorithm.

6.3 Future Work

In order to obtain good decomposing results, a better understanding of the behaviors of the plates with different material properties and arbitrary geometries is necessary. The algorithm should be tested using a numerical simulation that accounts for shear deformation of plates. In addition, the application of the proposed algorithm using experimental strain data obtained from thin plates under various configurations (ex, load conditions, material properties, and arbitrary geometries) could provide practical first-hand experience. Furthermore, validation of the algorithm on a real wind turbine blade model will be necessary in order to eventually accomplish the strain decomposition task in the realistic circumstances.

REFERENCE

1. *2012 Half Year Report*, in *World Wind Energy Association*. 2012.

2. Ciang, C.C., J.-R. Lee, and H.-J. Bang, *Structural health monitoring for a wind turbine system: a review of damage detection methods.* Measurement Science and Technology, 2008. **19**(12): p. 122001.

3. Farrar, C.R. and K. Worden, *An introduction to structural health monitoring.* Philosophical Transactions of the Royal Society A: Mathematical, Physical and Engineering Sciences, 2007. **365**(1851): p. 303-315.

4. Laflamme, S., et al., *Soft Elastomeric Capacitor Network for Strain Sensing Over Large Surfaces.* Mechatronics, IEEE/ASME Transactions on, 2013. **18**(6): p. 1647-1654.

5. Turner, A. and T.W. Graver, *Structural monitoring of wind turbine blades using fiber optic Bragg grating strain sensors*, in *Experimental Mechanics on Emerging Energy Systems and Materials, Volume 5*. 2011, Springer. p. 149-154.

6. Takeda, N., *Characterization of microscopic damage in composite laminates and real-time monitoring by embedded optical fiber sensors.* International Journal of Fatigue, 2002. **24**(2): p. 281-289.

7. Doyle, C., *Fibre Bragg Grating Sensors-An Introduction to Bragg gratings and interrogation techniques.* Smart Fibres Ltd, 2003: p. 1-5.

8. Rademakers, L., et al. *Fiber optic blade monitoring*. in *European Wind Energy Conference, London*. 2004.

9. Wikipedia. *Acoustic Emission*. The Free Encyclopedia 2014 [cited 2014; Available from: http://en.wikipedia.org/wiki/Acoustic_emission.

10. Joosse, P., et al., *Acoustic emission monitoring of small wind turbine blades.* Journal of solar energy engineering, 2002. **124**(4): p. 446-454.

11. Erik R. Jørgensen, K.K.B., Malcolm McGugan, Christian L. Thomsen, Find M. Jensen, Christian P. Debelog Bent F. Sørensen, *Full Scale Testing of wind Turbine Blade to Failure.* Riso-R-1392(EN) National Laboratory, Denmark, 2004.

12. Ghoshal, A., et al., *Health monitoring of composite plates using acoustic wave propagation, continuous sensors and wavelet analysis.* Journal of reinforced plastics and composites, 2007. **26**(1): p. 95-112.

13. Blanch, M. and A. Dutton, *Acoustic emission monitoring of field tests of an operating wind turbine.* Key Engineering Materials, 2003. **245**: p. 475-482.

14. Todoroki, A. and Y. Tanaka, *Delamination identification of cross-ply graphite/epoxy composite beams using electric resistance change method.* Composites Science and Technology, 2002. **62**(5): p. 629-639.

15. Matsuzaki, R. and A. Todoroki, *Wireless detection of internal delamination cracks in CFRP laminates using oscillating frequency changes.* Composites science and technology, 2006. **66**(3): p. 407-416.

16. Tata, U., et al., *Bio-inspired sensor skins for structural health monitoring.* Smart Materials and Structures, 2009. **18**(10): p. 104026.

17. Carlson, J., J. English, and D. Coe, *A flexible, self-healing sensor skin.* Smart materials and structures, 2006. **15**(5): p. N129.

18. Kang, I., et al., *A carbon nanotube strain sensor for structural health monitoring.* Smart materials and structures, 2006. **15**(3): p. 737.

19. Laflamme, S., et al. *Thin film sensor network for condition assessment of wind turbine blades*. in *SPIE Smart Structures and Materials+ Nondestructive Evaluation and Health Monitoring*. 2014. International Society for Optics and Photonics.

20. Wilkinson, A., M. Clemens, and V. Harding, *The effects of SEBS-< i> g</i>-maleic anhydride reaction on the morphology and properties of polypropylene/PA6/SEBS ternary blends.* Polymer, 2004. **45**(15): p. 5239-5249.

21. Acam-messelectronic, *DAQ Acam PCap01-EVA-KIT*, in *http://www.acam.de/typo3temp/pics/4027ce32bb.jpg*, Acam-messelectronic.

22. Wu, J., *Development of an algorithm for strain signal decomposition of Soft Elastomeric Capacitors on structural surface*, in *Civil Engineering*. 2014, Iowa State university.

23. Tessler, A. and J.L. Spangler, *A least-squares variational method for full-field reconstruction of elastic deformations in shear-deformable plates and shells.* Computer methods in applied mechanics and engineering, 2005. **194**(2): p. 327-339.

24. Glaser, R., V. Caccese, and M. Shahinpoor, *Shape monitoring of a beam structure from measured strain or curvature.* Experimental mechanics, 2012. **52**(6): p. 591-606.

25. Nishio, M., T. Mizutani, and N. Takeda, *Structural shape reconstruction with consideration of the reliability of distributed strain data from a Brillouin-scattering-based optical fiber sensor.* Smart Materials and Structures, 2010. **19**(3): p. 035011.

26. Jones, R., et al., *Determination of cantilever plate shapes using wavelength division multiplexed fiber Bragg grating sensors and a least-squares strain-fitting algorithm.* Smart materials and structures, 1998. **7**(2): p. 178.

27. Heins, C.P., *Applied plate theory for the engineer*. 1976: Lexington Books.

28. Ventsel, E. and T. Krauthammer, *Thin plates and shells: theory: analysis, and applications*. 2001: CRC press.

29. Huang, C., *Stress singularities at angular corners in first-order shear deformation plate theory.* International journal of mechanical sciences, 2003. **45**(1): p. 1-20.

30. Parker, D.L., et al. *Experimental validation of optimal sensor placement algorithms for structural health monitoring*. in *Proceedings of the Third European Workshop on Structural Health Monitoring*. 2006.

31. Kubrusly, C. and H. Malebranche, *Sensors and controllers location in distributed systems—A survey.* Automatica, 1985. **21**(2): p. 117-128.

32. Heo, G., M.L. Wang, and D. Satpathi, *Optimal transducer placement for health monitoring of long span bridge.* Soil Dynamics and Earthquake Engineering, 1997. **16**(7–8): p. 495-502.

33. T.G. Carne, C.R.D., *A modal test design strategy for model correlation.* Proceedings of the 13th International Modal Analysis Conference, Nashville, TN, 1995.

34. Kammer, D.C., *Sensor placement for on-orbit modal identification and correlation of large space structures.* Journal of Guidance, Control, and Dynamics, 1991. **14**(2): p. 251-259.

35. Yao, L., W.A. Sethares, and D.C. Kammer, *Sensor placement for on-orbit modal identification via a genetic algorithm.* AIAA Journal, 1993. **31**(10): p. 1922-1928.

36. Guo, H.Y., et al., *Optimal placement of sensors for structural health monitoring using improved genetic algorithms.* Smart Materials and Structures, 2004. **13**(3): p. 528.

37. Cobb, R.G. and B.S. Liebst, *Sensor Placement and Structural Damage Identification from Minimal Sensor Information.* AIAA Journal, 1997. **35**(2): p. 369-374.

38. C.C. Flanigan, C.D.B., *Automated selection of accelerometer locations for modal survey tests.* Proceedings of the 20th International Modal Analysis Conference (IMAC-X), San Diego, CA, 1992.

39. Balageas, D., C.-P. Fritzen, and A. Güemes, *Structural health monitoring*. Vol. 493. 2006: Wiley Online Library.

40. Li, H.-N., D.-S. Li, and G.-B. Song, *Recent applications of fiber optic sensors to health monitoring in civil engineering.* Engineering structures, 2004. **26**(11): p. 1647-1657.

41. Ashwill, T., *Blade Manufacturing Improvements Development of the ERS-100 Blade.* 2001., 2001.

42. Berry, D. and T. Ashwill, *Design of 9-meter carbon-fiberglass prototype blades: CX-100 and TX-100.* SAND2007-0201, Sandia National Laboratories, Albuquerque, NM, 2007.